

Structural Characterization of Proteasome Inhibition

Dissertation
for the award of the degree
"Doctor rerum naturalium" (Dr. rer. nat.)
of the Georg-August-Universität Göttingen

within the doctoral program
Biomolecules: Structure - Function - Dynamics
of the Göttingen Graduate School for Neuroscience, Biophysics and
Molecular Biosciences (GGNB)

submitted by

Jil Schrader

from Geseke, Germany

Göttingen, 2017



Thesis Committee

Prof. Dr. Holger Stark (Reviewer)

Structural Dynamics, Max Planck Institute for Biophysical Chemistry

Prof. Dr. Ralf Ficner (Reviewer)

Molecular Structural Biology, Göttingen Center for Molecular Biosciences

Dr. Karin Kühnel

until 2016: Neurobiology, Max Planck Institute for Biophysical Chemistry

Members of the Examination Board

Prof. Dr. Holger Stark

Structural Dynamics, Max Planck Institute for Biophysical Chemistry

Prof. Dr. Ralf Ficner

Molecular Structural Biology, Göttingen Center for Molecular Biosciences

Prof. Dr. Blanche Schwappach

Molecular Biology, University Medical Center Göttingen

Dr. Alexander Stein

Membrane Protein Biochemistry, Max Planck Institute for Biophysical Chemistry

Prof. Dr. Henning Urlaub

Bioanalytical Mass Spectrometry, Max Planck Institute for Biophysical Chemistry

Prof. Dr. Detlef Doenecke

Molecular Biology, University Medical Center Göttingen

Date of the oral examination: 22.05.2017

I hereby declare that the PhD thesis 'Structural Characterization of Proteasome Inhibition' has been written independently with no other aids or sources than quoted. This thesis (wholly or in part) has not been submitted elsewhere for any academic award or qualification.

A handwritten signature in black ink, appearing to read 'J. Schrader'. The signature is written in a cursive, flowing style with a large initial 'J'.

Jil Schrader

Contents

List of Publications	v
Abstract	vi
1 Introduction	1
1.1 Ubiquitin-Mediated Proteolysis	1
1.1.1 The Ubiquitin-Proteasome Pathway Mechanism	1
1.2 The 20S and 26S Proteasome	4
1.2.1 The 20S Proteasome - Structure and Function	4
1.2.2 The 20S Catalytic Mechanism - Proteolysis	7
1.2.3 The 26S Proteasome - Structure and Function	8
1.3 Proteasome Inhibition	13
1.3.1 Boronic Acid Inhibitors	15
1.3.2 Epoxyketone Inhibitors	16
1.3.3 Ketoaldehyde Inhibitors	16
1.3.4 Recent Advances in Proteasome Inhibitor Development	17
1.3.5 Biological Implication of Proteasome Inhibition	18
1.4 An Introduction to X-ray Crystallography and Single Particle Electron Cryomicroscopy	20
1.4.1 X-ray Crystallography	20
1.4.2 Single Particle Electron Cryomicroscopy	23
1.4.3 Advantages and Disadvantages	24
1.5 Objectives	27
2 Materials and Methods	29
2.1 Materials	29
2.1.1 Software	29
2.1.2 Special Equipment	30
2.1.3 Chemicals	31
2.1.4 Buffers	33
2.2 Methods	34
2.2.1 Protein Purification	34
2.2.1.1 Purification of 20S Proteasomes from HeLa cells	34
2.2.1.2 Purification of 26/30S Proteasomes from HeLa Cells	35

2.2.2	Enzyme Kinetics	36
2.2.3	Electronic Structure Calculations	37
2.2.4	Crystallization Methods	38
2.2.4.1	Preparation of Protein Crystals	38
2.2.4.2	Postcrystallization Treatment	39
2.2.5	X-ray Analysis Methods	40
2.2.5.1	Crystal Mounting and Diffraction Data Collection	40
2.2.5.2	Structure Determination	40
2.2.5.3	Identification of Ions	40
2.2.6	Sample Preparation for Electron Microscopy	41
2.2.6.1	GraFix	41
2.2.6.2	Negative Staining	41
2.2.6.3	Vitrification	42
2.2.7	Imaging of Electron Microscopic Data	42
2.2.8	Image Processing	42
2.2.8.1	Micrograph Analysis and Particle Picking	42
2.2.8.2	2D Processing	43
2.2.8.3	Initial Model Building	43
2.2.8.4	Conformational Sorting	43
2.2.8.5	Refinement and Resolution Determination	43
2.2.8.6	Model Building	44
2.2.8.7	Validation	44
2.2.9	Visualization of the Conformational Space of the Human 26S Proteasome	44
3	Results	47
3.1	Native Human 20S Proteasomes and in Complex with Inhibitors	47
3.1.1	Purification and Crystallization of the Human 20S Proteasome	47
3.1.1.1	Preparation of Human 20S Proteasome Crystals	49
3.1.1.2	Postcrystallization Treatments	49
3.1.2	Native Crystal Structure of the Human 20S Proteasome	51
3.1.3	Crystal Structures of Seven Inhibitor Complexes of the Human 20S Proteasome	53
3.1.4	Structural Implications of the Six-ring Linkage	58
3.1.5	Elucidation of the Inhibition Mechanism of Epoxyketone Inhibitors	60
3.2	Structural Impact of 20S Inhibitors on the Human Proteasome Holoenzyme	65
3.2.1	Purification and Analysis of the Human 26S Proteasome in Complex with Oprozomib	65

3.2.2	EM Structure of the Human 26S Proteasome in Complex with Oprozomib	68
3.2.3	Restricted Dynamics in the Inhibited 26S Proteasome	72
3.2.4	The Energy Landscape of the Lid Movements	74
4	Discussion	77
4.1	Pipeline for Structure-based Analysis of Human Proteasome Inhibition	78
4.2	Native Human 20S Proteasomes Structure at 1.8 Å Resolution	80
4.3	Human 20S Proteasome Inhibition	82
4.4	Structural Impact of 20S Inhibitors on the 26S Holoenzyme	88
4.5	A Potential bi-directional Signaling Pathway	91
5	Conclusion and Outlook	97
Appendices		
A	Declaration of contribution as co-author	I
B	Abbreviations	III
Bibliography		
		VII
Acknowledgements		
		XXIII
Curriculum Vitae		
		XXV

List of Publications

This thesis is based on the following publication and manuscript:

1. **J. Schrader***, F. Henneberg*, R. A. Mata, K. Tittmann, T. R. Schneider, H. Stark, G. Bourenkov, A. Chari. (2016). The inhibition mechanism of human 20S proteasomes enables next-generation inhibitor design. *Science*. 353(6299), 594-598.
2. D. Haselbach*, **J. Schrader***, F. Lambrecht, F. Henneberg, A. Chari, H. Stark. Long range allosteric regulation of the human 26S proteasome by 20S proteasome-targeting cancer drugs. Manuscript in preparation.

* authors contribute equally to this work.

In addition, parts of this work are registered for patent:

1. H. Stark, A. Chari, **J. Schrader**, F. Henneberg. (2016). Method for the purification of biological macromolecular complexes. EP 16173037.9 and USSN 62/345,913. Filed January 2016. Patent Pending.
2. H. Stark, A. Chari, **J. Schrader**, F. Henneberg. (2016). Next-generation proteasome inhibitor design. EP 16173057.7 and USSN 62/346,203. Filed January 2016. Patent Pending.

Abstract

The proteasome plays a major role in non-lysosomal protein degradation pathways and inhibition of proteasomes became a valid therapeutic strategy for anti-cancer therapy in the recent years. Current efforts focus on the identification and development of second generation inhibitors with enhanced pharmacological properties. For this, improved structural knowledge and an advanced biochemical characterization of proteasome inhibition is necessary.

In this work, I present a reproducible and robust pipeline that enables the purification, crystallization, crystal handling and structure determination of the native 20S proteasome and 20S-inhibitor complexes. Crystal structures including four previously uncharacterized inhibitor complexes with clinically relevant inhibitors were elucidated at resolutions between 1.8 and 2.1 Å. The improved resolutions allow to define the inhibition chemistry at atomic resolution. This led to revised descriptions of binding modes for epoxyketone and ketoaldehyde inhibitors, a redefinition of the proteasome active site, and a concept for future drug design.

Single particle electron cryomicroscopy (cryo-EM) was the method of choice when studying the influence of 20S core particle inhibition on the dynamic 26S holoenzyme. We determined structures of the 26S proteasome with and without inhibitor and report for the first time structural changes of 26S proteasomes upon inhibition. Drug binding limits the conformational space of the 19S regulatory particle and we identified an energy barrier that stabilizes the proteasome in a non-productive state. Here, we describe that core particle inhibition triggers a structural long-range allosteric regulation of the human 26S proteasome.

This thesis offers insights into the exact catalytic mechanism of peptide cleavage and proteasome inhibition in the human 20S proteasome and a detailed description of the proteolytic site. In addition, the structural impact of 20S inhibition on the human 26S proteasome was studied for the first time and the findings allow for a new way to screen and develop future allosteric proteasome inhibitors. A reproducible workflow to structurally study inhibitor-proteasome complexes by advanced protein complex purification combined with X-ray crystallography or single particle cryo-EM is presented.

Keywords: protein complex purification, X-ray crystallography, electron cryomicroscopy, single particle image processing, structural dynamics, cancer therapeutics, drug design

Chapter 1

Introduction

1.1 Ubiquitin-Mediated Proteolysis

Protein degradation is a major part of protein homeostasis in the cell. The concept of protein degradation is at the center of understanding the underlying causes of the ever-growing list of diseases associated with protein misfolding¹ as well as aggregation-related degenerative disorders². Proteins in the cell have half-lives that range from a few minutes to several days and the level of all proteins must be evaluated continuously to uphold the required balance. The cell's ability to adapt to changing conditions or to progress through its general life cycle, ultimately requires a dynamic composition of its proteome. To maintain normal cell function new proteins are synthesized and old or unused proteins are degraded³.

In the 1970s, an intracellular, non-lysosomal protein degradation pathway was discovered and today it is known that protein degradation in eukaryotes is almost entirely undertaken by a complex molecular machine, the proteasome⁴. The proteasome forms the center of the ubiquitin-proteasome system (UPS), with critical functions in cell cycle control, protein quality control, programmed cell death by apoptosis, inflammation, transcription and many more biological processes³. The extent of the UPS is facilitated by a broad range of ubiquitin ligase enzymes and specific factors. The proteasome is the only ATP-dependent protease found in eukaryotes and the only one that is ubiquitin dependent⁵. Structurally, the proteasome is a hybrid of a proteolytic and ATP-dependent regulatory machinery composed of a 20S core particle and 19S regulatory particle, respectively⁶.

1.1.1 The Ubiquitin-Proteasome Pathway Mechanism

Degradation of proteins by the UPS is energy dependent and includes two discrete and successive parts: (1) substrate recognition, whereby the substrate specificity is ensured by polyubiquitination of substrates by specific enzymes and (2) substrate unfolding to

make the polypeptide backbone fully accessible for proteolytic cleavage⁷.

Proteins destined for degradation are modified with polymers of the highly conserved protein, ubiquitin. The covalent attachment of ubiquitin to the substrate is carried out by a series of enzymes (Figure 1.1):

Ubiquitin is first activated upon ATP turnover by an E1 ubiquitin activating enzyme, forming a high energy thiol ester with the carboxyl group at the C-terminus, thereby activating the C-terminus of ubiquitin for nucleophilic attack. Subsequently, the activated ubiquitin molecule is transferred to the active site cysteine of a second enzyme, the E2 ubiquitin conjugating enzyme. The ubiquitin ligase E3 recognizes its substrate, transfers the activated ubiquitin from the E2 enzyme to the substrate and catalyzes the formation of an isopeptide bond between a lysine residue of the substrate and the C-terminus of the ubiquitin. To form polyubiquitin chains, additional ubiquitin molecules are ligated to Lys48 of the ubiquitin that is already conjugated to the protein substrate⁸. Generally, a chain of four or more ubiquitin molecules is necessary to create a targeting signal for degradation by the proteasome and this three-step mechanism initiates all known ubiquitination reactions, independent of the biological fate⁹.

In human, numerous enzymes are involved in the UPS: two E1 enzymes, approximately 30 E2 conjugating enzymes and more than 500 E3 ubiquitin ligases, whereby the substrate selection is carried out by the different types of E3 ubiquitin ligases¹⁰.

Furthermore, deubiquitinating enzymes (DUBs) are part of the ubiquitin-proteasome pathway mechanism. These enzymes are responsible for removing ubiquitin from targeted proteins and disassemble polyubiquitin chains¹¹. DUBs add an additional regulatory control step prior to protein degradation and are responsible for maintaining a free pool of mono-ubiquitin for protein degradation¹².

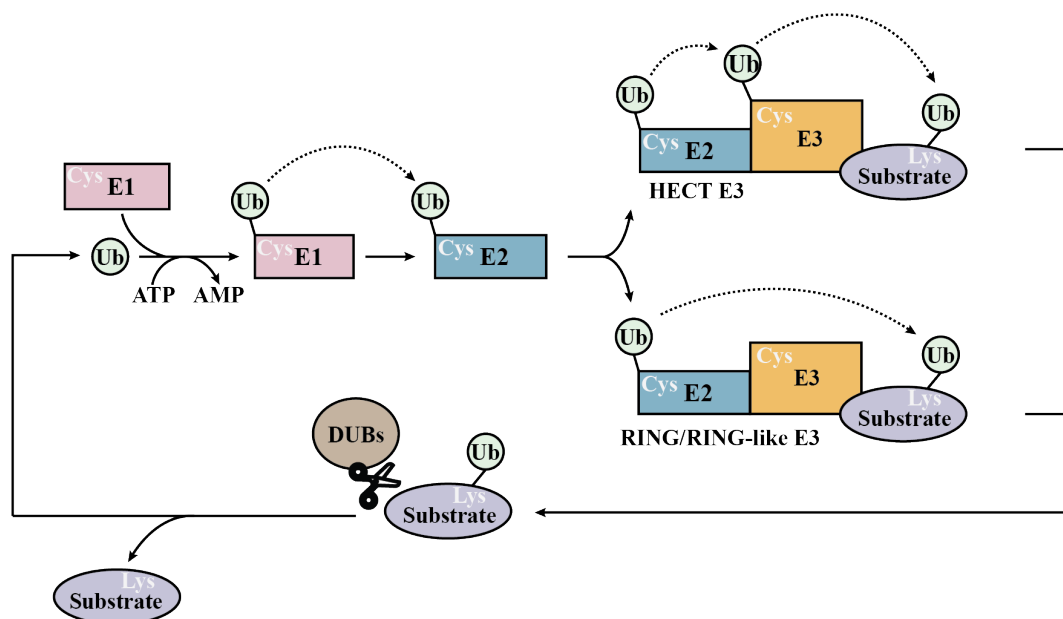


Figure 1.1: Overview of the ubiquitin conjugating mechanism. Ubiquitin molecules (Ub, green) are attached to substrate proteins (purple), which are destined for degradation. Ubiquitination results in the formation of a bond between the C-terminus of ubiquitin with the ϵ -amino group of a lysine of the substrate. In the UPS, a well-defined series of enzymes take part in the (poly-)ubiquitination reaction. Ubiquitin is first activated by the E1 enzyme (pink) under ATP hydrolysis and subsequently transferred to the E2 conjugating enzyme (turquoise). Next, the E3 ubiquitin ligase (orange) determines the transfer of ubiquitin to the substrate protein. Here, the transfer varies between the two major classes of E3 ubiquitin ligases, termed HECT and RING-like^{13,14}. The ubiquitin-tagged substrate is then targeted by the 26S proteasome for degradation (not shown). Ubiquitination is reversed by deubiquitinating enzymes (DUBs, brown). DUBs remove ubiquitin from proteins and disassemble polyubiquitin chains. Modified from Ravid and Hochstrasser¹⁵.

1.2 The 20S and 26S Proteasome

1.2.1 The 20S Proteasome - Structure and Function

The 20S proteasome is a large macromolecular complex of approximately 750 kDa, comprising 28 subunits arranged in four co-axially stacked heteroheptameric rings (Figure 1.2). The inner rings are formed by seven distinct β -subunits, whereas the outer rings consist of seven different α -subunits. Three β -subunits contain proteolytic active sites ($\beta 1$, $\beta 2$, $\beta 5$), belonging to the N-terminal nucleophile hydrolase family. These subunits are located deep within the barrel-shaped structure of the core particle, likely to avoid any unspecific degradation events and also to maintain a controlled, sequential degradation of substrates¹⁶.

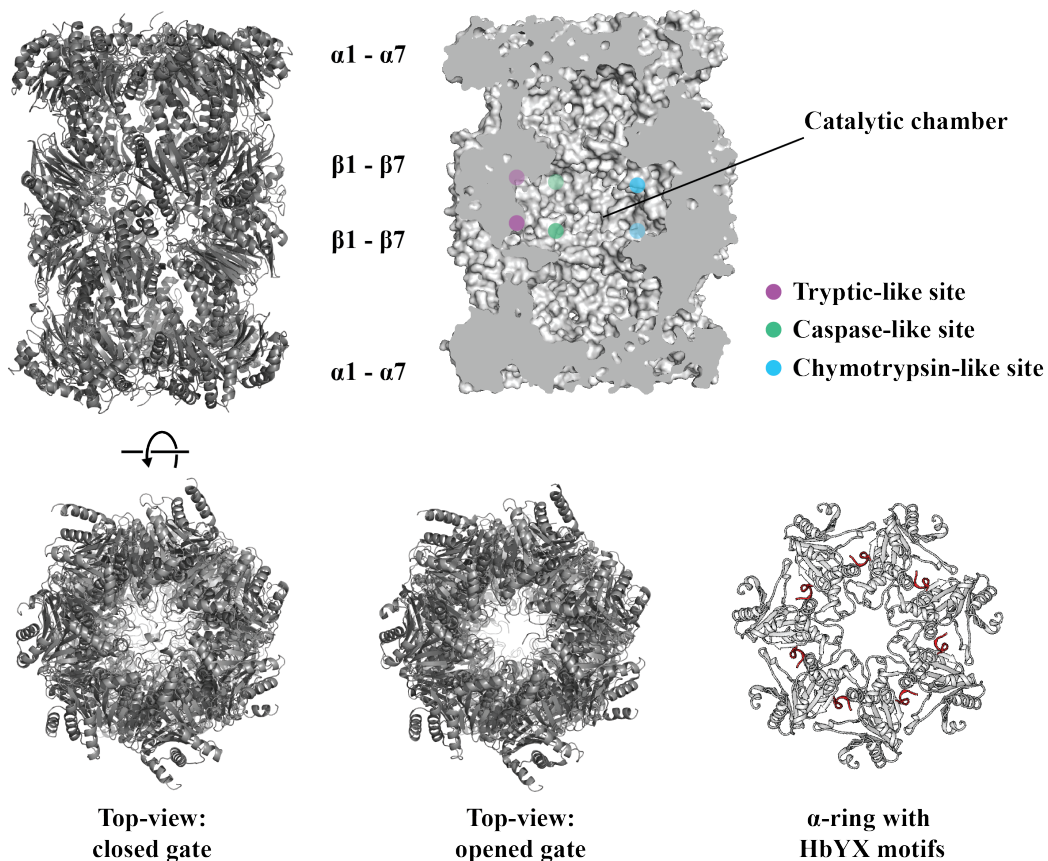


Figure 1.2: Structural details of the 20S proteasome. Top: Side view and cross section of a space-filling representation of the yeast 20S proteasome (PDB ID: 1RYP)¹⁶. Purple dots denote the spatial position of the $\beta 2$ (tryptic-like), green dots the $\beta 1$ (caspase-like), and blue dots the $\beta 5$ (chymotrypsin-like) active site, respectively. Bottom: Top view on the 20S proteasome. Bottom left: Wild-type yeast 20S proteasome (PDB ID: 1RYP), representing a closed gate. Bottom middle: Opened-gate mutant of the yeast 20S proteasome (PDB ID: 1G0U)¹⁷. Bottom right: View onto the α -ring of the 20S particle form *T. acidophilum*, in complex with the PAN C-terminus. The HbYX-motifs (red) which are inserted into the pockets formed at the interfaces of two adjacent α -subunits are shown. The HbYX motifs bind to a lysine residue in the α -pocket. Modified from Kriegenburg et al.¹⁸

Each active site cleaves preferentially after particular amino acid residues: (1) The β 1 subunit has been classified as a caspase-like active site, because cleavage occurs after acidic residues, (2) β 2 harbors a tryptic-like activity, cleaving after basic residues, and (3) β 5 is termed chymotryptic-like, because cleavage occurs preferentially after bulky hydrophobic residues¹⁹. Studies have determined that the 20S proteasome shows preference for certain peptide bonds over others for cleavage. The active sites are much less specific with regard to the recognition of certain amino acid residues in P1 position than classification based upon fluorogenic peptide substrates would suggest²⁰. According to a model by Schechter and Berger²¹, amino acid residues in a substrate undergoing cleavage are designated P1, P2, P3, P4 etc. in the N-terminal direction from the cleaved bond.

The 20S proteasome has a narrow channel in the center of the outer α -rings that only allows the passage of unfolded polypeptides, which then access the inner chamber and proteolytic active sites. The N-terminal tails of the α -subunits form a gate, its closed or open states prevent or allow the passage of substrates through the channel, respectively (Figure 1.2)¹⁷. To function *in vivo*, the 20S proteasome needs to associate with regulatory particles that partially determine the specificity of protease function.

The 20S proteasome is highly conserved from archaea to higher eukaryotes. The striking features of this protease were structurally analyzed by X-ray crystallography and electron microscopy. Atomic structures of the 20S proteasome from yeast and mammals have been determined and their overall structures and subunit arrangements are nearly identical^{16,22,23}.

X-ray crystallography is a method that enables to gain three dimensional structures of biological molecules at resolutions below 1 Å. The resolution of a structure measured in Ångström (Å) is an important indicator towards its quality and reliability. Resolution in general describes the distance of two points which can be significantly discerned from each other. To determine a structure's resolution, one can directly investigate the structural features (Figure 1.3): Structures around 20 Å show the overall shape. Molecular details are difficult to interpret in structures between 20 and 10 Å, though proteins and domains can be assigned. Between 9 and 6 Å alpha helices become visible. Details begin emerging around 5 Å when secondary structure elements can be determined; β -sheets become separated and bulky side chains become visible. Starting at 4 Å more side chains appear in the density. Nucleotide bases start being separated and most side chains are visible at a resolution of 3.5 Å. In crystal structures resolved to 2 Å, most of the rotamers appear in their correct conformation and at 1.6 Å the electron density is well enough defined to see holes in aromatic amino acids. From 1.1 Å resolution, the electron density allows positions of hydrogen atoms to be resolved.

The first crystal structure of the 20S proteasome was published in 1996 and revealed details of the *Thermoplasma acidophilum* 20S proteasome at a resolution of 3.4 Å²⁴. In the

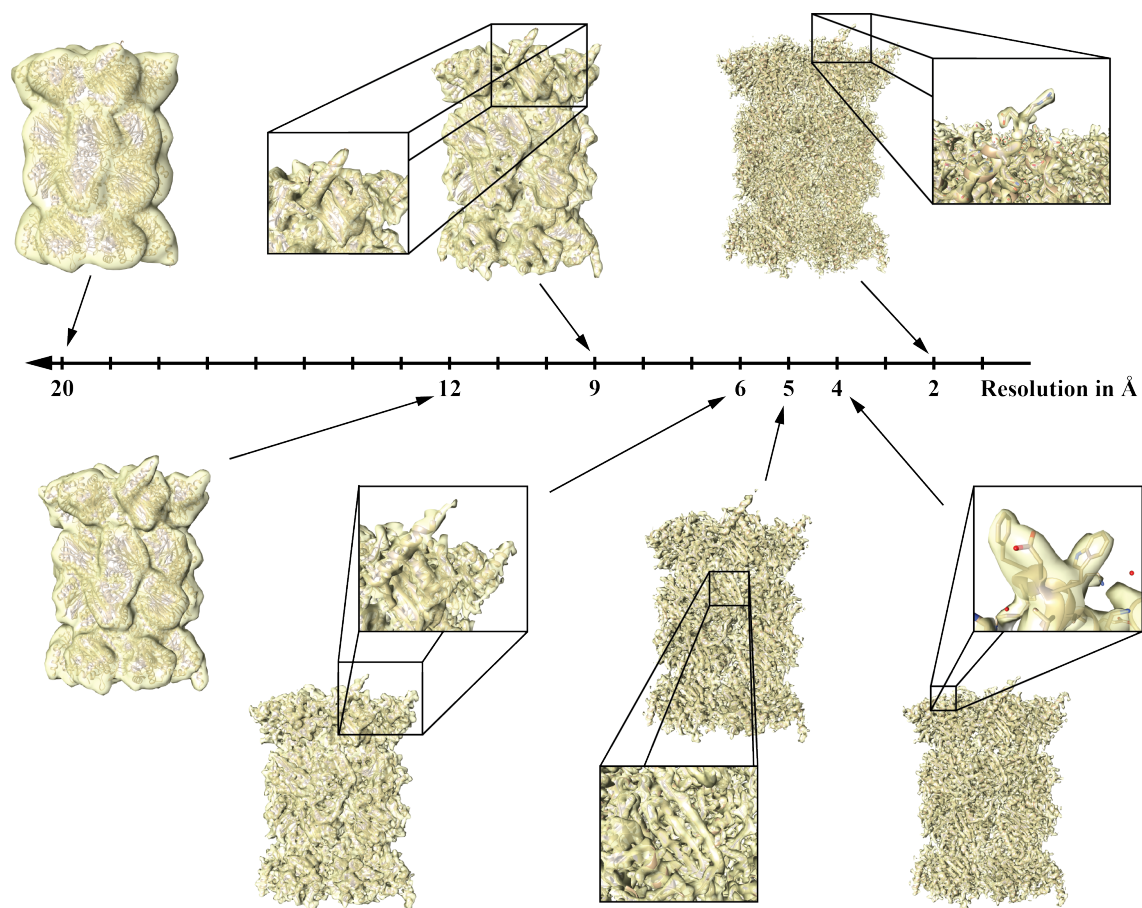


Figure 1.3: Structural details at distinct resolutions. The atomic model of the 20S proteasome is filtered to different resolutions. The depicted resolutions are defined by features which become visible in the structure. At 20 Å, the overall shape of the 20S proteasome is recognizable. Individual domains become visible at 12 Å and at 9 Å the α -helices are structurally defined. Between 6 and 5 Å β -sheets get separated. Starting at 4 Å, side chains become visible increasingly until at 2 Å all side chains are visible.

following years, 20S proteasomes from yeast (*S. cerevisiae*)¹⁶ and mammals (*Bos taurus*²³ and *Mus musculus*²²) were presented at resolutions between 2.4 and 3.2 Å, as well as the human 20S proteasome structure at 2.6 Å resolution²⁵. Superposition of the individual catalytic β -subunits revealed that the structures from different organisms adopt very similar folds. Further, the superpositions of the α -ring of the human proteasome with the α -ring of the proteasomes from *S. cerevisiae*, *Bos taurus* and *Mus musculus* illustrates high structural conservation²⁵.

In the crystal structures of free 20S proteasomes from higher organisms, the entrance to the internal proteolytic chamber containing catalytic sites is usually closed by the N-terminal tails of the α -subunits¹⁶. In yeast, the N-termini of the α 1, α 2, α 3, α 6, and α 7 fill the opening in several layers (Figure 1.2). It is assumed that this gate must be opened for substrate processing in fully activated proteasomes¹⁷. Only substantial rearrangements would allow access of peptide substrates into the catalytic chamber¹⁷.

1.2.2 The 20S Catalytic Mechanism - Proteolysis

Despite the fact that the catalytic sites of the 20S proteasome are unique in their chemical nature of substrate-binding and substrate preference, all sites employ an identical reaction mechanism for hydrolysis of the substrates peptide bonds. All three β -type subunits contain catalytically active threonine residues at their N-termini and employ a N-terminal nucleophile (Ntn) hydrolase activity.

The catalytic system is formed by the N-terminal threonine (Thr1), providing both the catalytic nucleophile and the primary proton acceptor, together with Glu17 and Lys33, first described in *T.acidophilum*^{24,26}. With structural and mutational studies it became clear that the residues Ser129, Ser169 and Asp199 in close proximity to Thr1 are required for catalysis^{26,24}. Additionally, Groll et al. proposed a fully occupied solvent molecule (NUK) in all three catalytic sites of the yeast 20S proteasomal complex. This molecule might be located close to the Thr1 O γ and N, Ser129 O γ and N and Gly47 N¹⁶.

With this knowledge a mechanism for proteolysis was proposed by Groll et al.:

During proteolysis, a nucleophilic attack of the hydroxyl group of Thr1 on the carbonyl carbon atom of the peptide bond takes place and the first cleavage product and a covalent acyl-enzyme intermediate are created. Next, the NUK water molecule, localized in close proximity to the Thr1 acts as a proton shuttle to regenerate the enzyme and the peptide fragment is released¹⁶. The mechanism of substrate proteolysis is depicted as a schematic representation in Figure 1.4.

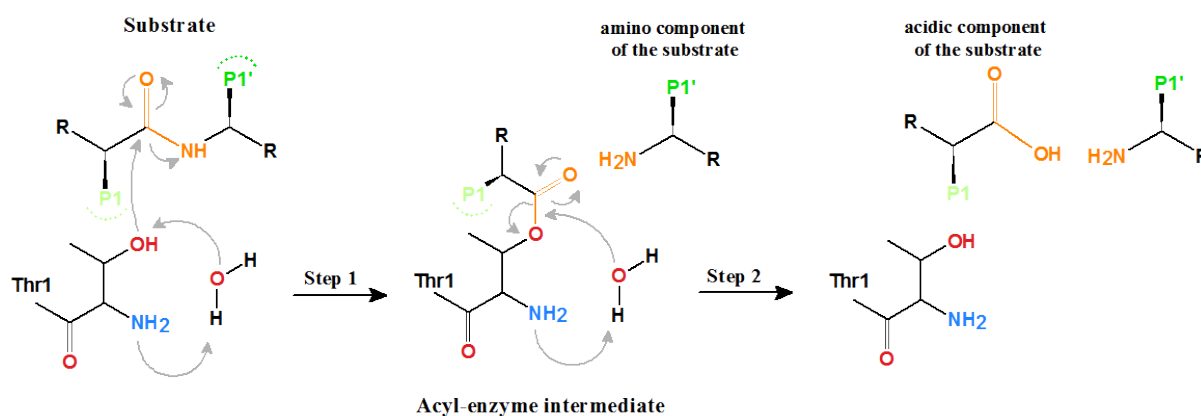


Figure 1.4: Substrate proteolysis. Schematic representation of the proteolytic cleavage mechanisms of the 20S proteasome. The substrates peptide bond is hydrolyzed by the N-terminal Threonine of the proteolytic active β subunit.

1.2.3 The 26S Proteasome - Structure and Function

The 2.5 MDa 26S proteasome is a large and complex member of the superfamily of ATP-dependent "chambered" proteases found in all domains of life^{27,7}. The human 26S proteasome is a labile complex that can dissociate into the 20S core particle (CP) and the 19S regulatory particle (RP). The 20S particle exhibits the proteolytic activity and the 19S regulatory particle is responsible for substrate recognition, deubiquitination, unfolding and translocation of substrates into the core particle. The regulatory particle consists of at least 19 subunits, whereby the particle can split into two distinct assemblies: the lid and the base (Figure 1.5).

The base consists of nine subunits: Rpt1-6 (regulatory particle triple A protein 1-6) are paralogous AAA+ ATPases and Rpn1, 2, 10 and 13 (regulatory particle non-ATPase) are non-ATPases. The six RP triphosphatases form a heterohexameric ATPase ring with the arrangement Rpt1-Rpt2-Rpt6-Rpt3-Rpt4-Rpt5²⁸, typically converting ATP hydrolysis into mechanical force and being in direct contact with the α -ring of the core particle. Rpn1 and 2 are the largest subunits of the proteasome, exhibiting α -helical proteasome/cyclosome repeats (PC), which function as a docking platform for extrinsic ubiquitin receptors and deubiquitinating enzymes (DUBs). Rpn13 and Rpn10 directly recognize and bind ubiquitin, acting both as intrinsic receptors for polyubiquitinated substrates. With a position in the periphery of the proteasome, the ubiquitin receptors Rpn10 and Rpn13 sit in a perfect orientation to take part in the first steps of substrate recognition (Figure 1.5).

The RP lid consists of nine different Rpn subunits: Rpn3, 5-9, 11, 12 and Rpn15, whereby six of them are Proteasome/CSN/Initiation complex (PCI) domains (Rpn3, 5, 6, 7, 9, and 12). The PCI domain is a purely α -helical domain of approximately 200 amino acid residues, which is generally localized at the extreme C-terminus of the protein. Rpn8 and Rpn11 are two MPN subunits, forming a heterodimer. The MPN domain spans approximately 140 amino acid residues present at the N-terminus of the proteins. Both the PCI and MPN domains might serve as structural scaffolds to uphold the proteasome's complex structure²⁹. Rpn15 (DSS1 in human) is a small acidic domain involved in ubiquitin-substrate binding³⁰. Rpn11 belongs to the DUBs. Structurally, the Rpn11 subunit sits above the central pore of the AAA+ ATPase with its catalytic MPN domain³¹. Due to its central position, Rpn 11 might be the primary DUB in proteasome degradation and is able to cleave off the entire ubiquitin chain from substrates which are directed from the 19S regulatory particle to the central pore of the 20S core particle (Figure 1.5). Mutations of Rpn11 in yeast show that the activity of the domain is linked to severe growth defects³².

In addition to the 19S proteasomal subunits, a number of proteins associate with the proteasome via loose, salt-labile interactions. These proteins play important roles in reg-

ulating the proteolytic function³³. Some serve as alternative ubiquitin receptors, such as the UBL/UBA domain containing proteins Rad23 (radiation sensitive 23), Dsk2 (dominant suppressor of Kar2) and Ddi1 (DNA damage-inducible 1), which help to deliver specific ubiquitin conjugates to the proteasome³⁴. For example, proteins which trim or extend the ubiquitin chains of substrates on the regulatory particle are the deubiquitin enzyme Ubp6/USP14 (ubiquitin-specific protease 6 in yeast and 14 in mammals) and the ubiquitin ligase Hul5 (HECT ubiquitin ligase 5 in yeast) and its mammalian ortholog, KIAA10^{35,36}.

Within the 26S proteasome one of the contacts between 20S and 19S particles occurs through the Rpn5 and Rpn6 lid domains, with their N-termini extended towards the $\alpha 1$ and $\alpha 2$ subunits of the 20S particle³¹. This allows a direct interaction between the lid and the core particle. The main contact between 19S and 20S particles was found between the α -subunits of the 20S and the conserved HbYX (hydrophobic, tyrosine, any amino acid) motifs at the flexible C-termini of the ATPase domains³⁷. The HbYX regions can dock at the $\alpha 3/\alpha 4$, $\alpha 1/\alpha 2$, and $\alpha 5/\alpha 6$ pockets between alpha subunits, shown by crosslinking experiments³⁸. The details of these interactions are not conclusively clarified, but it is thought that binding of all three HbYX motifs to the α -ring will cause it to undergo a conformational change that better allows for substrate entry into the proteolytic chamber^{16,17}. In Figure 1.2 the α -ring of the 20S particle from *T. acidophilum* together with the inserted HbYX motifs from the PAN C-terminus are shown.

Besides the ATP-dependent activator 19S there are a number of different types of "caps" or activators of the 20S particle. The 11S cap (proteasome activator 28/PA28/REG) and the bleomycin-sensitive 10 cap (Blm10/PA200), which stimulate the degradation of substrates without ATP hydrolysis and ubiquitin detection³⁹. The AAA+ ATPase p97 (CDC48/VCP) might also serve as an alternative cap, first shown for proteasomes from *T. acidophilum* and later for mammalian proteasomes^{40,41}. Complexes of the 20S core particle with one 19S regulatory particle on one end and another activator such as 11S or Blm10 on the other end are reported and referred to as hybrid proteasomes.

In general, the 26S proteasome is a dynamic molecular machine. As a consequence, this multiprotein complex is biochemically labile or unstable, especially when isolated from the cell. It is therefore challenging to work with these proteases, either for biochemical assays or structural studies. Still, during recent years, a series of cryo-EM reconstructions of the 26S holoenzyme as well as of the isolated RP or lid were published and provide a much clearer picture of its architecture.

The overall shape of the molecule was observed long ago, but only recently published structures give insights into the structural arrangements of the subunits within the complex. In 2010, the first subnanometer-resolution structure of the complete 26S proteasome was presented and individual subunits could be placed into the model⁴². Only over the

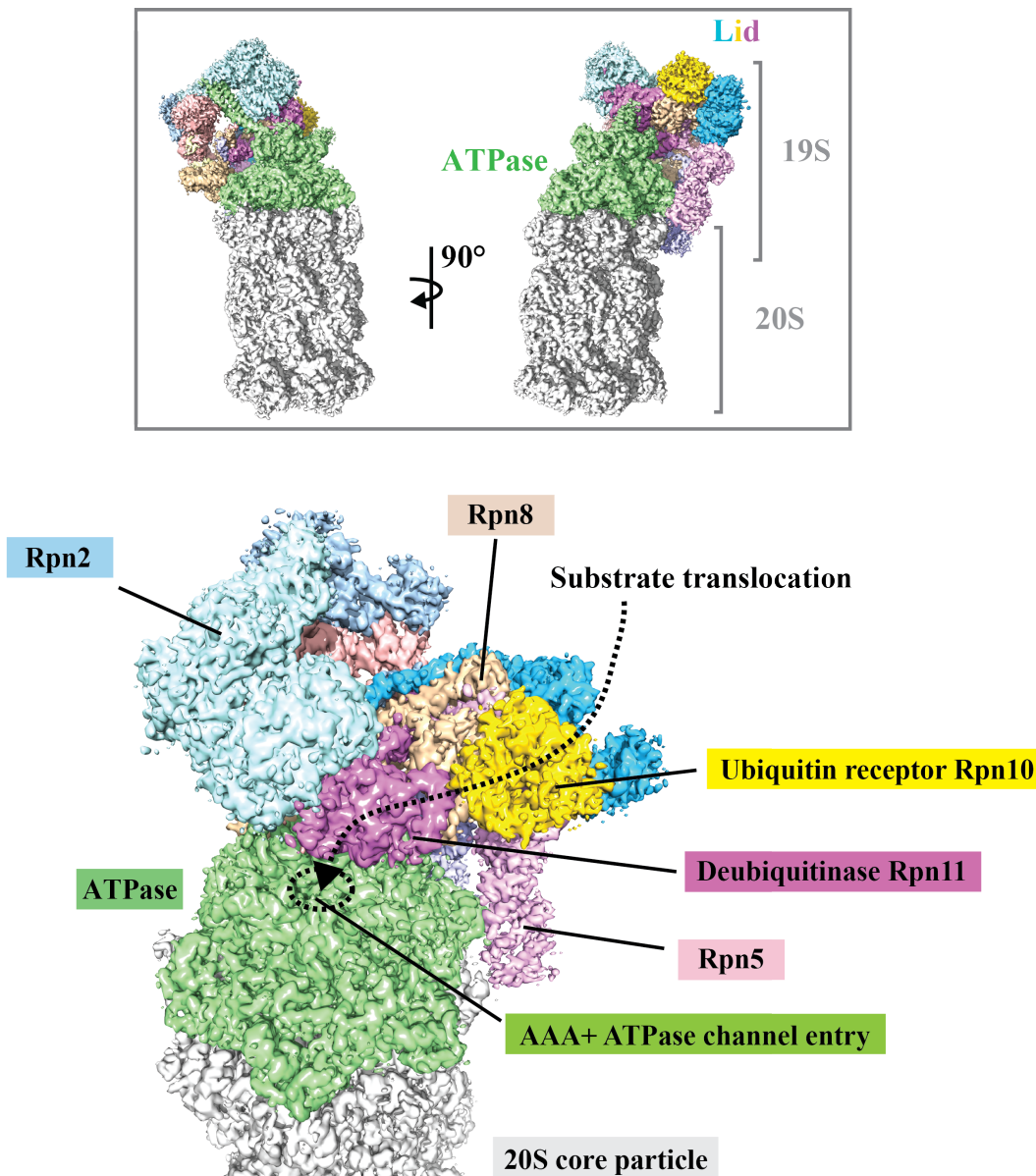


Figure 1.5: Structure of the 26S proteasome. Upper box: Architecture of the 26S proteasome, consisting of the 20S core particle, ATPase and Lid-complex. Bottom: Half-top view onto the Lid/ATPase. Dashed arrow gives the direction of substrate translocation: Substrate is detected by one of the ubiquitin receptors (Rpn10, yellow) of the lid complex, ubiquitin is recycled by the deubiquitinating lid enzyme Rpn11 (purple) and enters the 20S core particle by a translocation through the pore of the AAA+ ATPase.

past 4 years several publications revealed the structure of the yeast and human 19S particle and the 26S holoenzyme at higher resolutions^{31,43,42,44,45} with recently published structures of the human 26S proteasome at 3.9, 3.5 and 4.4 Å resolution, respectively^{46,47,48}. An unexpected feature regarding the core particle and regulatory particle interaction was found in electron microscopic data of *D. melanogaster* and *S. pombe* 26/30S proteasomes: The pore of the heteroheptameric AAA+ ATPase ring of the regulatory particle does not align with the pore of the 20S core particle. It is shifted axially by almost 30 Å and tilted vertically by 5-10°⁴⁹. The functional significance of the disalignment was not known, but

recent structural data from the yeast proteasome offers an explanation for this offset. Three major conformational states of the proteasome holoenzyme have been found by cryo-EM analysis: S1, S2 and S3⁵⁰. These states form the basis for a hypothesis of ubiquitin/substrate binding, deubiquitination, substrate unfolding and translocation by the proteasome. S1 is defined as the ground state, which is the predominant state under ATP hydrolysis and without substrate present in the condition. In contrast, the S3 state is present upon excess of substrates⁵¹ or by introducing the non-hydrolyzable ATP analogue ATP γ S⁵⁰ to the system. S2 is a hybrid state between S1 and S3. It is proposed that docking of substrates occurs in the S1 state, considered the *substrate-accepting state*, followed by a structural rearrangement when the substrate is accepted for degradation in S2 state. Finally, the substrate is unfolded, ubiquitin is removed and the substrate is translocated into the 20S core particle for degradation in conformational state S3, the *substrate-processing state*. The main conformational rearrangements are a rotation of the lid by 25° and a translation and rotation of the AAA+ ATPase in relation to the 20S core particle, resulting in an alignment of the ATPase ring and the core particle channel in S3.

Table 1.1: 26S proteasome subunits. Listed are all subunits belonging to the core and regulatory particle of the 26S proteasome.

Subunit Name	Subcomplex	Function	Activity/domain
$\alpha 1$	20S core particle	Scaffolding/gating	
$\alpha 2$	20S core particle	Scaffolding/gating	
$\alpha 3$	20S core particle	Scaffolding/gating	
$\alpha 4$	20S core particle	Scaffolding/gating	
$\alpha 5$	20S core particle	Scaffolding/gating	
$\alpha 6$	20S core particle	Scaffolding/gating	
$\alpha 7$	20S core particle	Scaffolding/gating	
$\beta 1$	20S core particle	Protease	Caspase-like
$\beta 2$	20S core particle	Protease	Tryptic-like
$\beta 3$	20S core particle	Scaffold	
$\beta 4$	20S core particle	Scaffold	
$\beta 5$	20S core particle	Protease	Chymotryptic-like
$\beta 6$	20S core particle	Scaffold	
$\beta 7$	20S core particle	Scaffold	
	Base		
Rpt1	19S regulatory particle	Unfoldase	AAA+ ATPase
Rpt2	19S regulatory particle	Unfoldase	AAA+ ATPase
Rpt3	19S regulatory particle	Unfoldase	AAA+ ATPase
Rpt4	19S regulatory particle	Unfoldase	AAA+ ATPase
Rpt5	19S regulatory particle	Unfoldase	AAA+ ATPase
Rpt6	19S regulatory particle	Unfoldase	AAA+ ATPase
Rpn1	19S regulatory particle	Substrate recruitment	PC repeats
Rpn2	19S regulatory particle	Rpn13 docking	PC repeats
Rpn10	19S regulatory particle	Ubiquitin receptor	vWA/UIM domain
Rpn13	19S regulatory particle	Ubiquitin receptor	PRU domain
	Lid		
Rpn3	19S regulatory particle	Ubiquitin receptor	PCI domain
Rpn5	19S regulatory particle	Ubiquitin receptor	PCI domain
Rpn6	19S regulatory particle	Ubiquitin receptor	PCI domain
Rpn7	19S regulatory particle	Ubiquitin receptor	PCI domain
Rpn8	19S regulatory particle	Ubiquitin receptor	JAMM/MPN+ domain
Rpn9	19S regulatory particle	Ubiquitin receptor	PCI domain
Rpn11	19S regulatory particle	Deubiquitylation	JAMM/MPN+ domain
Rpn12	19S regulatory particle	Scaffold	PCI domain
Rpn15	19S regulatory particle	Ubiquitin receptor	IDP

1.3 Proteasome Inhibition

The proteasome is a key molecular complex for the degradation of proteins that control the cell division cycle and apoptosis. It is therefore an interesting target for therapeutic agents that inhibit cell proliferation in diseases such as cancer. Proteasome inhibition is an accepted antineoplastic strategy since the approval of Bortezomib in 2003⁵². Within nine years, Bortezomib was raised from development to its first approval by the US Food and Drug Administration (FDA) for the treatment of multiple myeloma, with an annual sales value of two billion US Dollars. The success of Bortezomib has drawn further interest in proteasomes as targets in oncology, and today at least five other compounds are at various stages of clinical approval for treatment of multiple myeloma, a cancer of plasma cells^{53,54}.

Inhibition of proteasomes leads to the accumulation of misfolded proteins and the formation of toxic, reactive oxygen species. At the same time it induces apoptosis in cancerous cells, which lack the ability to enter cell cycle arrest⁵⁵. In preclinical studies, researchers studied the effectiveness of proteasome inhibitors on different types of cancers and found a selectivity for malignant cells^{56,57}. It was found that actively proliferating malignant cells are more sensitive to proteasomal inhibition than non-cancerous cells^{58,59}. The underlying mechanisms of the increased susceptibility of malignant cells are not yet completely understood. Malignant cells have characteristics that might play a role in the biological basis for this cytotoxic mechanism: malignant cells proliferate rapidly and have therefore an increased demand for proteasomal degradation. This hypothesis is consistent with findings in studies of lymphocytes. Chronic Lymphocytic Leukemia (CLL) lymphocytes have a three-fold higher activity of the chymotryptic-like active site and an upregulated ubiquitin-proteasome system with higher levels of ubiquitin-conjugated proteins compared to healthy lymphocytes⁶⁰. Inhibition of the proteasome in cancerous lymphocytes would result in an accumulation of proteins and terminate in apoptosis.

The first clinically approved drug Bortezomib revealed substantial off-target activity by reacting with various enzymes that results in severe side effects⁶¹. Furthermore, resistance to this drug remains a clinically significant problem⁶². In recent years, second-generation competitive inhibitors have been discovered and many are under evaluation by the FDA. The design principle for these inhibitors involves a combination of a peptide moiety coupled with a reactive head group acting as electrophilic anchor, such as for example α',β' -epoxyketones, boronates, aldehydes, α -ketoaldehydes, vinyl sulfones or β -lactones. Most of the recently published structural knowledge about proteasome inhibition including the mechanism of inhibitor binding and the binding-site composition derives from studies of the yeast 20S proteasome. Only little is known about the inhibitory mechanisms in the human system, whereas it is assumed that inhibition takes place in a similar

manner. The first structures of the human 20S proteasome in complex with inhibitors were only recently determined by X-ray crystallography and electron microscopy at resolutions of 2.9 Å and 3.5 Å, respectively^{25,63}. Due to the relatively low resolution of these structures, direct observations of atomic details, especially at the binding site of inhibitors, was not possible. Nevertheless, predicted models for the inhibition mechanism of various inhibitor classes were published and are presented in the following sections. Structures of different 20S proteasome-inhibitor complexes were elucidated and analyzed for this thesis. Numerous inhibitors are described in literature, but only a selection of inhibitor classes was investigated in this thesis (Figure 1.6). In the following, the relevant inhibitor classes are listed and briefly described: 1) Boronic acid inhibitors, including the Bortezomib inhibitor with a lead in anti-cancer therapy over the last years, 2) Epoxyketone inhibitors that are a highly potent and customizable class of inhibitors, and 3) α -Ketoaldehydes, which were discovered in the 1990s but neglected for several years because their benefit over other inhibitor classes was not understood at that time.

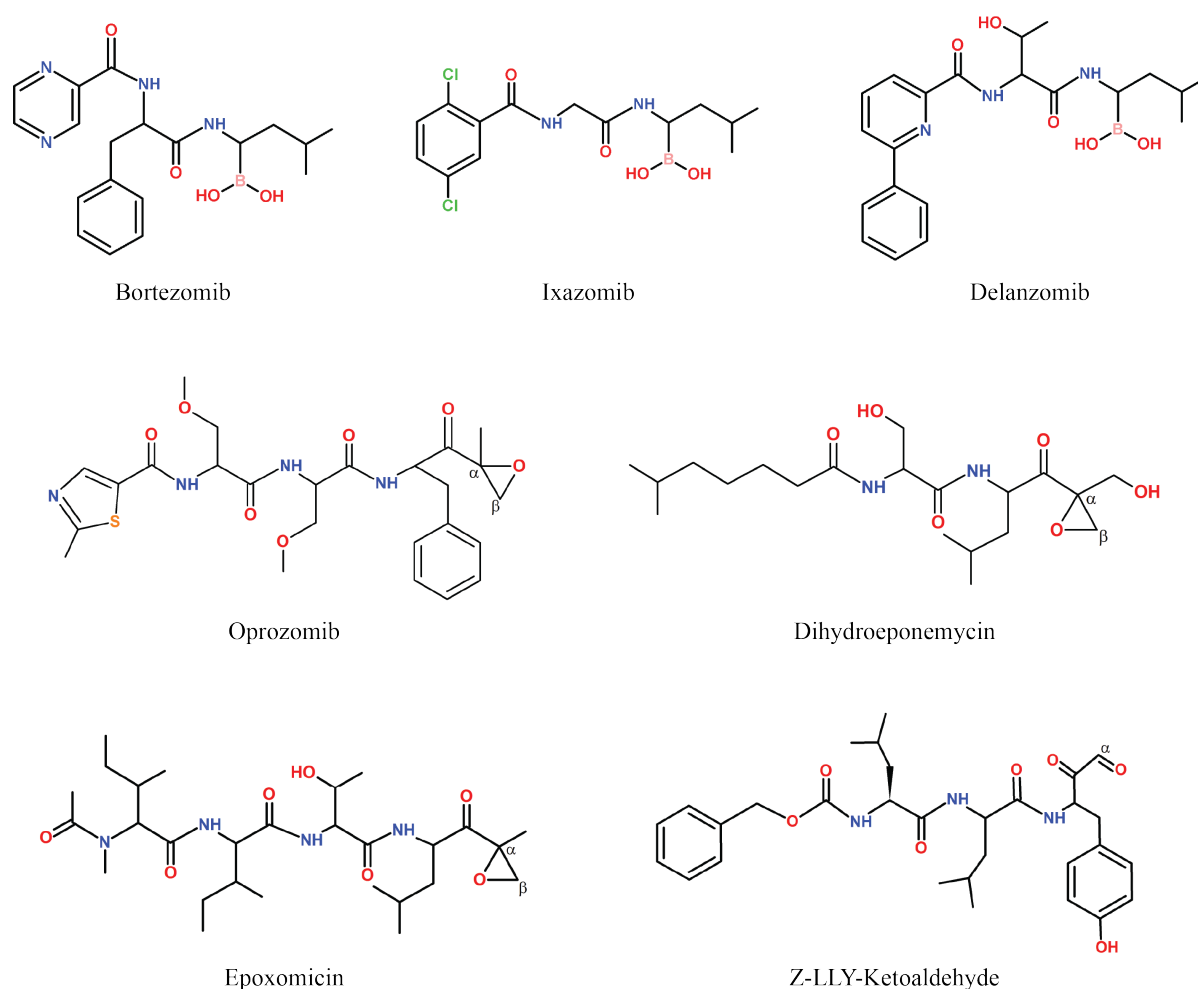


Figure 1.6: Chemical structures of proteasome inhibitors. Chemical structures of the boronic acid inhibitors Bortezomib, Ixazomib and Delanzomib. Oprozomib, Dihydroeponemycin and Epoxomicin belong to the group of α,β -epoxyketone inhibitors. Z-LLY-Ketoaldehyde represents the α -ketoaldehyde inhibitors.

1.3.1 Boronic Acid Inhibitors

Bortezomib, along with other boronic inhibitors is highly potent and inactivates the proteasomal active site by a covalent but slowly reversible binding mode. Boronic acid inhibitors covalently react with the nucleophilic Thr10 γ of the 20S proteasome proteolytically active subunits. Bortezomib was developed after successful proteasome inhibition was shown for the natural agent lactacystin and synthetic aldehyde inhibitors. Bortezomib is based on the substitution of the aldehyde with boronic acid to gain a compound which forms a covalent, reversible complex and exhibits an improved selectivity for proteasomal active sites compared to corresponding aldehydes⁶⁴.

Bortezomib was the first proteasome inhibitor to enter clinical trials and to be approved for cancer therapy, but despite prolonging the lifetime of multiple myeloma patients, Bortezomib shows severe side effects like neuropathy. In addition, patients often develop resistance and treatment requires an intravenous or subcutaneous injection, which is not ideal. Still, the positive clinical outcome of Bortezomib treatment provided a motivation for the discovery and development of next-generation proteasome inhibitors with higher efficiency and enhanced tolerability.

One of the next-generation boronic acid inhibitors is an orally bioavailable proteasome inhibitor, Ixazomib (MLN2238). Approved by the FDA in 2015, Ixazomib is used for the treatment of multiple myeloma patients with selectivity and potency similar to that of Bortezomib. This reversible proteasome inhibitor preferentially binds to and inhibits the $\beta 5$ active site of the 20S proteasome, whereby at higher inhibitor concentrations Ixazomib also inhibits the $\beta 1$ and $\beta 2$ activity^{65,66}.

A third boronic proteasome inhibitor, Delanzomib (CEP-18770), is currently in clinical trials. Delanzomib is orally deliverable and has been investigated in Phase I clinical trials for treatment of solid tumors, leukemia and non-Hodgkin's lymphoma⁶⁷. Delanzomib was developed to inhibit the $\beta 5$ chymotryptic-like site of the proteasome⁶⁸. However, it also co-inhibits the caspase-like site ($\beta 1$) in a concentration-dependent manner⁶⁹.

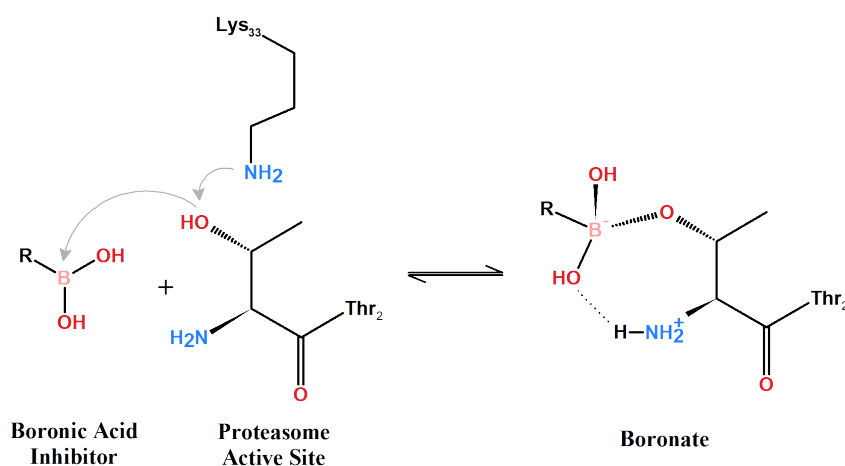


Figure 1.7: Mechanism proposed for boronic acid inhibitors. Schematic representation of the inhibition mechanism of boronic acid inhibitors.

1.3.2 Epoxyketone Inhibitors

The epoxyketone class of inhibitors are known for their specificity and potency, with no evidence of off-target effects. The first structural analysis of epoxyketone inhibition was carried out in *S. cerevisiae* 20S proteasomes. These studies proposed a possible mode of proteasome inhibition by the epoxyketone inhibitor Epoxomicin⁷⁰. The inhibitor binds to the Thr1 in the β 5, chymotryptic-like active site by a formation of a six-membered morpholine ring linkage. The morpholine 6-ring structure formation is described as a 2-step process (Figure 1.8). First, activation of the Threonyl O γ occurs either via the N-terminal group of Thr1 or via a neighboring water molecule found in all active sites of the 20S proteasome. A nucleophilic attack of the Thr1O γ on the α,β -epoxyketone's carbonyl carbon forms a hemiacetal. Next, the free α -amino group of Thr1 opens up the epoxide ring and intramolecular cyclization takes place. The resulting 1,6-morpholino ring closure is formed, irreversibly inhibiting the active site.

Carfilzomib and its orally bioavailable analog ONX-0912 are two α',β' -epoxyketone inhibitors that are approved or in clinical trials by the FDA, respectively⁷¹. Carfilzomib is equally potent to the boronic acid inhibitor Bortezomib but more selective for the chymotryptic-like site of the catalytic core. The specificity and relatively simple synthesis made epoxyketone inhibitors a popular choice for the synthesis of many modifications with the result of hundreds of epoxyketones, including many subunit-selective and activity-based inhibitors⁷².

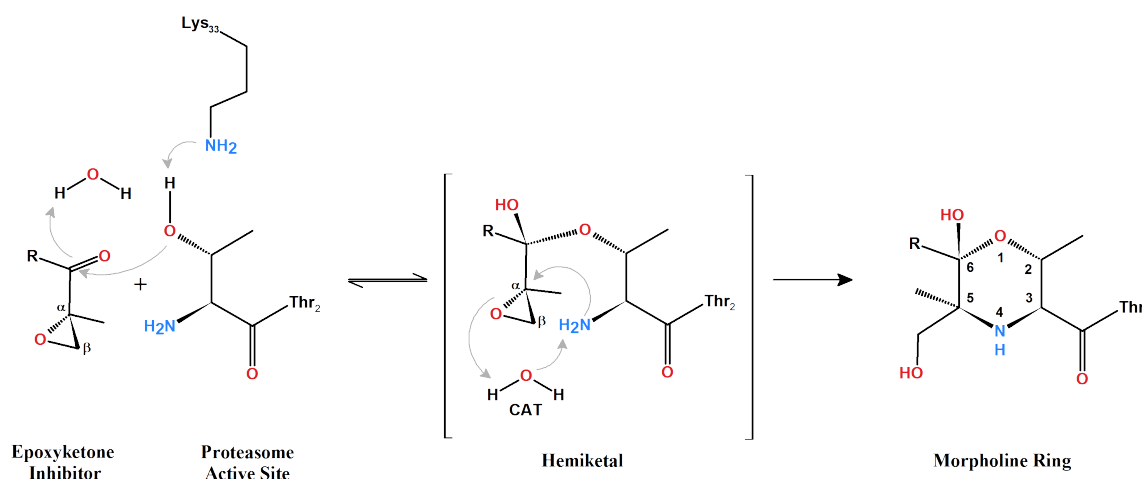


Figure 1.8: Mechanism proposed for α,β -epoxyketone inhibitors. Schematic representation of the proposed inhibition mechanism of α,β -epoxyketone inhibitors.

1.3.3 Ketoaldehyde Inhibitors

α -Ketoaldehyde inhibitors were first discovered in 1990, but only in 2011 first structural studies of the yeast 20S proteasome in complex with a ketoaldehyde revealed details

about the mode of action⁷³. Similar to epoxyketone inhibitors, a ring structure is formed upon inhibition, but unlike epoxyketones, the binding of an α -Ketoaldehyde is proposed to result in a 5,6-dihydro-2*H*-1,4-oxazine ring closure including a hemiketal and an imine bond (Schiff base). Formation of the hemiketal after the nucleophilic attack of Thr1 O γ proceeds as described for epoxyketone inhibition, but the second step encompasses a nucleophilic attack on Thr1N on the aldehyde carbon and a formation of a tetrahedral carbinolamine before releasing a water molecule and forming the rigid 6-membered ring. All steps towards the ring-formation are reversible, giving this class of inhibitors completely different pharmacological properties than those of irreversible epoxyketone morpholine-linkage inhibitors.

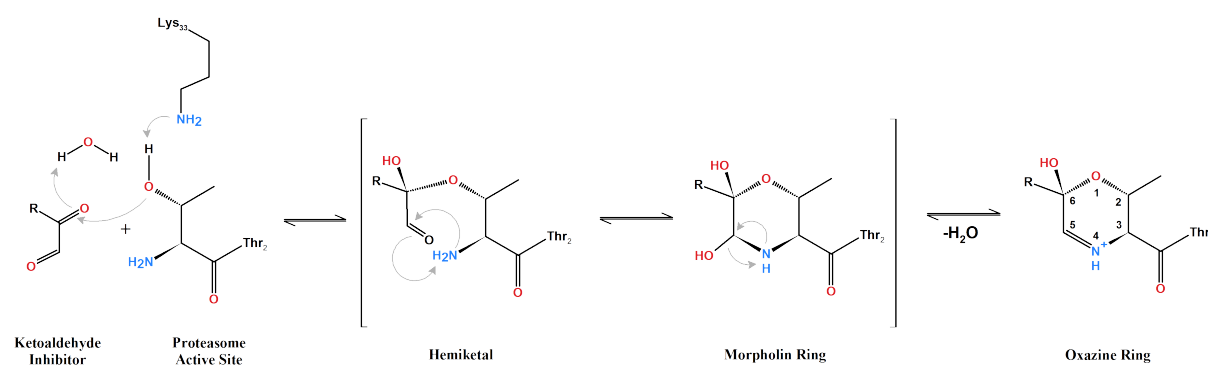


Figure 1.9: Mechanism proposed for α -ketoaldehyde inhibitors. Schematic representation of the proposed inhibition mechanism of α -ketoaldehyde inhibitors.

1.3.4 Recent Advances in Proteasome Inhibitor Development

Most of the proteasome inhibitors which are currently used as chemotherapeutics, or are in development are peptide-based covalent inhibitors. These compounds exert their inhibitory activity by a covalent interaction with the active site Thr1 O γ of the β -subunit. Covalent inhibitors are highly reactive, which leads to off-target interactions. In addition, the tissue distribution is very low due to slow dissociation kinetics, often inducing apoptosis and cell death *in vivo* of non-cancerous cells^{74,75}.

To overcome the disadvantages related to covalent inhibition, a concerted effort was put into development of noncovalent proteasome inhibitors, which bind the proteasome reversibly and time-limited. A number of classes of substrate-competitive and noncovalent proteasome inhibitors were identified and tested. These classes include Benzylamides, Oxadiazoles, and various natural products^{76,77,78,79,80,81}. For the development of new peptide-based noncovalent inhibitors extensive work has been carried out: New inhibitors were synthesized based on high-throughput screening of libraries including several hundred thousand compounds⁸².

In 2000, scientists discovered the natural product TMC-95A and its diastereomers B, C

and D from *Angiospora montagnei*, TMC-95A demonstrated a selective and competitive inhibition of the proteolytic activity of the 20S proteasome in a low molecular dose^{83,80}. These natural products were characterized as novel cyclic peptides, consisting of a heterocyclic ring system. TMC-95A inhibits all three catalytic sites of the 20S proteasome, shown by crystallographic studies⁸⁴. The mode of inhibition was described as noncovalent without modification of the N-terminal threonine upon inhibition. This noncovalent inhibitor binding is carried out by a specific network of hydrogens bonds. These interactions are between strictly conserved residues of the active sites with main-chain atoms of the inhibitor. TMC-95A adopts an antiparallel β -sheet structure with the peptide backbone as previously reported for α',β' -epoxyketone and aldehyde inhibitors^{16,24,80,83}. TMC-95A is favored over flexible ligands because its rigid ring structure prevents the inhibitor from structural rearrangements upon binding.

Currently many details of proteasome inhibition are known and a number of selective and potent inhibitors have been synthesized. A drug candidate with the optimal characteristics has not yet been found or produced. Results from biological assays as well as structural studies will help to improve existing inhibitors or to design new compounds that may provide better chemotherapeutic treatment solutions in the future.

1.3.5 Biological Implication of Proteasome Inhibition

Many cellular pathways are dependent on correct proteasome function. Several proteasomal substrates have essential tasks in cell-cycle regulation. Processing of these substrates by the proteasome are therefore essential. Important complexes involved in cell-cycle progression that depend on proteasome function are the cyclin-dependent kinase (CDK) complexes. CDK activity is regulated by short-living proteins, namely cyclins, which act at various stages of the cell cycle. The rapid turnover of cyclins is carried out by the UPS and only by an ordered and timed degradation of these small regulators can the continued growth of cells be sustained^{85,86}. Inhibition of the proteasome-mediated degradation of the cyclin proteins therefore results in reduced cell growth.

Furthermore, the proteasome controls apoptosis by affecting the nuclear factor of κ B (Nf- κ B). Nf- κ B transcription factors are bound to a specific inhibitor protein, I κ B, inactivating it and preventing it from activating transcription of its target genes. Upon stress, such as chemotherapy, radiation, viral infection and growth factors, I κ B is phosphorylated and subsequently degraded by the 26S proteasome^{87,88}, releasing Nf- κ B. Nf- κ B then translocates from the cytoplasm into the nucleus to activate transcription of a series of factors that promote cell growth and differentiation, and prevent apoptosis. Importantly, Nf- κ B initiates its own transcription and the transcription of its inhibitor I κ B, maintaining its own activity by positive feedback⁵⁷. By an inhibition of the proteolytic activity

of the proteasome, I κ B is stabilized in the cell and cancer cells are more vulnerable to chemotherapeutic or radiation treatments.

Proteasome function also influences the activation of the tumor suppressor p53⁸⁹. p53 is a short-lived protein with low quantities in the healthy eukaryotic cell. Cellular stresses such as chemical- or radiation-induced DNA damage, oxidative stress or oncogene activation cause p53 to accumulate in the cell, which triggers diverse cellular responses such as cell-cycle arrest. The cell efficiently regulates the cellular stress response by a feedback regulation via the p53-induced expression of MDM2 which then transports p53 from the nucleus to the cytoplasm and ubiquitinates p53 for rapid proteasomal degradation⁹⁰. Upon proteasome inhibition, p53 becomes activated and stimulates p53-mediated tumor-suppressor activity that result in apoptosis and senescence.

1.4 An Introduction to X-ray Crystallography and Single Particle Electron Cryomicroscopy

Understanding the chemical and biological functions, and mechanisms of macromolecular complexes often requires structural data with details at atomic resolution. Developments in technology and methodology over the last 20 years have paved the road to narrow the gap between two effective methods to study the structure of macromolecular machines: X-ray crystallography and single particle electron cryomicroscopy. In the present thesis both methods were utilized to analyze proteasome inhibition of either the 20S proteasome or the 26S holoenzyme. In the following section, a short introduction to both techniques is provided and the advantages and disadvantages of the techniques is presented.

1.4.1 X-ray Crystallography

X-ray crystallography is by far the oldest technique to investigate the structures of single molecules as well as macromolecular complexes. The discovery of X-rays by Wilhelm Conrad Roentgen in 1895 lead the way to its application in crystallography in the beginning of the 20th century and its first application in synchrotron radiation in the mid-1970s⁹¹. In 1958, John Kendrew unveiled the first protein structure, the structure of Myoglobin, a milestone in the history of structural biology⁹². Only two years later, Perutz published the structure of Hemoglobin⁹³. These milestones were achieved because a group of crystallographers around Perutz discovered the "method of isomorphous replacement" by which for the first time the crystallographic phase problem was overcome. Perutz discovered that heavy atoms could be attached to protein molecules and by this, the diffraction pattern would differ from crystals without heavy atoms. With this, phases of the reflections could be inferred for the first time^{94,95}.

In diffraction experiments, intensities of waves scattered from planes in the crystal are measured. The amplitude of the wave is proportional to the square root of the intensity measured on the detector. To calculate the electron density at a position in the unit cell, a summation of all planes is performed. Here, a certain electron density is the sum of contributions to the point of waves scattered from a plane, whose amplitude depends on the number of electrons in the plane, added with the correct relative phase relationship. This can be written mathematically as:

$$p(xyz) = 1/V \sum |F_{hkl}| \exp(i\alpha_{hkl}) \exp(-2\pi i hx + ky + lz) \quad (1.1)$$

where V is the volume of the unit cell, hkl is the crystal plane, the position in the unit cell is described as xyz and a_{hkl} is the phase associated with the amplitude $|F_{hkl}|$ ⁹⁶. The amplitudes can be measured but the phases are lost, which is known as the "phase problem".

For successful data collection a combination of the best possible instrumentation and a data collection strategy is needed. Today, diffraction patterns are measured at modern beamlines in synchrotron facilities with a very strong beam intensity, resulting in short exposure times. Data sets are collected with the oscillation photography method. The axes of the crystal are carefully aligned to the beam based on pre-screening of the crystal and the crystal is rotated around the set oscillation axis with diffraction patterns collected at defined angular distances.

Diffraction of protein crystals relies almost exclusively on scattering of X-rays by the electrons in the molecule resulting in spots measured on the detector during data collection. These spots have to be interpreted and incorporated into an overall dataset by scaling and merging. The amplitudes of interfering X-ray waves can be identified and the unit cell dimensions, crystal symmetry, and information of the molecular packing can be determined from the diffraction pattern intensities.

For calculating an electron density map, phase information has to be obtained. In addition to the method of isomorphous replacement introduced by Perutz, several experimental procedures to phase observed structure factor amplitudes were developed. One common way to determine phases is molecular replacement⁹⁷. Here, for example a reasonable homology model, can be used to provide an initial estimate for the phases. Besides this, a number of "direct methods" exist. *Ab initio* phasing is used when no phases from a structurally similar model are available, or if one wants to circumvent any kind of model bias by molecular replacement. To date, a standard *ab initio* method is still the Single or Multiple Isomorphous Replacement (SIR, MIR) method. Here, diffraction data from the native crystal and one or more crystals with derivatives, which produces a different diffraction pattern, is collected⁹⁸. Another approach is Single and Multiple Anomalous Dispersion (SAD, MAD)^{99,100}. Data is collected from a single crystal at several wavelengths, one wavelength at the absorption peak, one at the point of inflection and one at a remote wavelength. Whereas with SIR and MIR the protein phases are estimated from the additional scattering of the heavy metal atom crystals, in SAD and MAD the phases are calculated from wavelength-dependent quantitative differences in the anomalous scattering contribution of certain atoms contained within crystals.

Previously it was shown that phases for macromolecular complexes could be solved with anomalous scattering. The 30S ribosomal subunit from *B. Stearothermophilus* was solved by using the heavy atoms, osmium and lutetium at 5.5 Å resolution¹⁰¹. Similarly the fully assembled *T. thermophilus* 70S ribosome was phased with the anomalous scatterer iridium and solved to 7.8 Å resolution¹⁰².

Concluding the general X-ray crystallographic workflow, the determination of the initial phases is followed by the refinement of the phases, ending with a correct structural model. A model of the molecule is then built that agrees with both the information from diffraction in addition to biochemical knowledge.

Until today, X-ray crystallography has become the dominating method to determine three-dimensional structures of biological macromolecules. Synchrotron facilities that provide brilliant X-ray sources have extremely fast data-collection times and highly developed crystallographic methods form the basis to study macromolecules at very high resolution. Besides data collection and interpretation, one step for determining a three dimensional structure is fundamental: the crystallization of protein. The outcome of the crystallization procedure is determined by the choice of sample, optimization of the crystallization condition and post-crystallization treatments.

For the crystallization of macromolecular samples, the choice of the sample is often determined before starting with sample purification, or while searching for a suitable purification protocol. The initial step for crystallization is done when a reproducible purification strategy for the sample of choice is found and the soluble macromolecule can be prepared in viable quantities. For crystallization, the sample is then transferred into a solution, called mother liquor, in which it forms crystals. Finding a crystallization condition in which the flexible macromolecules arrange themselves in an ordered fashion can take time and often results in protein crystals which are fragile and need a complex post-crystallization treatment. Crystallization trials are performed in conditions that vary in buffer substance, pH, ions and precipitants. Besides the crystallization solution a number of factors are decisive for the optimal crystallization condition, including sample concentration, temperature and crystallization method. Most protein crystals are produced by the vapour diffusion method, either in hanging or sitting drop crystallization plates at temperatures ranging from room temperature (20-25°C) to temperatures close to the freezing point of water (0 °C). The setup for the vapour diffusion methods is relatively simple: A drop containing the protein sample is equilibrated against a large reservoir of mother liquor. Volatile substances can then diffuse between drop and reservoir, reaching an equilibrium in which the protein will crystallize. The absence of crystals and a clear drop indicates that the equilibration is still ongoing or the sample concentration is too low. When the drop shows precipitate but no crystals, the sample concentration might be too high. The protein crystals obtained are mostly fragile and/or they contain ordered molecules but also disordered solvent in between. The crystal volume occupied by solvent molecules is at about 40-60 % depending on the crystal¹⁰³. With post-crystallization treatments the volume of solvents can be reduced, and the crystal lattice becomes more ordered or the packing is more dense. This can even change the crystallographic space group. These rearrangements reinforce and form new crystal contacts, resulting in better diffracting crystals. The most effective post-crystallization protocol must be evaluated for

every crystal condition. Mostly it encompasses an increase or introduction of precipitant and/or the addition of small molecules which stabilize the crystal internally. Crystal dehydration can lead to remarkable improvements in crystal diffraction¹⁰⁴.

Since collection of X-ray data is carried out using a high intensity beam, the energy can cause severe heating and radiation damage on the crystal. To increase the lifetime of crystals in the X-ray beam it is an advantage to cool the crystals to very low temperatures (100 K/ -173 °C), the crystals must be protected from ice formation by using cryo-protectants. These cryo-protectants include Glycerol, MPD, low molecular weight PEGs and oils. The crystals are transferred to the cryo-protectant for varying time spans between a few seconds and hours. The crystals are then frozen in liquid nitrogen (LN₂) prior to X-ray measurements. An overall workflow of X-ray crystallography is presented in Figure 1.10.

1.4.2 Single Particle Electron Cryomicroscopy

Electron microscopy is the youngest among all other methods to determine three dimensional structures of protein complexes. In 1872, Ernst Abbe formulated his wave theory of microscopic imaging and about 60 years later the first electron microscope was built by Ernst Ruska and Max Knoll¹⁰⁵. Historically, electron microscopes were developed to overcome the limited resolution in light microscopes, imposed by the wavelength of visible light. Due to the small wavelength of electrons electron microscopes are capable of imaging at a higher resolution.

Using electron microscopy, a broad specimen range from the atomic to tissue scale objects can be imaged, providing snapshots of biological samples and cells close to their native states. For isolated macromolecular complexes the method of choice is the single particle electron cryomicroscopy approach using a transmission electron microscope (TEM). The TEM has a very similar setup to a light microscope, whereby the image is formed by transmitting electrons and not light. Those electrons interacting with the sample contribute to a phase contrast image, the electron micrograph. Phase contrast imaging is the highest resolution imaging technique ever developed, and can allow for resolutions of less than 1 Å.

Macromolecular machines are important in all living cells and with improving imaging and image processing methods, electron microscopy is now a standard technique to study macromolecular assemblies. The method became popular when it was possible to structurally study macromolecular complexes which are resistant to crystallization, albeit at lower resolution. Over the years, technological advances in sample preparation, instrumentation and computational analysis made electron microscopy a benchmark for structural studies.

Structural investigation of macromolecular complexes starts with a specialized sample preparation method. The purified protein sample is usually applied to an EM grid covered with a thin holey carbon film and blotted by a filter paper to remove excess solution to form a thin liquid layer. The sample is then rapidly vitrified in liquid ethane¹⁰⁶ to bring all particles to a solid state and to prevent dehydration within the vacuum of an electron microscope. Freezing also reduces the effects of electron beam damage¹⁰⁷. Next, the images, called electron micrographs, are collected to capture 2-dimensional projections of single particles in spacial orientations. Due to low dose exposure to reduce beam damage, the 2D micrographs have a poor image contrast. To reduce the noise, a high number of individual particles in the same orientation are averaged using software that aligns and merges the data. An initial 3D volume is constructed from many averaged images and the map is then iteratively refined and validated to become the final 3D map. Subsequently, the model is built and the quality of the map is then evaluated.

Recent technical advances in single particle cryo-EM allow structures of macromolecular machines to be determined in the resolution range between 2.5 to 5 Å. For example, ribosomes from human pathogens¹⁰⁸ or ribosome-protein complexes provide insight to their functions. Simultaneously, technical improvements in cryo-EM led to structures of smaller complexes with molecular masses smaller than 200 kilodaltons (kDa) to be determined¹⁰⁹. An idealized single particle electron cryomicroscopy workflow is presented in Figure 1.10.

1.4.3 Advantages and Disadvantages

In the last years, the major advances achieved in all aspects of structural biology are numerous. Sample preparation, crystallization, access to synchrotron facilities, high-end microscopes and high-speed computing enable multiple solutions to gain structural information of many microscopic objects. Working with X-ray crystallography and single particle electron cryomicroscopy means working with two diffraction-based techniques that bring along their own benefits and limitations.

A decisive factor when comparing these two techniques is the sample amount. For many protein complexes scientists struggle to purify large quantities, because the sample is labile or the purification protocol is not mature. For EM, only relatively low amounts of sample are needed, whereas crystallization often requires amounts in the milligram quantity range.

Both X-ray and electron beams cause radiation damage to biological samples. In X-ray crystallography some crystals tolerate high total doses because of their size and/or packing within the crystal. In EM, the total electron dosage to image the single particles has to be set to a minimum to preserve the structural information. As a consequence, low

dose imaging results in a poor signal-to-noise ratio making it is difficult to obtain good quality data.

X-ray diffraction reveals its major limitation when studying macromolecular complexes: crystallization of dynamic complexes is challenging and phasing represents the common bottleneck in crystallography. Even with outstanding samples, a successful analysis by X-ray crystallography is limited by the production of crystals and finally by the crystal quality which is still a trial and error approach. Nevertheless, in the last ten years an unprecedented increase in the number of new crystal structures in the Protein Database (PDB) is apparent.

Electron cryomicroscopy is suitable for large (>100 kDa) macromolecular complexes. Cryo-EM often struggles with problems in image analysis, which is mostly dependent on the sample quality. However, electron cryomicroscopy represents a powerful tool to study the structure and dynamics of macromolecular complexes at intermediate resolutions between 10 and 30 Å, while resolutions around 3 Å can also be achieved. The resolution limit around 3 Å was reached with macromolecular machines like polymerases, ribosomes and viruses from various organisms.

Moreover, hybrid structural approaches are also common. Cryo-EM and X-ray crystallography are complementary techniques; often atomic models from crystallographic studies are combined with electron microscopic data at medium resolution.

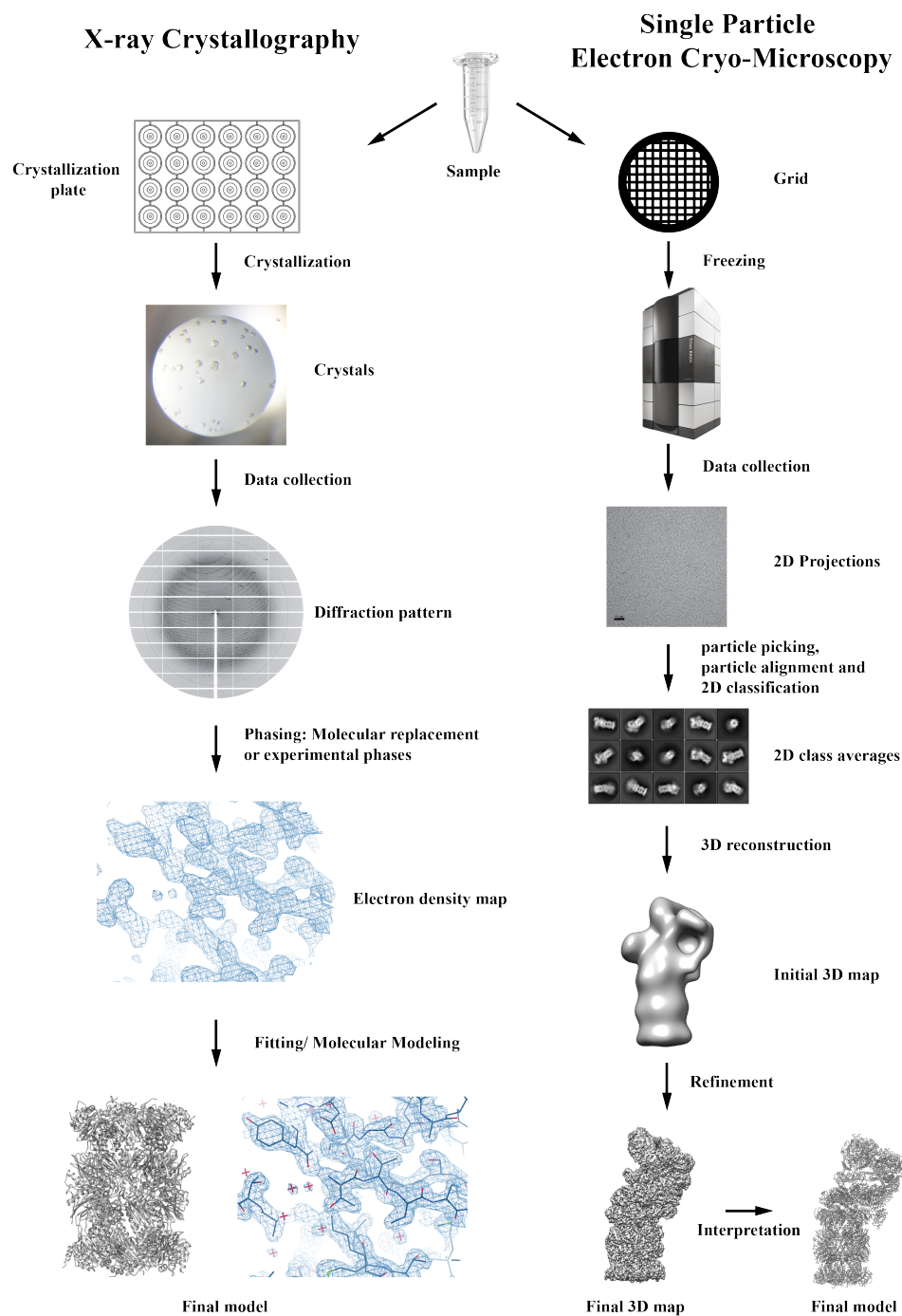


Figure 1.10: The overall X-ray crystallography and single particle cryo-EM workflow, from protein sample to 3D model. Schematic figure showing the workflow for macromolecular structure determination by X-ray crystallography and Cryo-EM. (1) X-ray crystallography: Diffraction images are obtained from protein crystals. These images encode the structural information. With the help of Fourier transformations, the information is translated into the molecular real space. Since the phases are not directly accessible so-called phasing approaches have to be performed. With further experimental data or by molecular replacement calculations these phases are obtained. Once initial phases are obtained, electron density maps are calculated. Molecular model building and structural refinement form the final steps of x-ray crystallographic model building. (2) Cryo-EM: A single-particle project starts with specimen preparation and the collection of EM images. The single particles are isolated and 2D analysis is performed. Next, an initial 3D map is calculated and iteratively refined. The final map is used to build a 3D model of the macromolecule.

1.5 Objectives

The aim of this thesis is to structurally characterize the inhibition of the human proteasome. During the course of this thesis, special attention was paid to the development of new methods and improvement of known methods to find ways for screening and characterizing the inhibition of the human 20S and 26S proteasome.

To elucidate structures of the human 20S proteasome, a reproducible, large-scale method to purify proteasomes from HeLa cytoplasmic extract was needed. Hence, a great effort was spent on the development of a gentle, chromatography-free purification strategy for human proteasomes. A robust pipeline for the production and crystallization of human 20S proteasomes could be established. The crystallization procedure reproducibly yielded 20S proteasome crystals in high abundance and allowed the analysis of native human 20S proteasome and in complex with cancer therapeutics in greater detail.

In the second part of this thesis, the structural implications of 20S core particle inhibition on the human 26S holoenzyme were studied. The novel purification strategy was transferred to human 26S proteasomes, yielding high amounts of 26S proteasome complexes. Structures of human 26S proteasomes with and without inhibitors were analyzed by single particle electron cryomicroscopy and the structural differences were investigated. The visualization of changes in the structure of the human 26S proteasome upon drug binding then allowed to formulate a hypothesis for future proteasome inhibitor design.

Chapter 2

Materials and Methods

2.1 Materials

2.1.1 Software

Table 2.1: Software used in this thesis.

Software	Source
Amira 4.1	https://www.fei.com/software ¹¹⁰
Adobe Creative Suite 5	http://www.adobe.com/de/creativecloud.html
CCP4	http://www.ccp4.ac.uk
Cow software suite	Group of Prof. Dr. Stark, Göttingen
COOT	https://www2.mrc-lmb.cam.ac.uk/personal/pemsley/coot ¹¹¹
Gautomatch	http://www.mrc-lmb.cam.ac.uk/kzhang
Gctf	http://www.mrc-lmb.cam.ac.uk/kzhang ¹¹²
Imagic	https://www.imagescience.de/imagick_em.html ¹¹³
JLigand	http://www.ytbl.york.ac.uk/mxstat/JLigand ¹¹⁴
KaleidaGraph 4.03	http://www.synergy.com/wordpress_650164087
Orca 3.0.3	https://orcaforum.cec.mpg.de/
OriginPro 9.1	http://www.originlab.de/Origin
Phenix	https://www.phenix-online.org
Python 2.7	https://www.python.org
PyMOL	https://www.pymol.org
RELION 1.2	http://www2.mrc-lmb.cam.ac.uk/relion ¹¹⁵
ResMap	http://resmap.sourceforge.net
Simple PRIME	http://simplecryoem.com ¹¹⁶
UCSF Chimera	http://www.cgl.ucsf.edu/chimera ¹¹⁷

2.1.2 Special Equipment

Table 2.2: Machines and special equipment used in this thesis.

Machine/Equipment	Manufacturer
ActiLoops	Molecular dimensions
Äkta Prime	GE Healthcare
Balances	Sartorius
Centrifuge LYNX 6000	Thermo Scientific
Copper EM grids	Plano
Crychem M Plate, 24-well	Hampton Research
Crystal Clear Sealing Tape	Jena Bioscience
Crystalgen Plate 24-well, pregreased	Jena Bioscience
Fiberlite rotor F14, F21, F35L	Thermo Scientific
FluoroMax-4 fluorescence spectrophotometer	Horiba Scientific
Gradient Master ip	Biocomp
Incubator Eco-Line E100	RUMED
Incubator Multitron Pro Shaker	Infors HT
Leica EM GP	Leica
LithoLoops	Molecular dimensions
Micro-Ultracentrifuge MX 150+	Sorvall
Orbital Shaker RS0S20	Phoenix Instrument
Photometer Lambda Bio X	Perkin Elmer
Plate Sealer ALPS 3000	Thermo Scientific
Pipetting Robot Microlab Star LET	Hamilton
Quantifoil grid R3.5/1 Cu 200 mesh	Quantifoil Micro Tools GmBH
Rotor TH660	Sorvall
Rotor S140AT	Thermo Scientific
Rotor SW40	Beckmann Coulter
Siliconized Glass Cover Slides	Hampton Research
Stereo microscopes M125	Leica
TEM CM200 FEG	Philips
TEM Titan Krios	FEI
Ultracentrifuge WX Ultra 80, 90	Sorvall
Vitrobot	FEI
Zebra Micro Desalt Spin Columns	Thermo Scientific

2.1.3 Chemicals

Table 2.3: Chemicals, Substrates, Enzymes and Antibodies used in this thesis.

Chemicals	Supplier
2-methyl-2,4-pentanediol (MPD)	Sigma-Aldrich
1,4-Dithiothreitol (DTT)	Roth
Aspartate	Sigma-Aldrich
β -Glycerophosphate disodium salt hydrate	Sigma-Aldrich
Benzamidine Hydrochloride hydrate	Sigma-Aldrich
Bis[sulfosuccinimidyl] suberate (BS3)	Thermo Scientific
Bis(2-hydroxyethyl)amino-tris(hydroxymethyl)methan	Sigma-Aldrich
Bovine serum albumin (BSA)	Sigma-Aldrich
Bradford Assay reagent	BioRad
Coomassie Brilliant Blue R-250	BioRad
Dimethylsulphoxide (DMSO)	AppliChem
Dinatriumhydrogen phosphate (Na_2HPO_4)	Merck
Dipotassium phosphate (K_2HPO_4)	Merck
Ethanol	Merck
Ethylenediaminetetraacetic acid (EDTA)	Merck
Glucose	Merck
Glutaraldehyde	Science Services
Glycerol	Merck
Iodoacetamide	Sigma-Aldrich
Isopropanol	Merck
Lauryl Maltose Neopentyl Glycol	Anatrace
Magnesium chloride	Merck
Magnesium acetate	Merck
N-ethylmaleimide	Sigma-Aldrich
Octyl Glucose Neopentyl Glycol	Anatrace
Phosphoenolpyruvic Acid Tris(cyclohexylammonium)	
Salt Hydrate	TCI
Polyethylene glycol (PEG) 400	Sigma-Aldrich
Polyethylene glycol (PEG) 3350	Sigma-Aldrich
Potassium chloride	Merck
Potassiumdihydrogen phosphate (KH_2PO_4)	Merck
Protamin sulphate	Sigma-Aldrich
Protease inhibitor tablet , EDTA free	Roche
Protein Marker	BioRad

Pyruvate kinase	Roche
Sucrose	Merck
Sodium chloride	Merck
SDS-PAGE running buffer	Roth
Sulfo-MBS	Thermo Scientific
<hr/>	
Substrates, enzymes, antibodies	Supplier
Bortezomib	Selleckchem
Delanzomib	Selleckchem
Dihydroeponepmycin	APExBIO
Epoxomicin	APExBIO
Ixazomib	Selleckchem
Oprozomib	Selleckchem
Suc-LLVY-AMC	Bachem
Ubiquitin Antibody	Santa Cruz Biotechnology
Z-LLY-Ketoaldehyde	Bachem

2.1.4 Buffers

Table 2.4: Buffers for protein purification, crystallization, crystal stabilization/dehydration and enzymatic assay. Composition of all buffers used for the experiments listed in this thesis.

Purpose	Composition
Purification	0.05 M BisTris pH 6.5, 0.05 M KCl, 0.01 M MgCl ₂ , 0.01 M β -Glycerophosphate
Crystallization	0.1 M BisTris pH 6.5, 0.2 M MgCl ₂ , 10 % (w/v) PEG3350
Crystal stabilization	0.1 M BisTris pH 6.5, 0.2 M MgCl ₂ , 20 % (w/v) PEG3350
Crystal dehydration	0.1 M BisTris pH 6.5, 0.2 M MgCl ₂ , 25 % (w/v) PEG3350, 20 % (v/v) MPD
Enzyme activity	0.05 M BisTris pH 6.75, 1 mM EDTA, 0.01 % (w/v) SDS

2.2 Methods

2.2.1 Protein Purification

2.2.1.1 Purification of 20S Proteasomes from HeLa cells

S30 HeLa cytoplasmic extract was prepared by hypotonic lysis according to Dignam et al.¹¹⁸, with some minor modifications: after hypotonic lysis and centrifugation to collect nuclei, the supernatant (the crude cytoplasmic extract) was centrifuged at 30.000 x g for 30 minutes at 4 °C and flash frozen in 40 ml aliquots in liquid nitrogen and stored at -80 °C until further use.

The S30 HeLa cytoplasmic extract was thawed in a water bath at 37 °C, supplemented with purification buffer to 1x concentration from a 10x stock, followed by the addition of sucrose powder to 20 % (w/v), Octyl Glucose Neopentyl Glycol (OGNG; from a 10 % (w/v) stock solution in water) to 0.1 % (w/v), Iodoacetamide to 10 mM, N-Ethylmaleimide to 10 mM and Benzamidinium Chloride to 10 mM. The extract was incubated at room temperature on a magnetic stirrer for 30 minutes, followed by incubation at 30 °C with shaking at 140 rpm for 1 hour. The treated extract was centrifuged at 100.000 x g for 2 hours at 4 °C. After centrifugation, the supernatant was filtered through 3 layers each of cheese cloth and miracloth to obtain a S100 HeLa cytoplasmic extract. The clarified extract is subjected to differential precipitation with Poly Ethylene Glycol400 (PEG; number signifies the mean molecular weight of the PEG polymer). PEG400 is added at a concentration of 20 % (v/v) to the S100 HeLa cytoplasmic extract under stirring at 4 °C and incubated for 20 minutes. Precipitated proteins are removed by centrifugation at 30.000 x g for 30 minutes at 4 °C. The supernatant is then precipitated by raising the concentration of PEG400 to 30 % (v/v) as described above. The precipitate of this step, which contains human 20S proteasomes, is recovered by centrifugation at 30.000 x g for 30 minutes at 4 °C and resuspended in purification buffer containing 2 % (w/v) sucrose, 10 mM DTT and 0.01 % (w/v) Lauryl Maltose Neopentyl Glycol (LMNG) in an orbital shaker at 18 °C.

The resuspended material is loaded on 10-30 % (w/v) sucrose gradients in purification buffer containing 5 mM DTT, which are centrifuged at 270.000 x g for 16 hours at 4 °C. Gradients were harvested in 400 µl fractions using Äkta Prime. SDS-PAGE¹¹⁹ was utilized to identify fractions containing 20S proteasomes. Selected fractions were pooled and precipitated by the addition of 40 % (v/v) PEG400. After centrifugation (30.000 x g, 20 minutes), the supernatant was removed and the precipitate was resuspended in Purification buffer containing 5 % (w/v) sucrose, 10 mM DTT and 0.01 % (w/v) LMNG. The resuspended material is loaded on linear 10-40 % (w/v) sucrose gradients in Purification

buffer containing 5 mM DTT, which are centrifuged at 284.000 x g for 20 hours at 4 °C. Fractions containing 20S proteasomes are yet again identified by SDS-PAGE, precipitated and concentrated by the addition of 40 % PEG400 and resuspended in Purification buffer containing 5 % (w/v) sucrose, 5 mM DTT and 0.01 % LMNG, yielding the finally purified protein preparation at 13 mg/ml.

Protein concentrations were determined by the Bradford assay (BioRad, Munich, Germany) using BSA as a standard. This procedure reproducibly yields 20 mg purified human 20S proteasomes, starting from 300 ml S100 HeLa cytoplasmic extract at a concentration of 10 mg/ml. The entire purification procedure is concluded within 48 hours yielding crystallization grade protein.

The purification description is according to Schrader et al., 2016¹²⁰.

2.2.1.2 Purification of 26/30S Proteasomes from HeLa Cells

Purification of human 26/30S proteasomes was performed according to the recently developed human 20S proteasome protocol, as described above. S30 HeLa cytoplasmic extract is prepared by hypotonic lysis¹¹⁸, centrifuged at 30.000 x g for 30 minutes at 4 °C, flash frozen in liquid nitrogen and stored at -80 °C.

The S30 extract was thawed in a water bath at 37 °C, supplemented with purification buffer to 1x from a 10x stock, sucrose powder to 20 % (w/v), Octyl Glucose Neopentyl Glycol (OGNG; from a 10 % (w/v) stock solution in water) to 0.1 % (w/v), Iodoacetamide to 10 mM, N-Ethylmaleimide to 10 mM, Benzamidinium Chloride to 10 mM and ATP to 7.5 mM. The extract was incubated at room temperature on a magnetic stirrer for 30 minutes, followed by an addition of Dithiothreitol (DTT) powder to 50 mM and a second incubation at room temperature for 30 minutes. The S100 extract was prepared by centrifugation at 100.000 x g for 2 hours at 4 °C and the supernatant was filtered through 3 layers each of cheese cloth and miracloth.

The S100 extract was processed by two subsequent rounds of precipitation with PEG400. First, PEG400 was added to a concentration of 23 % (v/v) to the S100 extract at 18 °C on a magnetic stirrer and incubated for 30 minutes. Second, the supernatant was precipitated by raising the concentration of PEG400 to 30 % (v/v) as described before. The precipitate contains the human 26S/30S proteasomes and was resuspended with purification buffer supplemented with 7.5 mM ATP, 5 mM DTT and 0.01 % (w/v) Lauryl Maltose Neopentyl Glycol (LMNG) in an orbital shaker at 18 °C. The resuspended material was incubated with an ATP regeneration system (10 mM Sodium Creatine phosphate, 5 µg/mL Creatine kinase) at 30 °C for 30 minutes.

The sample was loaded on 20 % / 50 % 2-step sucrose cushions in purification buffer containing 7.5 mM ATP and 5 mM DTT. The cushions were centrifuged at 260.000 x g for 14 hours at 4 °C, harvested in 500 µl fractions with Äkta Prime™ (GE Healthcare ,

Munich, Germany) and analyzed by SDS-PAGE to identify fractions containing 26S and 30S proteasomes. Fractions were pooled and precipitated by the addition of 40 % (v/v) PEG400 for 30 minutes and after centrifugation (30.000 x g, 30 minutes) the precipitate was resuspended in purification buffer containing 5 % sucrose, 7.5 mM ATP, 5 mM DTT and 0.01 % (w/v) LMNG. The proteasomes were treated with Oprozomib at a concentration of 0.5 mM at 25 °C for 30 minutes. Proteasomes were loaded on linear 10-40 % (w/v) sucrose gradients in purification buffer containing 7.5 mM ATP, 5 mM DTT, which were centrifuged at 220.000 x g for 16 hours at 4 °C. 400 µl fractions were analyzed by SDS-PAGE, selected proteasome fractions were precipitated by the addition of 40 % (v/v) PEG400 and resuspended in purification buffer containing 7.5 % (w/v) sucrose, 7.5 mM ATP, 5 mM DTT and 0.01 % (w/v) LMNG.

As a final step, proteasomes were fractionated on linear 10-45 % (w/v) sucrose gradients in purification buffer containing 7.5 mM ATP, 5 mM DTT, which were centrifuged at 260.000 x g for 16 hours at 4 °C. Fractions containing 26/30S proteasomes were yet again identified by SDS-PAGE, precipitated by the addition of 40 % (v/v) PEG400 and resuspended in 2x purification buffer containing 15 % (w/v) sucrose, 15 mM ATP, 10 mM DTT and 0.02 % (w/v) LMNG yielding the final purified protein preparation at 30 mg/ml. Protein concentrations were determined by the Bradford assay (BioRad, Munich, Germany) using BSA as a standard.

This purification procedure reproducibly yields 45 mg purified human 26/30S proteasomes, starting from 800 ml S100 HeLa cytoplasmic extract at a concentration of 10 mg/ml.

2.2.2 Enzyme Kinetics

To determine the chymotryptic-like activity of the $\beta 5$ catalytic active site of the human 20S proteasome, kinetic measurements were performed using a FluoroMax-4 fluorescence spectrophotometer. Succinyl-Leucine-Leucine-Valine-Tyrosine-7-amido-4-methylcoumarin (Suc-LLVY-AMC) was utilized as substrate. Enzyme kinetics were determined by measuring the fluorescence emission of the hydrolyzed substrate at 460 nm ($\lambda_{\text{ex}} = 380$ nm) at a constant temperature of 37 °C.

The Suc-LLVY-AMC conversion was characterized using 50 nM human 20S proteasomes. The proteasomes were pre-incubated in reaction buffer at 37 °C for 3 minutes. The reaction was started by adding the substrate and the fluorescence signal was measured continuously.

When analyzing the first-order rate constant of inhibition, the reaction mixture containing the reaction buffer, 150 µM Substrate and the respective inhibitor was pre-incubated. The following inhibitor concentration were used: 50 µM Oprozomib, 50 µM Dihydroepone-mycin, 15 µM Z-LLY-Ketoaldehyde. The reaction was started by the addition of human

20S proteasomes at a final concentration of 50 nM. Suc-LLVY-AMC and the inhibitors were dissolved in DMSO and stored at -80 °C until usage. Data analysis was carried out with OriginPro 9.1 (Origin Lab) and KaleidaGraph 4.03 (Synergy Software). To analyze the chymotryptic-like catalytic activity and catalytic activation of the 20S proteasome the following equation was used:

$$F(t) = F_0 + \Delta F_{ss} \cdot t - \frac{(\Delta F_{ss} - \Delta F_0)}{k_{act}} \cdot (1 - \exp(-k_{act} \cdot t)). \quad (2.1)$$

where F_0 denotes the fluorescence at time $t = 0$ and ΔF_{ss} the increase in fluorescence (activity) in *steady state* after activation. ΔF_0 denotes the increase in fluorescence (activity) at time $t = 0$ prior to activation. k_{act} denotes the first-order activation rate constant. The first-order inactivation rate constants were determined by using the equation with two exponential terms (Z-LLY-Ketoaldehyde) or two exponential terms and a linear term for the epoxyketone inhibitors Oprozomib and Dihydroeponemycin. The first term makes up the catalytic activation, whereas the second exponential term accounts for the catalytic inactivation by inhibition. The linear term signifies the residual activity of the proteasome after inactivation by epoxyketone inhibitors.

Data analysis was performed by Prof. Dr. Kai Tittmann, University Göttingen. The method description is according to Schrader et al., 2016¹²⁰.

2.2.3 Electronic Structure Calculations

Cluster calculations were carried out on selected model systems, considering the Dihydroeponemycin, Oprozomib and Z-LLY-Ketoaldehyde inhibitors. The starting structures were based on the crystallographic data. All stationary points and constrained optimizations were carried out at the B3LYP-D3(BJ)/def2-SVP level of theory^{121,122,123,124}, which include dispersion corrections as suggested by Grimme, with a Becke-Johnson type damping¹²⁵. The nature of the stationary points was confirmed by frequency calculations. The reaction energy profiles are provided at the level of theory used for the optimizations (B3LYP-D3/def2-SVP).

Free-energy corrections were computed from frequency analysis under the rigid-rotor harmonic approximation of the latter structures. The electronic energy was determined at the B3LYP-D3/def2-TZVP level of theory, under the COSMO continuum solvation model¹²⁶. Diethyl ether was employed as the solvent ($\epsilon=4.3$), which is commonly chosen to model protein-like environments¹²⁷. All free-energy values reported correspond to the sum of the latter electronic energies and the thermodynamic corrections computed with the smaller def2-SVP basis set. All calculations were carried out with the Orca 3.0.3 program pack-

age¹²⁸.

Cluster quantum chemical calculations were performed by Prof. Dr. Ricardo Mata, University Göttingen. The method description is according to Schrader et al., 2016¹²⁰.

2.2.4 Crystallization Methods

2.2.4.1 Preparation of Protein Crystals

The basis for all protein crystallization experiments is formed by the phenomenon that a protein will stay in solution only up to a certain concentration, depending on its solubility limit. Crystallization requires bringing the macromolecule to a supersaturation state. Introducing the sample to a precipitation agent can promote the nucleation of protein crystals in the solution.

The two main techniques to obtain crystals are vapor diffusion and batch crystallization. Vapor diffusion is carried out in a hanging or sitting drop set up: A drop containing a mixture of protein and precipitant is sealed in an environment of pure precipitant (Figure 2.1, A). Over time, dehydration of the protein drop takes place until an equilibrium between drop and precipitant is formed. During the vapor diffusion method, a protein solution will start to concentrate from an undersaturated state to a supersaturated state. If crystals are formed the concentration of the free protein in the drop will decrease and crystals grow until the concentration of protein drops below to, or below the solubility line (Figure 2.1, B). The vapor diffusion techniques are easily adjustable by increase or decrease of the starting protein concentration or by the ratio of protein to precipitant or even by ratio of protein-precipitant mixture to the precipitant reservoir.

In the batch approach, the protein is mixed with a defined amount of the precipitant. To prevent the drop from drying out, the procedure is performed under a paraffin/mineral oil film, as shown in Figure 2.1, A. If the concentration of the precipitant is chosen in such a way that the solution is in the metastable zone, a successful crystallization might occur (Figure 2.1, B).

For the human 20S proteasome, crystallization attempts were carried out by the vapor diffusion method. With a vast number of possible crystallization conditions it took time until different precipitant solutions and effects of pH, temperature and additives were analyzed and a final crystallization condition was found. The new crystal form of the human 20S proteasome was obtained using the precipitant PEG3350 in combination with the buffer substance BisTris at pH 6.5 and the salt additive MgCl₂ (Crystallization buffer).

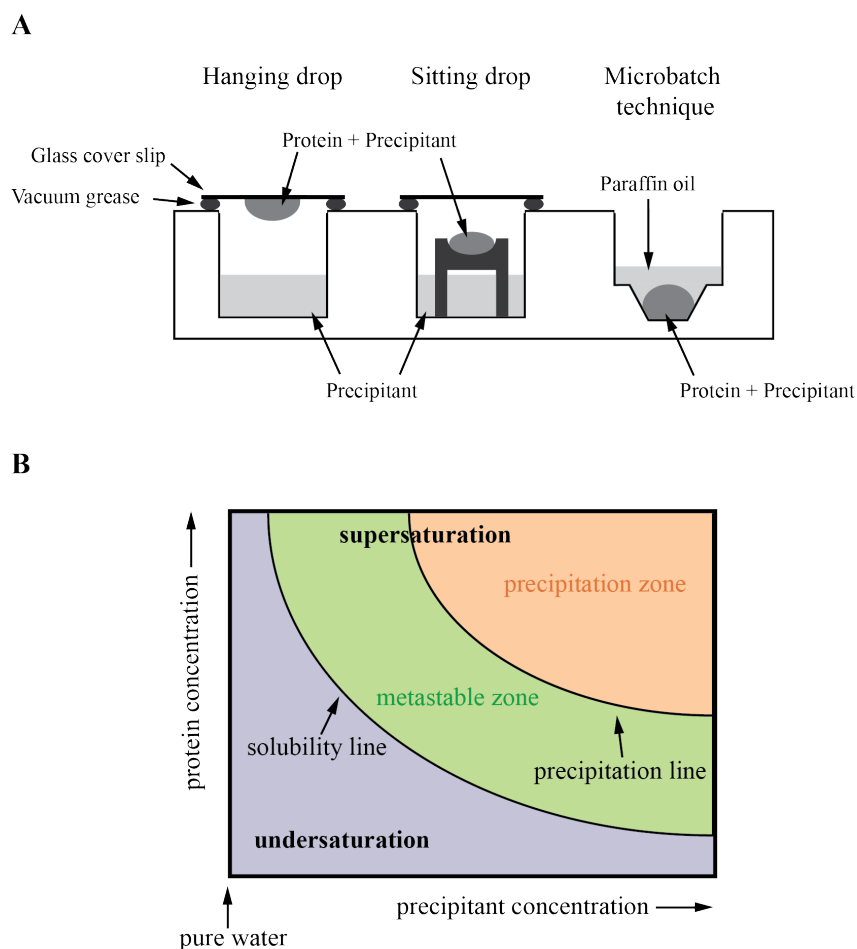


Figure 2.1: Crystallization techniques and the crystallization phase diagram. (A) Schematic representation of vapor diffusion techniques hanging and sitting drop and batch crystallization technique. (B) Schematic representation of a two-dimensional phase diagram, illustrating the change of protein concentration against precipitating agent concentration. Two areas are separated by the solubility line: the undersaturated and the supersaturated state of a proteins solution. The supersaturated area comprises the metastable and the precipitation zones, whereby crystals will eventually appear in the metastable phase and no crystals are formed in the precipitation zone. Modified from Bernhard Rupp¹²⁹.

2.2.4.2 Postcrystallization Treatment

To improve the diffraction quality of macromolecular complexes it is almost always required to perform a postcrystallization treatment after crystals are obtained. Initial crystals are often of poor quality and unsuitable for X-ray studies. Postcrystallization is a method that provides the possibility to increase the diffraction quality of crystals. For the human 20S proteasomes one crucial step in crystal preparation is the dehydration, resulting in a controlled reduction of solvent molecules in the crystal and decrease of volume of the crystal by altering the crystal packing. These rearrangements promote new crystal contacts and thereby result in better diffracting crystals. Dehydration is performed by an increase or an introduction of precipitant: here PEG3350 and MPD.

2.2.5 X-ray Analysis Methods

2.2.5.1 Crystal Mounting and Diffraction Data Collection

After post crystallization treatments the human 20S proteasome crystals are ready for harvest. Crystals are harvested in Litholoops mounted on a standard 18 mm stainless steel pin and plunged in liquid nitrogen or directly transferred to a nitrogen gas stream at 100 K. X-ray diffraction data was collected under cryogenic conditions at 100 K. Initial crystal screening and data collections were performed at beamline ID23-I, ESRF, Grenoble, France using the PILATUS 6M detector. The high-resolution diffraction datasets were collected at the P14 beamline of the Petra III storage ring, EMBL, Hamburg, using the MD3 diffractometer with the spindle axis mounted in a vertical and downward configuration and the PILATUS 6M detector.

At the P14 beamline, a smooth "top-hat" X-ray beam profile with a total photon flux of up to 2×10^{13} ph/ sec was created by the installation of focusing Compound Refractive Lenses 20.6 m upstream of the sample position and slits 0.3 m upstream. To get beam-sizes matching the crystal sizes the slit opening was adjusted ($150 \times 200 \mu\text{m}^2$ in linear dimensions). Exposing the whole crystal provided by far the best resulting datasets. Standard setups with small X-ray beams or helical data collection only resulted in 2.3 Å maximal resolution.

Crystals were exposed 40 ms per image with a gamma-slicing of 0.05 - 0.1 in a total rotation range of 180° - 360° at 50% attenuation. The collected datasets were rapidly scaled and integrated with the XDS program package.

2.2.5.2 Structure Determination

For model building the initial phases were determined by molecular replacement using the murine 20S structure (PDB ID: 3UNE). Model building and optimization was performed using COOT¹¹¹. Subsequent refinement was performed using the program REFMAC5 in the CCP4 package¹³⁰. Final graphic representations of details in the crystal structure were completed using the programs PYMOL and COOT. For modeling the bound inhibitors, complete stereo-chemical descriptions of double- or single-covalent link attachments were created using the program JLigand¹¹⁴ and applied in real-space fitting with COOT followed by a refinement with REFMAC5.

2.2.5.3 Identification of Ions

The identification of many ions in the native 20S structure was validated by anomalous difference Fourier maps. For ligands in question, soaking experiments with anomalous

scatterers were performed: Cl⁻ ions were identified by their anomalous Fourier differences at 6.5 keV and by exchange against Br⁻ ions and measurements at the bromide K- absorption edge (13.47 keV). Mg²⁺ ions were identified by exchange through soaking crystals with Mn²⁺ ions and measurements at the manganese absorption edge (6.5 keV). K⁺ ions were identified by their residual anomalous scattering at 6.5 keV, non-exchangeability by either Br⁻ or Mn²⁺ and by measuring the coordination distances to neighboring residues within the structure.

2.2.6 Sample Preparation for Electron Microscopy

2.2.6.1 GraFix

The purified human 26S proteasomes were prepared for EM analysis by a fixation protocol: First, the sample was fixated in batch, using 2 mM of the crosslinking agent BS3 for 30 minutes at 4 °C. The BS3-fixed protein sample was then loaded onto 10-30 % (w/v) GraFix gradient in which the complexes are centrifuged into an increasing concentration of the fixation reagent glutaraldehyde. The gradients contained 0-0.05 % (w/v) glutaraldehyde and were centrifuged for 16 hours at 114000 x g. The human 26/30S proteasomes sediment to 2/3 of the gradient and the exact fraction is determined by fractionation and dotblot analysis. Dotblot is performed by pipetting 2 µl of each sample fraction onto a nitrocellulose membrane and subsequent staining with amido black solution. After fractionation, the sample is immediately quenched by adding 20 mM of sodium aspartate (pH 6.5).

2.2.6.2 Negative Staining

The fractions containing the 26/30S proteasomes were analyzed by negative stain electron microscopy. A 2 % (w/v) uranyl formate solution was prepared freshly in double distilled water. In-house prepared carbon film was floated on the protein solution for up to 1 minute, depending on the protein concentration. The foil with the attached protein complexes was picked up by a holey carrier carbon film on a copper grid. Excess liquid was removed by gentle blotting of the grid with a filter paper. The grid containing foil and particles was then transferred onto the staining solution for 1 minute. The excess staining solution was blotted with a filter paper and the grid was allowed to air dry at room temperature for at least 10 minutes.

2.2.6.3 Vitrification

After determination of the sample's quality by negative stain electron microscopy the sample was prepared for subsequent vitrification for cryo-EM analysis. For a successful cryo grid preparation the sucrose had to be removed from the protein sample. Almost all sucrose is removed by buffer exchange on Zeba Spin desalting columns and the particles were absorbed by continuous foil, as described before. The foil was picked up by a quantifoil grid containing a thick carbon film. Thereafter, the grid is loaded into the Vitrobot or Leica EM GP apparatus. 4 μl of water is loaded to one side of the grid before blotting at 4 °C at 100-75 % humidity. The grid was then plunge-frozen into liquid ethane and the thin water film with the particles on the grid was vitrified. Grids were stored in liquid nitrogen until usage.

2.2.7 Imaging of Electron Microscopic Data

Negative stain electron microscopic analysis was performed on a CM200 FEG microscope. Images were taken at 1 μm defocus on a twice binned CCD camera at a magnification of 88000 x. The corresponding pixel size is 2.5 \AA /pixel. High-resolution cryogenic electron microscopy was performed on a Titan Krios TEM microscope equipped with a C_s -corrector. 17 image frames were recorded on a direct electron detector (Falcon2) with a dosage of 50 electrons per \AA^2 with a pixel size of 1.27 \AA .

2.2.8 Image Processing

Image processing of the human 26S proteasome was performed by Dr. David Haselbach, Structural Dynamics Department at the Max Planck Institute for Biophysical Chemistry, Göttingen.

2.2.8.1 Micrograph Analysis and Particle Picking

Individual image frames were aligned and weighted according to electron dose to reduce the effects of drift and charging using the software unblur¹³¹. The Contrast Transfer Function (CTF) was determined on averaged micrographs with Gctf¹¹². Particles were selected with the software Gautomatch¹³² and individual particle coordinates were refined by alignment against a projected model of the 26S proteasome. Particles were cropped in a window 1.5 times in diameter.

2.2.8.2 2D Processing

For 2D analysis, particles were down-sampled to a pixel size of 4 to 8 Å/pixel as well as filtered and normalized. Several image sorting steps to remove contaminations, blurred images or broken particles were performed: First, power spectra for each particle were calculated and classified using a hierarchical cluster scheme. The resulting class averages were visually inspected for the Thon ring quality. Strongly charged and/or blurred classes were discarded. Second, iterative rounds of multi-reference alignment and 2D classification were performed. Particles sampled into classes which do not show intact proteasome particles were discarded.

2.2.8.3 Initial Model Building

After particle sorting, the best class averages were chosen and an initial 3D model was generated with the program simple PRIME¹¹⁶. This independent approach produces 3D models based on an iterative projection-matching approach without the need of an initial model.

2.2.8.4 Conformational Sorting

The resulting 3D model was used as the initial reference for 3D classification, using the program RELION¹¹⁵. Here, all particles were classified according to the two main conformational states (non-rotated and rotated). The flexible protein Rpn1 was masked out because it interferes with the alignment.

2.2.8.5 Refinement and Resolution Determination

The particles belonging to the non-rotated state were refined using the "auto-refine" routine in RELION. Further hierarchical sorting was performed in RELION to sort particles regarding to various regulatory particle conformations: A series of 3D classification steps without alignment with decreasing mask size was performed. After 4 refinement steps, 98000 particles contributed to the final 26S proteasome model (details in Results section). A local resolution map was estimated in ResMap¹³³, calculating local Fourier Shell Correlation (FSC) values in a sphere with a diameter of 13 voxels, scanning the entire 3D model.

2.2.8.6 Model Building

For the 20S particle, the crystal structure of the Oprozomib-inhibited human 20S proteasome was used as initial atomic coordinate model (PDB entry: 5LEY)¹²⁰. Models of each regulatory particle protein were generated with Robetta^{134,135} and docked as rigid bodies into the EM density map with UCSF Chimera¹¹⁷. Nucleotides were placed by fitting the crystal structure of PAN (PDB entry: 3H4M)¹³⁶ into the density.

Secondary structure prediction for regions that were modeled partly or completely *de novo* were obtained using the server psipred¹³⁷. The initial rigid body refinement was performed using real space refinement in Phenix¹³⁸ and modeling was carried out manually in COOT.

Secondary structure restraints were generated using *phenix.ksdssp* and all secondary structure restraints were visually inspected and required restraints were added manually. The real space refinement was performed over several iterative rounds.

2.2.8.7 Validation

For datasets which yield two or more main conformations, the structural model is validated by a cross reference test. Here, the particles corresponding to one conformation were refined on a model with the alternative conformation. The final 3D reconstruction relaxed back to the originating model and the sorting was considered as valid.

2.2.9 Visualization of the Conformational Space of the Human 26S Proteasome

If not stated differently, particles with and without Oprozomib bound to the proteasome were treated as separate subsets. All particles of one subset were refined against the initial 26S proteasome map using RELION to gain alignment parameters. This reduces the subsequent calculations in the classification step. The resulting aligned images were randomly split in subsets of 100,000 particles and a RELION 3D-classification¹³⁹, yielding 40 classes per subset, was performed, without aligning the particles again. Each resulting 3D class was further refined with the assigned particles using RELION.

In total, 346 classes were obtained. To further analyze the motions between the classes we used principle component analysis (PCA). The result of a PCA are eigenvectors that describe the largest covariance within the dataset. In aligned 3D volumes of the same molecule, the largest covariance are primarily movements within the molecule¹⁴⁰. The eigenvectors can be used as conformational coordinates¹⁴¹. Before applying PCA, the refined 3D-classes were aligned in UCSF Chimera against a model of the most rigid part of

the 26S complex; the 20S proteasome subcomplex. This is necessary to avoid calculating eigenvectors which describe shifts and rotations of the 3D-classes among themselves. 3D classes from datasets with and without Oprozomib were combined and normalized, and subsequently eigenvectors were calculated using PCA. Hence, the eigenvectors describe the movements found in both datasets and allow us to compare the results. One can then describe the conformers X_i on a coordinate e_n (the eigenvector describing movement n) by:

$$X_i = a_{n,i}e_n + \bar{X} \quad (2.2)$$

where \bar{X} is the average volume, e_n is a specific eigenvector and $a_{n,i}$ is a linear factor. In other words, e_n is a conformational coordinate and $a_{n,i}$ places the conformer X_i at its specific place on this conformational coordinate. The addition of the mean volume results from the definition of PCA. Eigenvectors and their corresponding trajectories can be sorted according to their contribution to the overall mobility.

The movements described by the conformational coordinates might however be composed out of several primitive motions of the molecule. Therefore, one cannot assign a single measure (e.g. rotation angle, translation movement) to all of these movements. The following movements were found and are listed descending in the value of the covariance:

Table 2.5: Eigenvectors and the corresponding conformational changes.

Eigenvector	Description
1	Rotation of the Lid and translation of the ATPase domain
2	Resolution differences
3	Conformational stabilization of Rpn9
4	Conformational stabilization of Rpn5, 10 and 12; Movement of Rpn1
5	Motion of Rpn1; Conformational stabilization of Rpn9, 10
6	Translation of Rpn2, 3, 7, 12
7	Stretching of the Lid; Movement of the central helical bundle (Rpn3, 6, 8, 11); Movement of ATPase domain
8	Rise of the ATPase (including Rpn1); Sinking of Rpn2 and 8
9	Rotation of Rpn1
10	Small movements

To understand the motion described by the eigenvectors, video trajectories were interpolated using equation 2.2 and subsequent morphing in UCSF Chimera. Then, for each 3D class the linear factors with respect to each eigenvector were determined. By placing the different conformers on the reaction coordinates energetic conclusions can be drawn. Knowing the number of particles assigned to each class, we can calculate their free energy

differences $\Delta\Delta G$ by the *BOLZMANN* Factor:

$$\Delta\Delta G = k_B T \ln\left(\frac{p_i}{p_0}\right) \quad (2.3)$$

where T is the absolute temperature, p_i is the number of particles in state i and p_0 is the number of particles in the most populated state¹⁴². The number of particles belonging to each 3D was counted from the respective data output files from RELION¹¹⁵. Free energy differences were calculated using equation 2.3 as multiples of $k_B T$. From equation 2.3 it becomes clear that regions with high energies have a lower number of single particles belonging to them. To visualize the energy landscape with and without Oprozomib, combinations of two eigenvectors were used as the axis of a new three-dimensional coordinate system. The 3D classes were placed as data points in these landscapes with the dimensions being the respective linear factors $a_{n,i}$ and $a_{m,i}$, and the difference in free energy $\Delta\Delta G$. We could then describe energy landscapes in which the molecule moves by interpolating between these discrete states.

To account for false-positives, for example 3Ds which are classified in two separate classes but do only differ slightly, we applied a final binning of close data points. Therefore, all data points within a given distance were averaged. This distance was set to the half-width of the peak around one linear factor. These landscapes have important limitations. In contrast to for example Molecular Dynamics simulations, the 3D volumes yielded from single particle analysis sample the conformational space discrete and sparse. Hence, large areas in the landscapes, especially those of high energy, are highly interpolated. This is also apparent in the fact that the very low sampled areas close to unfolding and complex decomposition are not accessible to this method. However, this method offers an opportunity to quantify the results of 3D classifications and, as in our specific case, allows us to learn about the influence of small molecule binding on the functional conformational landscape of a macromolecular machine.

This method was developed by Dr. David Haselbach and Felix Lambrecht in the Structural Dynamics Department at the Max Planck Institute for Biophysical Chemistry, Göttingen.

Chapter 3

Results

3.1 Native Human 20S Proteasomes and in Complex with Inhibitors

The structure determination of macromolecular complexes by X-ray crystallography depends on the availability of crystals that diffract to suitably high resolution. Crystallization conditions are known for 20S proteasomes from various organisms, and crystal structures up to a resolution of 2.4 Å were previously published^{16,23,25,143}.

In this section, the outcome from novel purification strategies, new crystallization conditions and post-crystallization procedures with the resulting high-resolution structures of the native human 20S proteasome and its complexes with 20S inhibitors are presented.

3.1.1 Purification and Crystallization of the Human 20S Proteasome

The starting point for the successful structure determination of human 20S proteasomes at a significantly higher resolution is a novel concept of protein purification. For human 20S proteasomes, a chromatography-free purification technique was established and optimized (Figure 3.1, A for a schematic description of the procedure and Figure 3.1, B for a representative SDS-PAGE of individual steps of the 20S proteasome purification).

The purification strategy is simple, rapid, and enables the purification of human 20S proteasomes within 48 hours. The purification is chromatography-free and starts with the treatment of cytosolic extract of HeLa cells. After centrifugation of the extract at 30000 x g for 30 minutes (S30 extract preparation), the supernatant is incubated with 2-Iodoacetamide and N-Ethylmaleimide for 30 minutes and centrifuged at 100000 x g for 2 hours (S100 extract preparation). The resulting supernatant is then subjected to a combination of differential precipitation with the polymer PEG400 and sucrose gradient centrifugation. Fractions containing 20S proteasomes are identified by SDS-PAGE after

each purification step. This procedure reproducibly yields 20 mg purified human 20S proteasomes, starting from 300 ml cytosolic HeLa extract at 10 mg/ml.

The resulting highly soluble and stable human 20S proteasomes have a specific activity of $13 \text{ nmol/mg}^{-1}/\text{min}^{-1}$ in the activation phase (pre-steady-state) and $60 \text{ nmol/mg}^{-1}/\text{min}^{-1}$ in the steady-state phase (Figure 3.1, C). This means that the human 20S proteasomes purified by the chromatography-free purification method have a higher specific activity by a factor of 10 than reported for previous 20S proteasome preparations²².

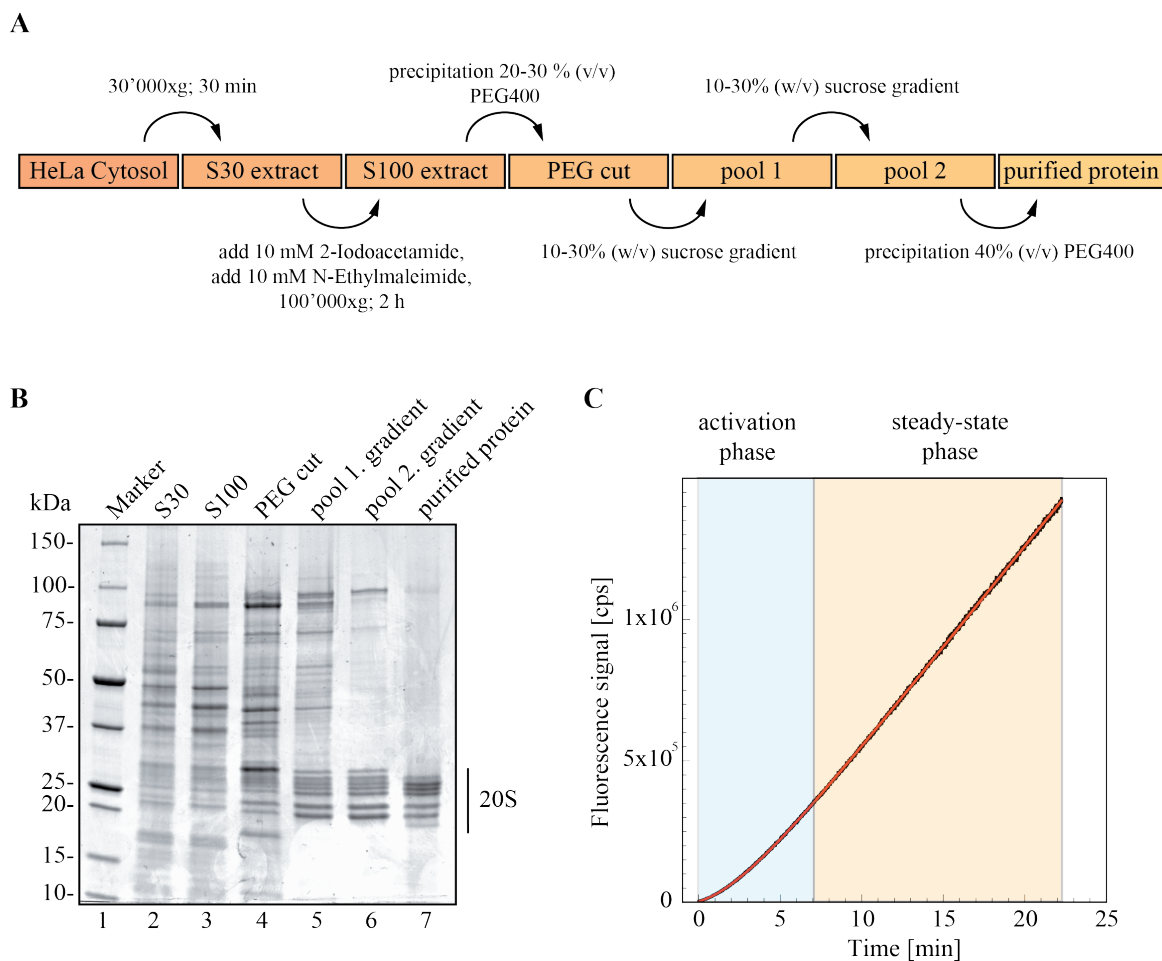


Figure 3.1: The high-throughput purification procedure. (A) Schematic representation of the entire high-throughput pipeline to purify human 20S proteasomes from HeLa cytoplasm. (B) SDS-polyacrylamide gel electrophoresis analysis of distinct steps of the purification procedure. Samples of the S30 (lane 2) and S100 (lane 3) extract, the 20-30 % (v/v) PEG400 cut (lane 4), the pool of the first (lane 5) and second (lane 6) sucrose gradient centrifugation, the purified 20S proteasome sample (lane 7) and a marker as reference (lane 1) are depicted. (C) Activity of the human 20S proteasome from the chromatography-free purification. The increase in fluorescence signal of AMC release by proteolytic cleavage is plotted against time. Figure adapted from Schrader et al., 2016¹²⁰.

3.1.1.1 Preparation of Human 20S Proteasome Crystals

The freshly purified protein is diluted with purification buffer to a concentration of 7.5 mg/ml and crystallized by mixing 0.5 μ l protein and 0.5 μ l crystallization buffer in Chrysem sitting drop vapor diffusion plates over a 500 μ l reservoir of crystallization buffer. Within 4 hours, nucleation takes place and the first small crystals are detectable. To depict the time course of human 20S crystallization, a time-lapse experiment was performed and the results are shown in Figure 3.2. Within 24 hours the crystal grows to its full size, 150 x 150 x 200 μ m³.

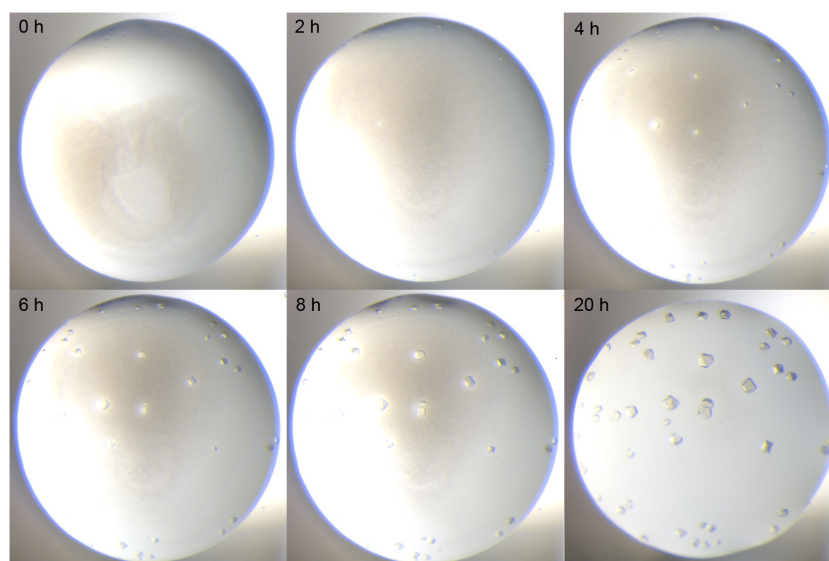


Figure 3.2: Time-lapse experiment of human 20S crystallogenesis. Timepoints are 0, 2, 4, 6, 8, and 20 hours. Nucleation takes place after 4 hours and crystals grow within 24 hours to their full size. Figure adapted from Schrader et al., 2016¹²⁰.

3.1.1.2 Postcrystallization Treatments

To gain a high reproducibility in crystal diffraction to 1.8-2.2 Å resolution, the human 20S proteasome crystals need to be stabilized and dehydrated in a controlled manner. Extensive time and effort was spent to find the optimal procedure.

Finally, three steps seem to be critical and necessary for highly reproducible crystal diffraction: 1) Crystals initially grown at 18 °C are transferred to incubators where the temperature is decreased to 4 °C within 24 hours. When at 4 °C the crystals are carefully transported into the 4 °C room. All postcrystallization treatments take place at 4 °C. 2) The seals are removed and 1 μ l of the reservoir solution is added to the 1 μ l drop. Subsequently, 2 μ l of the crystal stabilization buffer is added to the drop and the reservoir solution is exchanged against the stabilization buffer. The wells are re-sealed and equilibration against the new reservoir by vapor-diffusion takes place in excess of 8 hours at 4 °C. 3) If needed, ligands (e.g. proteasome inhibitors) are soaked into the crystal when

analyzing the inhibitor-proteasome complexes. Inhibitors are soaked into the crystals by adding 4 μl of dehydration buffer, which additionally contains 5 mM of the proteasome inhibitor to gain a final concentration of 2.5 mM. The wells are re-sealed and equilibration against the new reservoir by vapor-diffusion takes place in excess of 12 hours at 4 °C. The full post crystallization protocol is concluded within 30 hours.

3.1.2 Native Crystal Structure of the Human 20S Proteasome

In this thesis, a high resolution structure of the native 20S proteasome at an unprecedented resolution of 1.8 Å is presented. A diffraction pattern of the stabilized and dehydrated human 20S proteasome crystals measured at beamline P14 in Hamburg is shown in Figure 3.3, A.

The determination of the native structure at 1.8 Å provides better insights into the architecture of the entire particle and its active sites. The obtained structures display excellent stereochemistry with values for $R_{\text{work}} = 18\%$ and $R_{\text{free}} = 21\%$ (Table 3.1) and the final crystallographic maps reveals clear electron densities for all 6724 residues and allows the identification of several ligands present in buffers used for purification and crystallization (Figure 3.3, B). The identity of many ions was validated by anomalous difference Fourier maps. In the final structure, 58 chloride, 15 magnesium and 6 potassium ions, in addition to several PEG molecules and more than 3500 localized water molecules were assigned.

Table 3.1: Data collection and refinement statistics of the native 20S crystals. Values in parenthesis denote values for the highest resolution shell. Number of unique reflections used in refinement are shown.

Tag	Native	Native
PDB ID	5LE5	5LEX
Divalent salt	MgCl ₂	Mg(OAc) ₂
Space group	P2 ₁ 2 ₁ 2 ₁	
Unit cell		
a (Å)	113.4	113.9
b (Å)	202.8	203.1
c (Å)	316.0	316.0
Data collection		
Wavelength (Å)	0.976	
Resolution range (Å)	107-1.80	50-2.20
	(1.90-1.80)	(2.28-2.20)
No. of reflections	8923661	2519654
No. of unique reflections	633728	366080
Completeness (%)	99.9 (99.7)	99.2 (98.1)
<I/SigI >	18.5 (0.91)	13.0 (0.9)
CC _{1/2}	1.00(0.32)	1.00(0.36)
R _{p.i.m.}	0.026 (0.71)	0.039 (0.87)
Refinement		
R _{work}	0.184	0.176
R _{free}	0.213	0.220
No. of atoms		
Protein	48205	48134
Ligand/Solvent	3712	3493
R.m.s.d. bond length (Å)	0.018	0.015
R.m.s.d. bond angle (Å)	1.92	1.72
Ramachandran % most favored/ /favored	95.88/3.06	95.60/3.29

In Figure 3.4 the active sites of all three catalytic sites of the 20S proteasome and the identified ligands are shown. At 1.8 Å resolution, a number of differences with respect to the previous published structures become visible. Particularly, a chloride ion is present

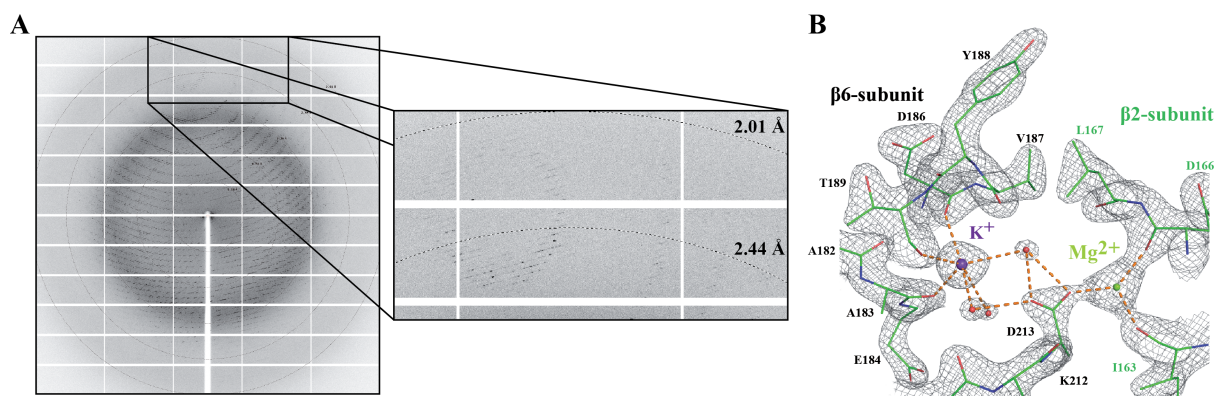


Figure 3.3: Diffraction pattern and structural details at 1.8 Å resolution. (A) A typical diffraction pattern of stabilized and dehydrated human 20S proteasome crystals measured by the oscillation method at beamline P14, EMBL Hamburg. Beam size matched crystal size, exposure time was 40 ms and the oscillation range 0.05°. The diffraction limit is 1.8 Å. (B) The electron density gives insight into the quality of the high resolution structure at 1.8 Å resolution. Shown is a potassium (magenta)-magnesium (light green) double ion site, stabilizing the $\beta 6$ - $\beta 2$ interface. Protein main chains and side chains belonging to the $\beta 6$ subunit are labeled in black. Protein main chains and side chains belonging to the $\beta 2$ subunit are labeled in green. The σ_A -weighted electron density map is shown contoured at 1.5 σ . Figure adapted from Schrader et al., 2016¹²⁰.

in all three sites, which was previously described as a catalytic water (NUK). Soaking experiments, where crystals grown in $MgCl_2$ were soaked with $Mg(OAc)_2$, replace the Mg^{2+} ion against a water molecule. Additionally, up to three localized water molecules (H_2O -1, -2, -3) are present in the active sites. These findings imply a new interpretation of the inhibition mechanism: A water in the NUK position might act as a proton shuttle. The putative role of this water was analyzed at a later point (see below).

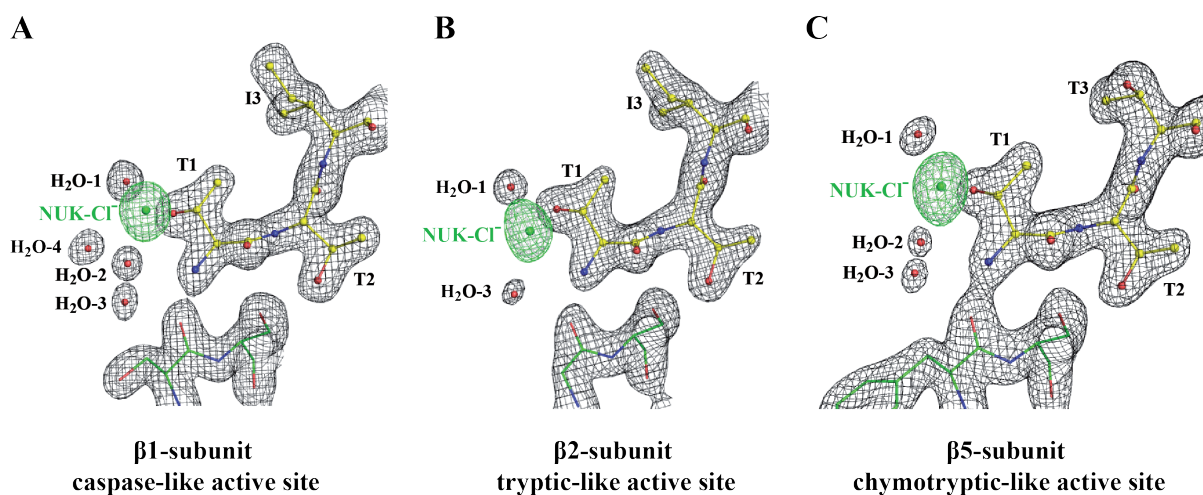


Figure 3.4: Close-up view of all three catalytic sites of the high resolution 20S structure. (A) $\beta 1$ -subunit caspase active site with Thr1, Thr2, Ile3, four H_2O molecules and a NUK chloride (green). (B) $\beta 2$ -subunit tryptic active site is shown in the same orientation as in (A). Shown are two H_2O molecules, as well as the NUK chloride. (C) $\beta 5$ -subunit chymotryptic active site depicted as in (A) and (B), shown are three H_2O molecules and the NUK chloride. The 2mFo-DFc electron density map is shown contoured at 1.5 σ . Figure adapted from Schrader et al., 2016¹²⁰.

3.1.3 Crystal Structures of Seven Inhibitor Complexes of the Human 20S Proteasome

In addition to the native structures, six structures of the human 20S proteasome in complex with inhibitors at resolutions between 1.9 and 2.4 Å were elucidated. Four of these complexes describe proteasomes with inhibitors which are in clinical trials for the treatment of cancer. Binding of these inhibitors to the human 20S proteasome was structurally uncharacterized prior to this work. Oprozomib, Dihydroeponemycin, Ixazomib, and Delanzomib were chosen. They belong to three different inhibitor classes: α',β' -Epoxyketone, α -Ketoaldehyde and Boronic acid. All inhibitors used in this experiments are described to have a specificity for the $\beta 5$ subunit and in all further steps the analysis of the inhibitors is restricted to this active site. In Table 3.2 the most important data collection details and refinement statistics are depicted.

Table 3.2: Crystallographic data collection and refinement statistics of inhibitor-20S complexes. Colors indicate the difference in inhibitor classes. Statistics for epoxyketone inhibitors (blue), ketoaldehyde inhibitors (violet) and boronic acid inhibitors (green) are listed, respectively the PDB entry ID. Values in parenthesis denote values for the highest resolution shell. Number of unique reflections used in refinement is shown.

Inhibitor Class Tag	Epoxyketone				Ketoaldehyde	Boronic acid		
	Oprozomib	Oprozomib	Epoxomicin	Dihydro- eponemycin	Z-LLY- ketoaldehyde	Bortezomib	Ixazomib	Delanzomib
PDB ID	5LEY	5LEZ	5LF0	5LF1	5LF6	5LF3	5LF7	5LF4
Divalent salt	MgCl ₂	Mg(OAc) ₂	MgCl ₂	MgCl ₂	MgCl ₂	MgCl ₂	MgCl ₂	MgCl ₂
Space group				P2 ₁ 2 ₁				
Unit cell								
a (Å)	113.4	113.9	113.1	113.9	113.9	113.4	113.4	114.4
b (Å)	202.7	203.2	202.4	203.5	203.5	202.7	202.6	202.8
c (Å)	315.1	315.2	314.8	316.0	315.6	314.9	314.5	314.3
Data collection								
Wavelength (Å)				0.976				
Resolution range (Å)	170-1.90 (2.00-1.90)	50-2.19 (2.27-2.19)	107-2.41 (2.50-2.41)	50-2.0 (2.07-2.00)	50-2.07 (2.15-2.07)	157-2.10 (2.20-2.10)	94-2.00 (2.10-2.00)	50-1.99 (2.06-1.99)
No. of reflections	2653718	2510786	2519995	4381423	2792074	2017022	3047303	4210019
No. of unique reflections	526170	351230	262073	464668	403247	393306	459417	462522
Completeness (%)	97.5 (99.4)	99.3 (94.3)	99.9 (99.6)	99.8 (98.3)	96.4 (72.3)	98.7 (89.1)	99.8 (99.6)	99.1 (90.0)
<I/SigI>	15.3 (0.83)	15.2 (1.1)	13.1 (0.83)	12.2 (1.0)	12.9 (0.6)	12.4 (0.9)	14.6 (1.0)	11.3 (1.0)
CC _{1/2}	1.00 (0.24)	1.00 (0.40)	1.00 (0.28)	1.00 (0.39)	0.99 (0.22)	1.00 (0.26)	1.00 (0.29)	0.99 (0.34)
R _{p.i.m.}	0.041 (1.03)	0.036 (0.81)	0.060 (1.06)	0.038 (0.69)	0.043 (1.0)	0.052 (0.87)	0.041(1.1)	0.045 (0.81)
Refinement								
Rwork	0.189	0.181	0.168	0.175	0.185	0.183	0.182	0.184
Rfree	0.224	0.222	0.227	0.209	0.226	0.225	0.215	0.217
No. of atoms								
Protein	48208	48372	48372	48302	48219	48331	48272	48272
Ligand/solvent	3756	3882	3385	3839	3718	3888	3809	3794
R.m.s.d. bond length (Å)	0.016	0.015	0.018	0.014	0.013	0.014	0.013	0.012
R.m.s.d. bond angles (Å)	1.80	1.75	1.89	1.71	1.65	1.72	1.68	1.642
Ramachandran % most favoured /favoured	95.58/3.30	95.24/3.45	95.91/2.88	95.68/3.16	95.49/3.35	95.67/3.12	95.62/3.24	95.88/2.99

The high-resolution human 20S proteasome structures in complex with inhibitors reveal differences to earlier published data. The most prominent differences are visible in the 20S-Oprozomib structure at 1.9 Å resolution. After refinement, the linkage of Oprozomib

to the active site revealed a cyclic moiety. Unlike the previously predicted 1,4-morpholine ring closure, the electron density map revealed a larger, 7-membered ring structure. This ring-shaped structure could be modeled as a 1,4-oxazepane linkage, where the C6-methyl group is oriented towards the the inner side of the ring (Figure 3.5). Additionally, all three localized water molecules are displaced by the bound inhibitor and an epoxyketone specific water molecule is hydrogen-bonded to the C6-OH and to Thr21 γ -OH, referred to as EK-H₂O.

These findings suggest that the ring closure proceeds via a nucleophilic attack by the N-terminal amine of the epoxide β carbon and not by the epoxide α carbon, as reported for the 6-ring closure.

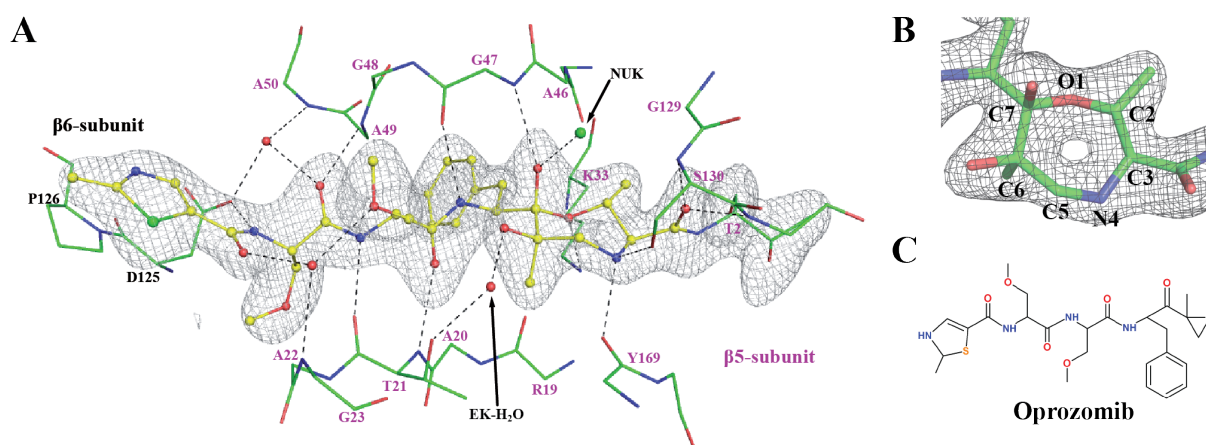


Figure 3.5: High-resolution human 20S proteasome in complex with Oprozomib. (A) The $\beta 5$ active site inhibited by Oprozomib at 1.9 Å. The omit map for the inhibitor, the cyclic linkage, and β Thr2 is contoured at 4 σ . Depicted side chains are enumerated and the NUK chloride is shown as a green dot. The inhibitor is covalently attached to Thr1 are depicted in ball-and-stick representation. Dashed lines indicate hydrogen bonds at ≤ 3.2 Å distance. (B) Close-up view of the 7-membered ring-closure, along with the corresponding omit map contoured at 6 σ . (C) Chemical structure of Oprozomib. Figure adapted from Schrader et al., 2016¹²⁰.

In the following, a multitude of control experiments to validate the 1,4-oxazepane ring formation were carried out: (I) 20S proteasome crystals were grown as described before. After full growth, the crystals were soaked with Mg(OAc)₂ prior to soaking with the inhibitor Oprozomib. In the calculated electron density, an exchange of the chloride molecule for an acetate molecule was detected, while the formation of a 1,4-oxazepane linkage was not affected. As seen in Figure 3.6 the electron density in the active site represents the larger 7-membered ring and an additional acetate molecule is present. This acetate molecule forms hydrogen-bonds to each of the C6-OH and the C7-OH of the 1,4-oxazepane ring as well as a hydrogen bond to the amide of the main chain segment Ser130. These findings show that the exchange of chloride for acetate does not affect the formation of a 7-membered, 1,4-oxazepane linkage.

(II) This experiment was performed to ensure that the formation of the 1,4-oxazepane ring linkage is not a consequence of radiochemistry during X-ray data collection. First,

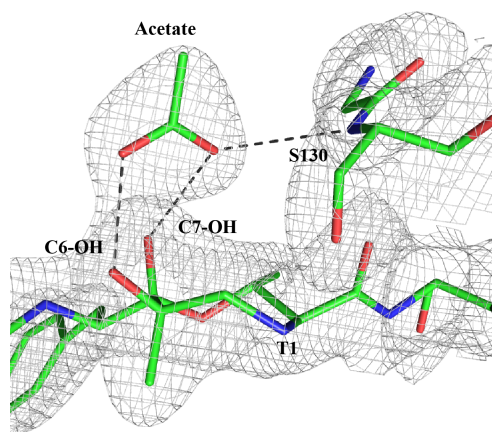


Figure 3.6: Active site of Acetate and Oprozomib soaked 20S crystals. Crystals soaked with $\text{Mg}(\text{OAc})_2$ before soaking with inhibitor, show the presence of an acetate molecule in the active site together with the covalently linked inhibitor. The close-up view shows the 7-ring structure together with the acetate which is hydrogen-bonded to two oxygen atoms of the 1,4-oxazepane ring. Hydrogen bonds are visualized as dashed lines. Figure adapted from Schrader et al., 2016¹²⁰.

a complete dataset at a low X-ray dose (0.7 MGy) was collected (Figure 3.7, A), then the crystal was treated with a high dose (15 mGy) exposure followed by the collection of a second dataset at 0.7 MGy exposure (Figure 3.7, B). The calculated electron density maps revealed no obvious differences and that the 7-ring is not a consequence of radiation damage.

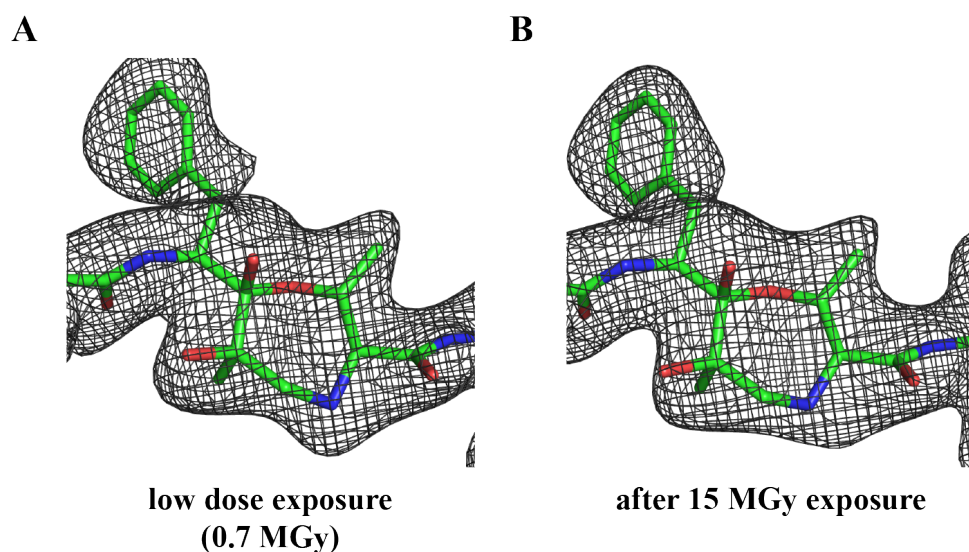


Figure 3.7: Low-dose experiment. Shown are the electron density maps of the ring linkage region from a (A) low-dose and (B) a high-dose exposure. Both maps show electron density for the 1,4-oxazepane 7-membered ring and no obvious differences are discernable. Figure adapted from Schrader et al., 2016¹²⁰.

(III) Next, crystals were soaked with the natural product epoxyketone, Epoxomicin. Diffraction data to 2.4 Å were collected. The structure was calculated by refinement of the integrated and scaled X-ray data against the present model of the native human 20S. The electron density maps in the human epoxyketone-20S proteasome crystal structure revealed density for the bigger 7-ring linkage formation. Modeling the cyclic molecule visible in the inhibited state reveals that it represents the 1,4-oxazepane ring structure. Figure 3.8 illustrates the β_5 active site bound by Epoxomicin at 2.4 Å accompanied by

an omit map for the inhibitor, covalent linkages, and the $\beta 5$ Thr2, as well as the chemical structure of Epoxomicin.

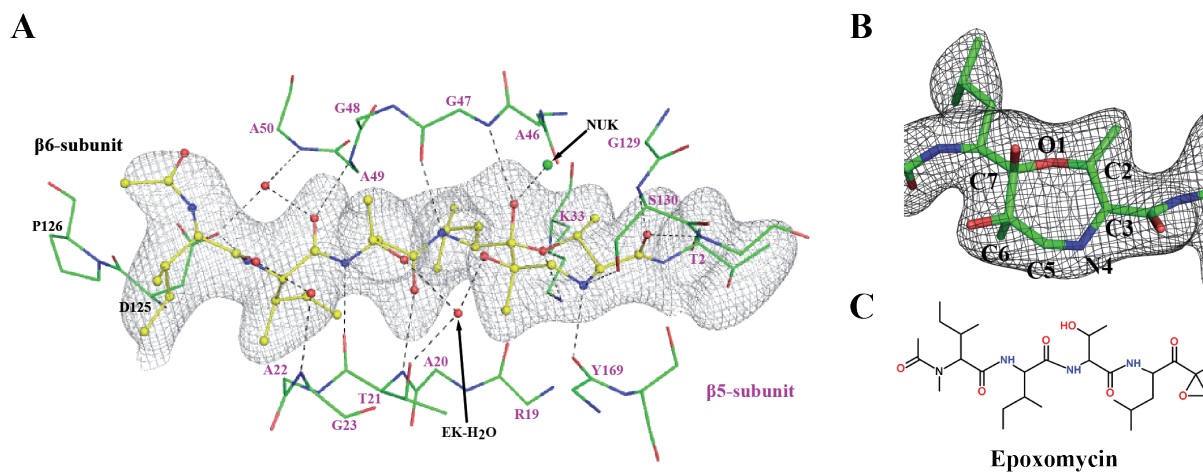


Figure 3.8: Epoxomicin-human 20S proteasome co-crystal structure. (A) Shown is the $\beta 5$ active site inhibited by Epoxomicin at 2.4 Å. The omit map is contoured at 4 σ . Depicted side chains are enumerated and the NUK chloride is shown as a green dot. Dashed lines indicate hydrogen bonds at ≤ 3.2 Å distance. (B) Close-up view of the 7-membered ring-closure, along with the corresponding omit map contoured at 6 σ . (C) Chemical structure of Epoxomicin. Figure adapted from Schrader et al., 2016¹²⁰.

(IV) A high-resolution structure of the human 20S proteasome bound by another natural epoxyketone product, Dihydroeponemycin, was determined. In contrast to the previously investigated epoxyketone inhibitors Oprozomib and Epoxomicin, Dihydroeponemycin shows a methanolic group at the α carbon (Figure 3.9, A and B). At a resolution of 2 Å the difference between an α carbon methyl group and a methanolic group should further confirm the given ring-closure. If the binding would result in the formation of a 1,4-morpholine ring, then the calculated structure would reveal two methanolic groups at the carbon 6 position. Instead, the electron density for the Dihydroeponemycin-20S structure represents a 7-ring closure similar to the Epoxomicin and Oprozomib structures. Here, one methanolic group at the C6 atom oriented to the inner side of the ring is visible (Figure 3.9, C and D).

(V) Since the finding of a 7-ring closure in the inhibited 20S proteasome is described for the first time, it was important to assure that the alternative 6-ring formation is not present in the data and the 7-ring is not just one possible ring closure besides the 6-ring. This question led to the next experiment, to investigate if the 6-ring formation is an alternative ring-closure form. Therefore, a 6-ring model was refined against the Oprozomib-20S X-ray data. The result, depicted in Figure 3.10, showed a poor quality fit. It forces the structure to adapt the 6-ring formation, which leads to tremendous distortions in the molecular geometry of the model: (i) the N4-carbon bonds are elongated by 0.1-0.2 Å, (ii) the C5-alcohol bond is shortened by 0.1 Å, (iii) the bond-angle of the C5-methylalcohol differs by -20 degrees from the expected value, (iv) the van-der-Waals

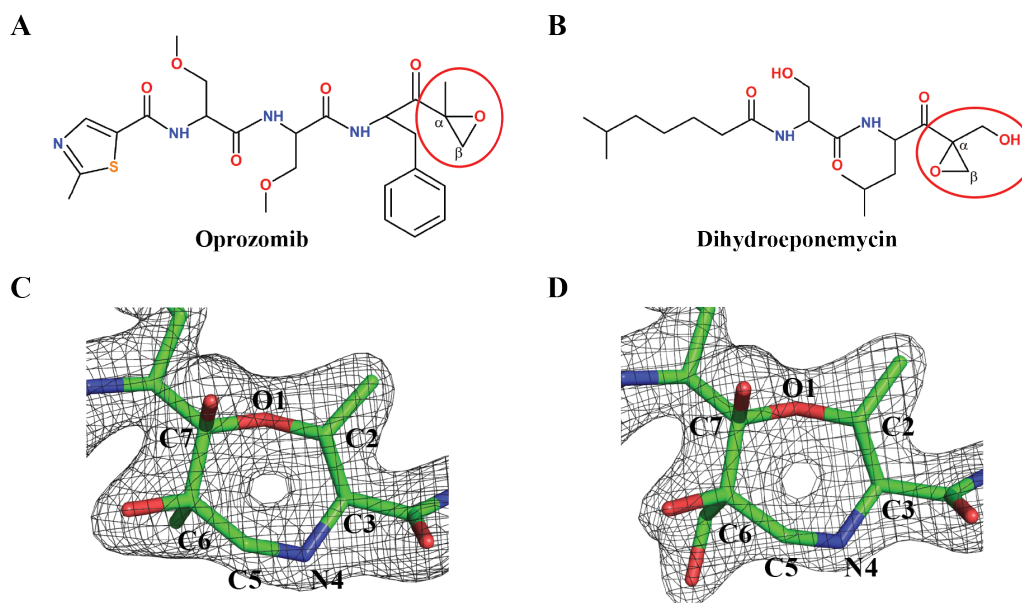


Figure 3.9: Validation of the ring closure in the 20S-Dihydroeponemycin crystal structure. (A) Chemical structure of Oprozomib. (B) Chemical structure of Dihydroeponemycin. In (A) and (B) the red oval highlights the reactive head group: the Oprozomib contains a methyl group and Dihydroeponemycin a methanolic group in the α -position to the ketone. (C) Close-up view of the 7-membered ring-closure upon Oprozomib inhibition, along with the corresponding omit map contoured at 6σ . (D) Close-up view of the 7-membered ring-closure upon Dihydroeponemycin inhibition, along with the corresponding omit map contoured at 6σ . The Dihydroeponemycin structure does not reveal electron density consistent with the presence of two methanolic groups.

distance between the C5-methyl alcohol and two main chain oxygen atoms (R19, Y169) is too short with 3 \AA and would result in repulsion forces, and moreover, (v) strong negative difference density peaks in difference maps contoured at 5σ levels at the C5 methanol oxygen of the 1,4-morpholine ring model, as well as positive density peaks contoured at 4.5σ levels close to positions 4 and 5 of the 7-ring model remained after 6-ring refinement. Adding it all up, the 6-ring formation cannot be considered as an alternative ring-closure upon epoxyketone inhibitor binding.

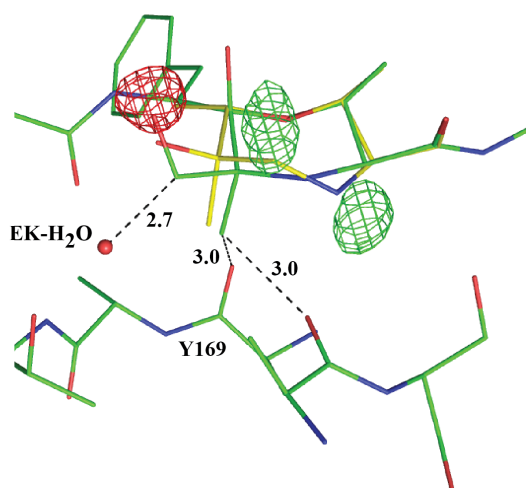


Figure 3.10: Competitive refinement. The competitive alignment of 1,4-morpholine versus 1,4-oxazepane linkage reveals a poor fit and severe distortions can be observed. Shown is an overlay of the active site inhibited by a 7-ring linkage (yellow) and the attempted 6-ring linkage (green). The strong negative difference density is visible at the C5 methanol atom in red, positive densities in green at positions 4 and 5. Figure adapted from Schrader et al., 2016¹²⁰.

3.1.4 Structural Implications of the Six-ring Linkage

To investigate structural implications of a real six-ring linkage, a structure of the human 20S proteasome with the inhibitor Z-LLY Ketoaldehyde was determined and analyzed at 2.1 Å resolution. Z-LLY-Ketoaldehyde belongs to the inhibitor class of the α -ketoaldehydes, which possess only an electrophile in the α position. It is therefore only capable of forming a 6-membered ring linkage.

The structure revealed that the ring-closure is without a doubt formed by six carbon atoms (Figure 3.11). The electron density at the active site shows a clear density for a hydroxyl group at the C5 position of the linkage, which indicates a formation of a 1,4-morpholine linkage. This is unlike previously published data where the ring closure for α -ketoaldehydes was proposed to be a 6-membered heterocyclic, 5,6-dihydro-2H-1,4-oxazine ring.

Considerable differences become visible when comparing the coordination of the presented epoxyketone-inhibited structures forming the 7-ring linkage to the 6-ring forming ketoaldehyde-inhibited structure. First, the NUK chloride molecule is absent and instead a water molecule is present in a new position 1.2 Å away from the NUK chloride side. This water molecule forms hydrogen bonds to the Ser130-amine and γ -OH as well as to N4 and C6-OH of the 1,4-morpholine ring. The C5-OH moiety, characteristic for the 1,4-morpholine ring closure, is stabilized by a dense hydrogen-bond network involving the carbonyl atoms of Arg19 and Tyr169, the nitrogen of Lys33, and the active site H₂O-3 (CAT).

These results indicate that the H₂O-3 might play a role in both proteasomal catalysis of peptide cleavage and in the cyclization step of the inhibition reaction.

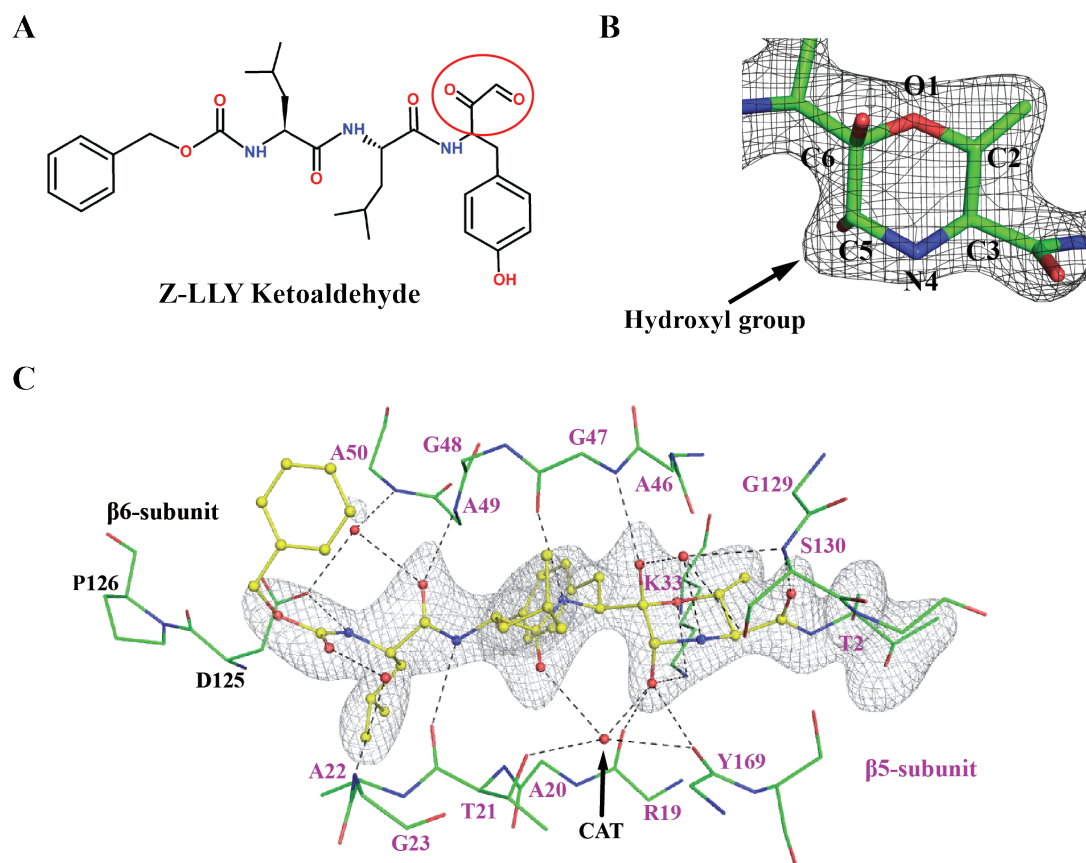


Figure 3.11: Ring-closure in the human 20S proteasome structure in complex with Z-LLY-Ketoaldehyde. (A) Chemical structure of Z-LLY-Ketoaldehyde. The red circle highlights the reactive head group with the electrophile in the α -position. (B) Close-up view of the 6-membered ring-closure, along with the corresponding omit map contoured at 6σ . The arrow points to the C5 position where a clear electron density for the hydroxyl group is visible. (C) The inhibited β 5 active site is illustrated, along with an omit map contoured at 4σ for the inhibitor, the cyclic linkage, and β 5 Thr2. Depicted side chains are numbered. The NUK chloride is shown as a green dot. Dashed lines signify hydrogen bonds (≤ 3.2 Å distance). Figure adapted from Schrader et al., 2016¹²⁰.

3.1.5 Elucidation of the Inhibition Mechanism of Epoxyketone Inhibitors

To address the hypothesis that the H₂O-3 might play a critical role in the function of the human 20S proteasome and in its inhibition, three high-resolution structures of human 20S proteasomes inhibited by boronic acid inhibitors were determined and the active sites were analyzed. Boronic inhibitors were chosen because they mimic the first tetrahedral intermediate state in protein cleavage.

A 2.1 Å structure of the Bortezomib-20S, a 2.0 Å structure of the Ixazomib-20S, and a 2.0 Å structure of the Delanzomib-20S proteasome complex were determined. The details of the site of inhibition are presented in Figure 3.12 for each of these inhibitors. All three calculated structures of the active site do not exhibit a NUK chloride molecule. The NUK chloride is exchanged against a water molecule. In addition, the localized water molecules H₂O-1 and H₂O-2 are displaced by the inhibitor. The H₂O-3 (CAT) molecule remains hydrogen-bonded to the boronic acid moiety, where it might stabilize the tetrahedral intermediate.

Given these observations, it is quite likely that the NUK chloride molecule located on the opposite stereoface of the inhibitor cannot support the cyclization step of α',β' -Epoxyketone and α -Ketoaldehyde inhibitors. In contrast, H₂O-3 (CAT) is well positioned in the active site to support the cyclization of the 6-, or 7-ring, respectively.

Furthermore, on the basis of the crystal structures of the inhibited human 20S proteasome, cluster quantum chemical calculations were performed to better understand the inhibition mechanism. The system of choice is the Dihydroeponemycin inhibitor, with two substantial benefits: the 6- and 7- ring formation can be compared within one system and according to the crystal structure, the spectating hydroxyl moiety of the inhibitor displaces the much more dynamic catalytic H₂O-3.

The previous results indicated that the residues Asp17 and Lys33 cooperate for the activation of the nucleophilic oxygen in Thr1 and the NUK chloride molecule stabilizes the tetrahedral intermediate. The model system depicted for this analysis includes the neighboring residues Lys33, Ser130 and Asp17, the NUK water, and an additional water to complete the hydrogen bond network to Ser130.

Reaction paths were computed and a connected path was obtained: The reaction proceeds via a proton transfer from the Thr1 γ -OH to the Lys33 ϵ -amine, followed by a nucleophilic attack of the hydroxide. Two groups are important for the energetics of this pathway: Asp17 and the NUK water. Asp17 favors the formation of the ϵ -NH₃⁺ group in the lysine and the NUK water forms a strong hydrogen bond with the Ser130 residue. The cluster model is shown in Figure 3.13, A. The electronic energy differences in the computed pathway for the nucleophilic attack on the keto carbon of Dihydroeponemycin

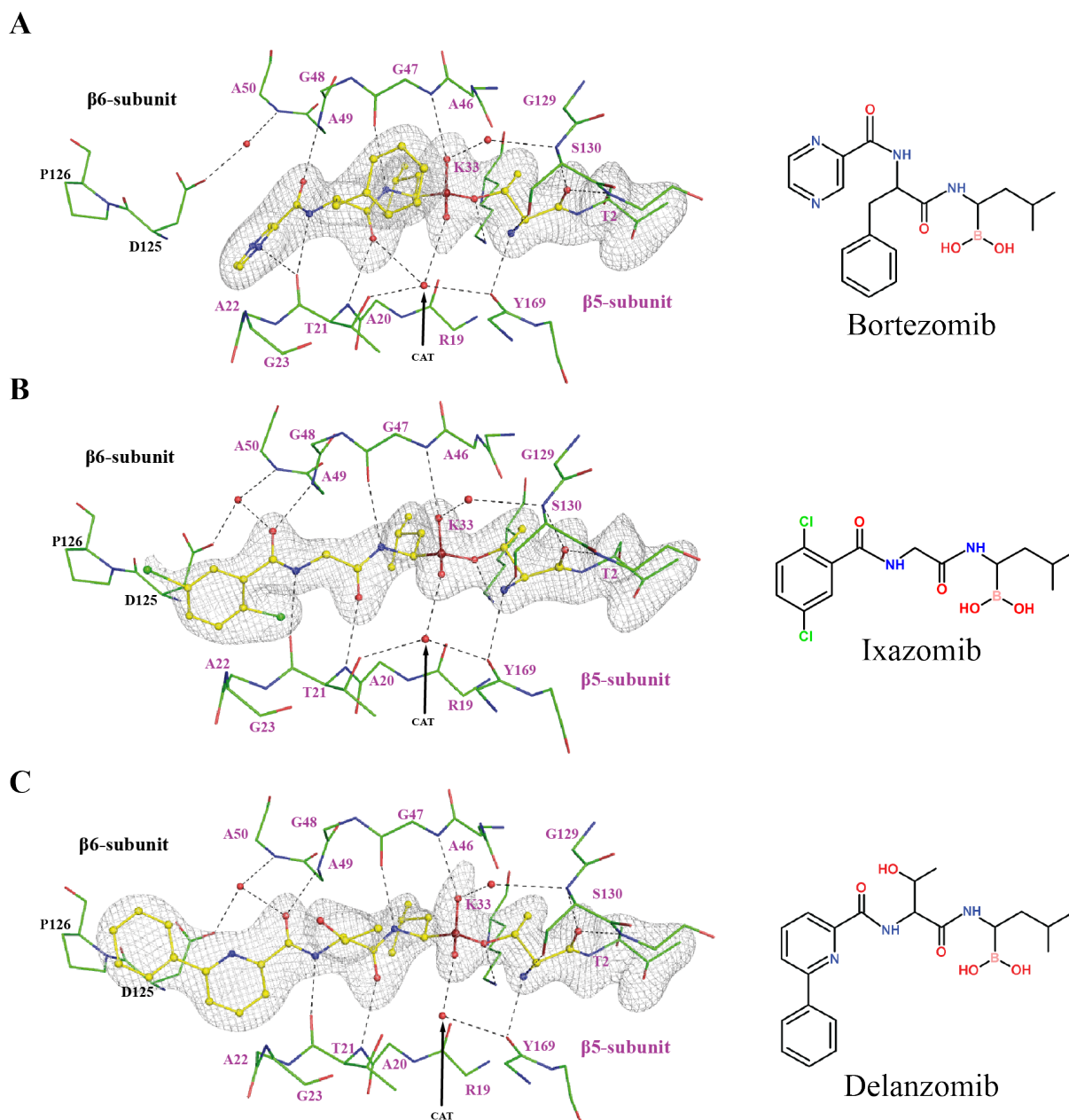


Figure 3.12: Structures of three boronic acid inhibitors bound to the human 20S proteasome. (A) Bortezomib, (B) Ixazomib and (C) Delanzomib. In all three cases, the left panel illustrates the inhibited $\beta 5$ active site of the human 20S proteasome. On the right side the omit map contoured at 4σ for the inhibitor, covalent linkage and $\beta 5$ Thr2 is shown. Depicted side chains are numbered and the NUK chloride is exchanged by a water molecule in all three structures. Dashed lines indicate hydrogen bonds at $\leq 3.2 \text{ \AA}$ distance. The $\text{H}_2\text{O}-3$ (CAT) molecule is shown as a red dot. Figure adapted from Schrader et al., 2016¹²⁰.

are shown in Figure 3.14, A.

In a second set of calculations, the energetics for the pathways leading to 6-ring and 7-ring formations were compared. From the Dihydroeponemycin data a model for the active site was chosen (Figure 3.13, B). This model includes the Thr1 amine, the 3-ring of Dihydroeponemycin and one water molecule was added to complete the hydrogen bond network between the Dihydroeponemycin methanolic OH group, and the Thr1 reactive

NH₂ group. This role is most likely taken over by Ser170 in the native environment. The NUK solvent molecule in addition to the residues Lys33, Ser130 and Asp17 were neglected since the NUK is located on the opposite stereoface of the ring and the residues has little impact. Both pathways were obtained by performing constrained optimizations, keeping the distance between the nitrogen and the target carbon in the inhibitor. The final reaction pathways for the 6- and the 7-ring formation are shown in Figure 3.14. Both pathways originate from the same starting structure that is the tetrahedral intermediate with the amine group facing the epoxide.

Thus, it appears that the reaction's bottleneck is the cyclization step of the inhibition reaction (Figure 3.15). The seven-ring pathway is kinetically favored by approximately 18 kJ/mol and the six-ring is thermodynamically more stable (by approximately 30 kJ/ml). Due to the strain of the transition state, the seven-ring formation is more favored.

The calculations gave no evidence that the NUK solvent molecule participates in the cyclization step due to its location and instead, from the computed pathways and the boronic acid inhibited human 20S proteasome structure, H₂O-3 might serve as a proton shuttle in the cyclization step as well as in the peptide hydrolysis.

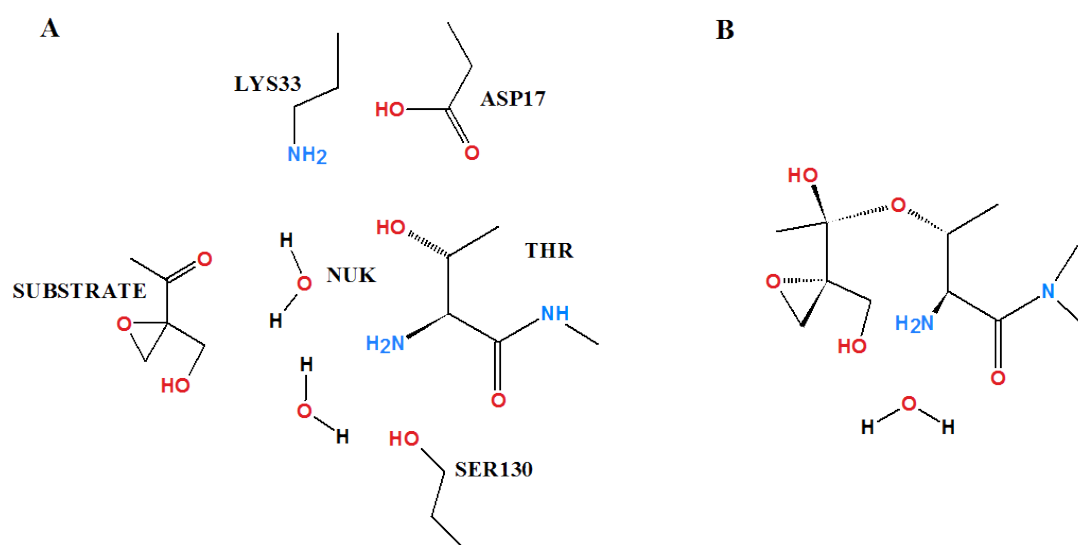


Figure 3.13: Model system used for electronic structure calculations. Model system for (A) tetrahedral intermediate formation and (B) a smaller model system for the ring formation of epoxyketone inhibitors focusing on the Thr1 amine and the 3-ring of the inhibitor, including one water molecule. Figure adapted from Schrader et al., 2016¹²⁰.

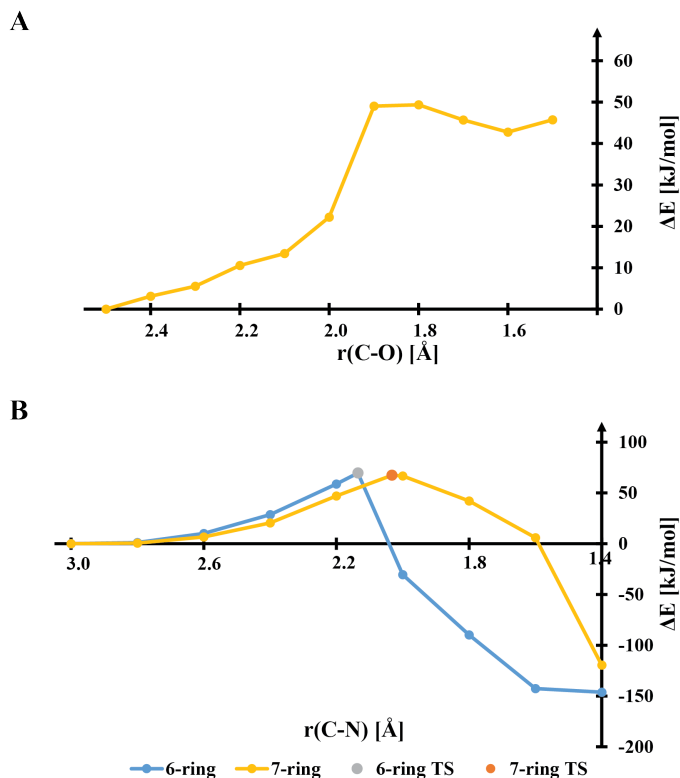


Figure 3.14: Electronic energy differences. (A) Reaction profile of the pathway for the nucleophilic attack at the keto carbon. The α carbons of the capped residues were kept fixed. This profile indicates that Lys33 and Asp17 cooperate to activate the nucleophile and the NUK stabilizes the tetrahedral oxyanion. (B) Full reaction pathways for both six- and seven-ring formations through a similar epoxide ring opening event. The $r(\text{C-N})$ distance corresponds to the distance in the forming bond, and therefore refers to two different carbons. Figure adapted from Schrader et al., 2016¹²⁰.

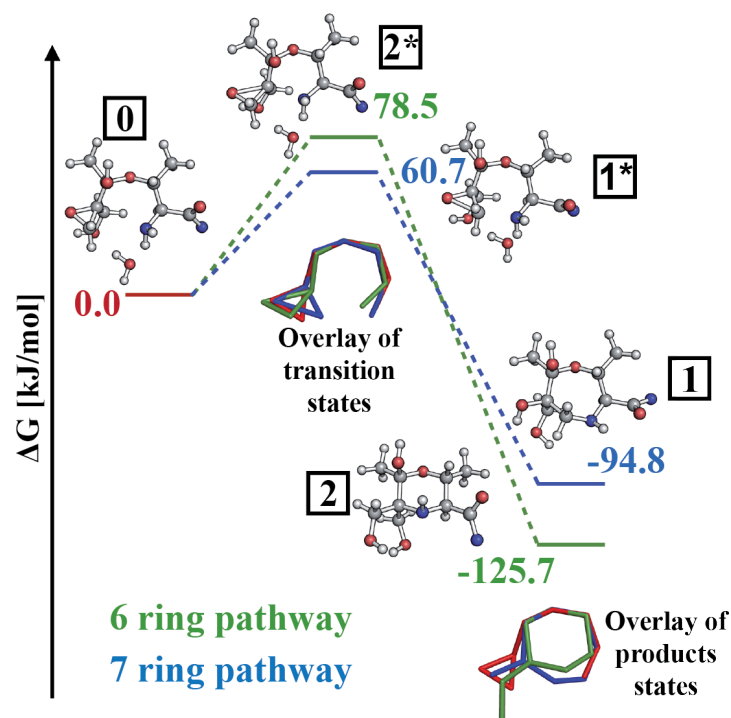
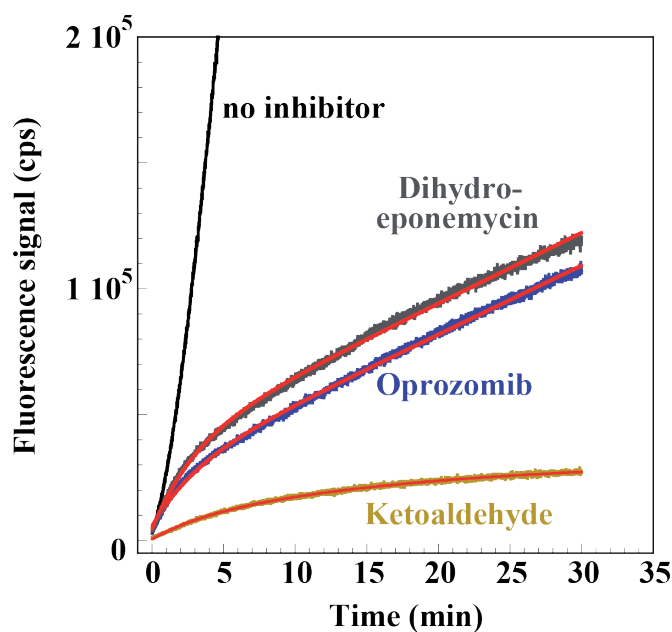


Figure 3.15: Computed reaction pathway of the Dihydroeponemycin model. The starting state, the transition state and the final ring-closure state. A schematic overlay of the transition state and the product states compared to the starting structure (red) is included. The seven-ring reaction pathway starts from 0 through transition state 1* to 1. The six-ring reaction pathway starts from 0 through transition state 2* to 2. Figure adapted from Schrader et al., 2016¹²⁰.

Additionally, kinetic measurements were performed to provide more information about the kinetic preferences of the 6- and 7-ring formation, respectively. The analysis of the first-order inactivation rate constants of 6-ring forming Z-LLY-Ketoaldehyde compared to the 7-ring forming Dihydroeponemycin and Oprozomib indicates that the six-ring formation rate is smaller by a factor of approximately 20 (Figure 3.16). Further, the residual rate of 3 % of the maximum activity detected for both Dihydroeponemycin and Oprozomib confirms that the seven-ring product is thermodynamically less stable. This results in a partially reversible inhibition for epoxyketone inhibitors, which corroborates the observations made by cluster quantum calculations.

Figure 3.16: Kinetic analysis of inhibitor binding. Shown are the kinetic analysis of the first order inactivation rate constants for 6-ring forming Z-LLY-Ketoaldehyde and 7-ring forming epoxyketone inhibitors Dihydroeponemycin and Oprozomib. The analysis of the Ketoaldehyde inhibitor showed no residual activity, indicating an irreversible inhibition mechanism. For the epoxyketones, the residual activity of approximately 3 % indicates a partial reversible inhibition. Figure adapted from Schrader et al., 2016¹²⁰.



3.2 Structural Impact of 20S Inhibitors on the Human Proteasome Holoenzyme

The first part of this thesis focuses on the human 20S proteasome. A large number of crystal structures of human 20S proteasomes in complex with inhibitors were studied, largely because 20S inhibition is an established approach for cancer treatment and much is unknown about their inhibition mechanisms¹²⁰. Proteasome inhibitors have a 20 year history in cancer therapy¹⁴⁴ but the structural impact of 20S inhibitors on the fully assembled 26S proteasome remains almost elusive.

The findings of the inhibition mechanisms cleared the picture about the competitive inhibition of the human 20S proteasome. The information gained from the crystal structures will help to design new inhibitors and improve their effectiveness.

The mystery about proteasome inhibition remains for the regulatory particle of the proteasomal holoenzyme. Does the inhibition affect the 19S particle? Is the inhibition represented by a structural rearrangement or restricted movements within the proteasome? One publication from 2007 provides a first indication that proteasome inhibitors are potent in stabilizing 26S proteasomes against dissociation of the core particle and the regulatory particle¹⁴⁵.

In the following sections, a structure of the human 26S proteasome in complex with the 20S proteasome inhibitor Oprozomib is presented and the structural effects of inhibition are analyzed.

3.2.1 Purification and Analysis of the Human 26S Proteasome in Complex with Oprozomib

Originating from the previously established biochemical method to purify functional human 20S proteasomes, a purification strategy for 26/30S proteasomes was established and is depicted in Figure 3.17. Other than for 20S proteasomes, the 26S proteasome 23 - 30 % PEG400 cut was loaded onto sucrose cushions to gain a concentrated 26S proteasome fraction. Following this step, the purification continues in the same way as for the 20S proteasomes, reproducibly yielding 15 mg human 26S proteasomes, starting from 300 ml cytosolic HeLa extract at a concentration of 10 mg/ml.

By employing isotonic (low salt) conditions throughout the purification, stability of the complex is maximized and the sample is stable at 4 °C for several weeks as validated by SDS-PAGE analysis and EM preparations. Most human proteasomes purified by this method appear to be in the double-capped 30S form. For structural analysis, only single-

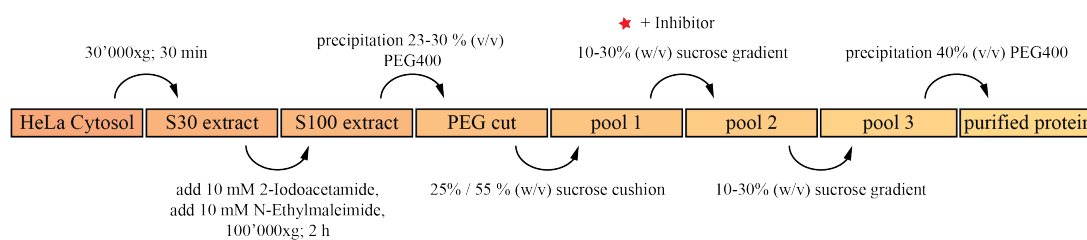


Figure 3.17: Schematic representation of the human 30S proteasome purification. (A) Schematic representation of the entire high-throughput pipeline to purify human 26S proteasomes from HeLa cytoplasm. The purification is completed within 72 hours.

capped 26S proteasomes were used to avoid symmetry problems during image processing and to provide a better angular distribution. Figure 3.18, A shows a representative micrograph.

To study the effect of inhibitors on the 26S proteasome, the epoxyketone inhibitor Oprozomib was chosen and introduced to the proteasome sample at an early stage during purification. The proteasome pool after sucrose cushion centrifugation was treated with 0.5 mM Oprozomib and incubated for 30 minutes at 25 °C before continuing with the sucrose gradient centrifugation.

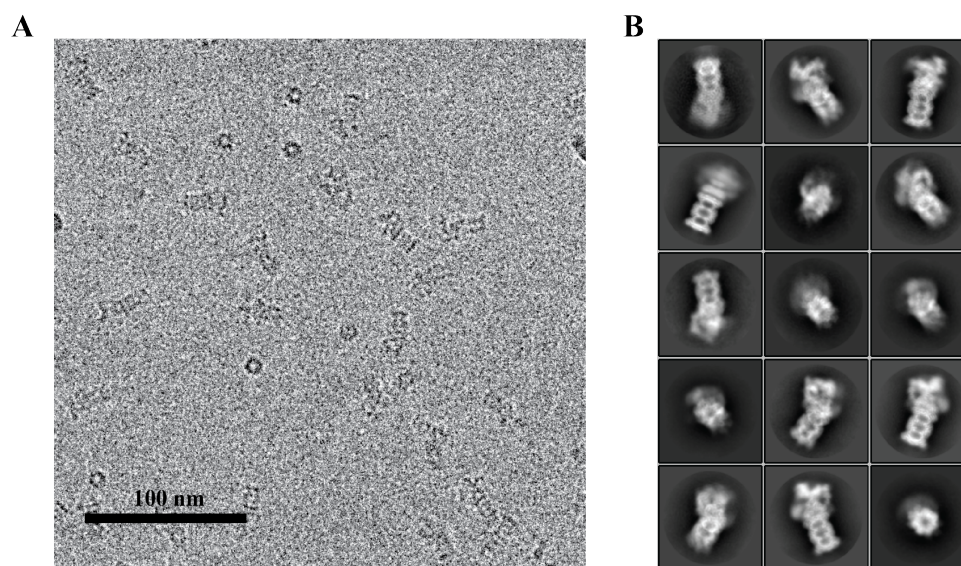


Figure 3.18: Representative micrograph and 2D class averages. (A) Representative cryo-EM micrograph depicting various orientations of Oprozomib-inhibited human 26S proteasomes. By following the purification and cryo-EM preparation procedure described above, high quality micrographs can be obtained. (B) Typical 2D class averages of human Oprozomib-26S proteasome particles. Figure adapted from Haselbach et al., 2017¹⁴⁶.

As part of the ubiquitin-proteasome system, the 26S proteasome detects and binds polyubiquitinated substrates. Earlier publications point to the fact that inhibition of the 20S proteasome leads to a stabilization and jamming of polyubiquitinated substrates in the

19S particle¹⁴⁷. Free ubiquitin or substrate-bound ubiquitin that is attached to the purified proteasome sample might alter the dynamic behavior and therefore the EM data analysis of the molecular machine. Before analyzing the sample on a structural level, we evaluated if the inhibited and non-inhibited samples behave differently in relation to ubiquitin binding. By western blot analysis, we could evaluate if substrate release, hence ubiquitin release is altered in the inhibited sample. For this, the inhibited and the non-inhibited sample were analyzed by SDS-PAGE in equal amounts and subsequently blotted in a western blot chamber against ubiquitin. Figure 3.19 shows the SDS-PAGE and western blot results. Both samples, the inhibited (Oprozomib) and the non-inhibited sample (Native), show antibody signals for ubiquitin (Figure 3.19, lane 3 and 4) but both samples have approximately the same amount of signal and no evidence for accumulation of ubiquitin molecules in the inhibited sample can be confirmed. Thus, it is unlikely that polyubiquitinated substrates or free ubiquitin have an influence on the structural behavior of the inhibited human 26S proteasomes.

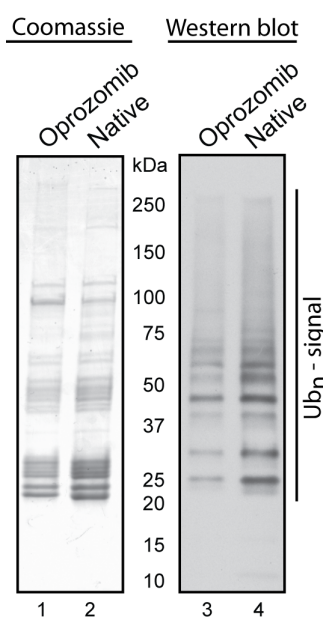


Figure 3.19: Western blot analysis. Purified Oprozomib-inhibited and non-inhibited 26S proteasomes were analyzed by SDS-PAGE and Ubiquitin was detected via western blot analysis. Lane 1 and 2 show Coomassie stained SDS-PAGE gel signals for 26S proteasome proteins. Lane 3 and 4 represent the corresponding Ubiquitin signals detected by western blot analysis. Figure adapted from Haselbach et al., 2017¹⁴⁶.

3.2.2 EM Structure of the Human 26S Proteasome in Complex with Oprozomib

EM sample preparation, data collection and image analysis was performed on Oprozomib-inhibited human 26S proteasomes. First, the freshly purified sample was inspected for quality and particle distribution by negative stain electron microscopy. Subsequently the sample was prepared for electron cryomicroscopy and 18991 EM micrographs were recorded. Figure 3.18, B shows reference-free 2D class averages after several image sorting steps.

To obtain a high-resolution structure extensive hierarchical computational sorting was performed and only particles which represent the major conformational population were included. The results after various computational sorting steps are shown in Figure 3.23. Finally, a cryo-EM structure of the Oprozomib-inhibited human 26S proteasome at a resolution of 3.8 Å was calculated (Figure 3.20, A) and the corresponding model was built (data statistics in Table 3.3). A look into the details of the inhibited 26S proteasome model reveals well-defined densities for the holoenzyme with amino acid side chains in the most stable parts of the molecule and only small variations in local resolution (Table 3.3 and Figure 3.22, A).

The best resolved regions are found in both β subunit rings and in the regulatory particle bound α subunit ring of the 20S core particle at a resolution of about 3.5 - 4.5 Å. The regulatory particle regions are more flexible, and the resolution decreases to the lowest resolution of 6 Å in the most outer parts of the lid with increasing distance from the rigid parts of the particle. Additionally, a clear density for the inhibitor is visible in the $\beta 5$ active site of the Oprozomib-20S complex and the ligand was modeled into the map (Figure 3.20, A).

The structure was investigated with regards to the B-factor values for all individual residues. The B-factors were analyzed in segments of five amino acids. Three quality levels were defined to validate the model building. In the final 3D model, side chains were modeled in areas with a B-factor smaller than 110 Å². Areas with a B-factor between 110 Å² and 150 Å² were truncated to polyalanine. Residues with B-factors greater than 150 Å² were not included in the final map. Figure 3.22 shows the final human 26S proteasome model colored according to the B-factor value. The B-factors range from 25 Å² (low B-factor) to 175 Å² (high B-factor). The local resolution differences of the EM density map and B-factor distribution of the atomic model are well-correlated.

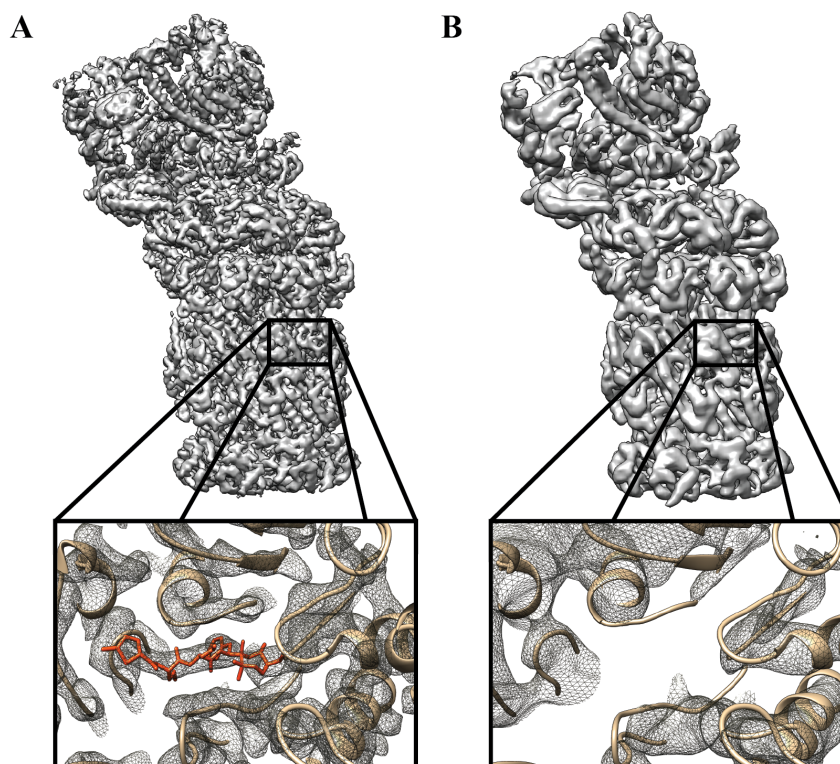


Figure 3.20: Surface view and $\beta 5$ active side of Oprozomib-inhibited and non-inhibited 26S proteasome. (A) Oprozomib-inhibited, (B) Non-inhibited. In both cases, the upper panel shows the surface view of the human 26S proteasome complex and the lower panel shows a zoom-in to show the $\beta 5$ active site. The inhibited structure reveals an extra density for the inhibitor in the $\beta 5$ active site. Figure adapted from Haselbach et al., 2017¹⁴⁶.

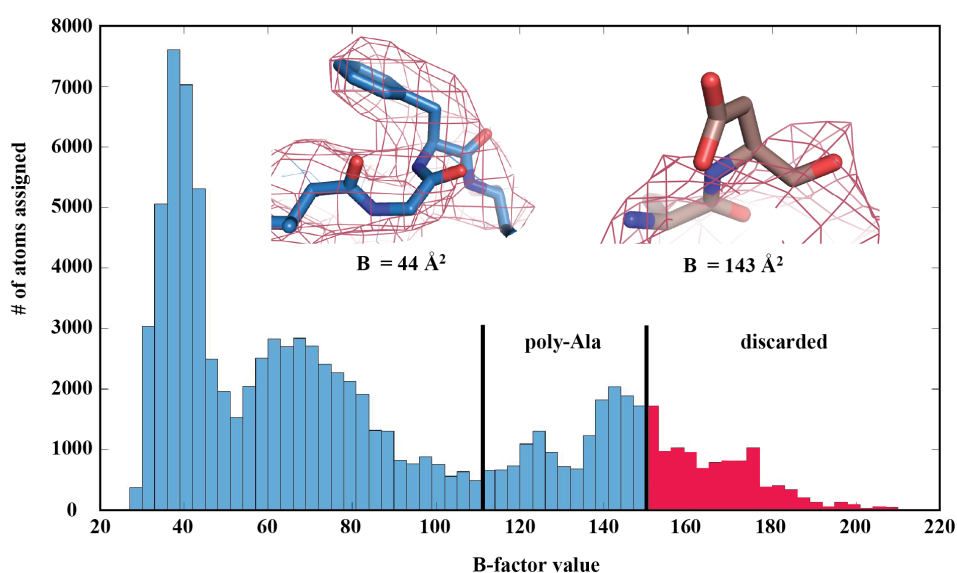


Figure 3.21: B-factor distribution The final human 26S proteasome model analyzed for B-factor distribution. In segments of five amino acids the whole structure was analyzed and three quality levels were chosen to define the level of structural details which are interpreted in the final map. Side chains were included in areas with a B-factor value of 110 \AA^2 or less. Only polyanaline chains are shown in areas of B-factors between 110 \AA^2 and 150 \AA^2 . No residues were modeled in areas with B-factors higher than 150 \AA^2 . Figure adapted from Haselbach et al., 2017¹⁴⁶.

Table 3.3: Human Oprozomib-26S proteasome model statistics.

Data collection	
Particles	233513
Pixel size (Å)	1.27
Defocus range (um)	0.4 - 8 (mean 1.9)
Electron dose (e ⁻ /Å ²)	40.2
Refinement	
Space group	P1
a, b, c (Å)	426.27
α, β, γ(°)	90.0, 90.0, 90.0
Resolution (Å)	3.8
Wilson B (Å ²)	66.3
Map sharpening B-factor (Å ²)	-184.9
Resolution at FSC = 0.143 (Å)	3.83
r _{work}	0.4526
Rachmachandran statistics	
Outliers	2.46 %
Favored	83.02 %
R.m.s deviations	
Bond length (Å)	0.015
Bond angles (°)	1.669
Validation	
EMRinger score	1.94

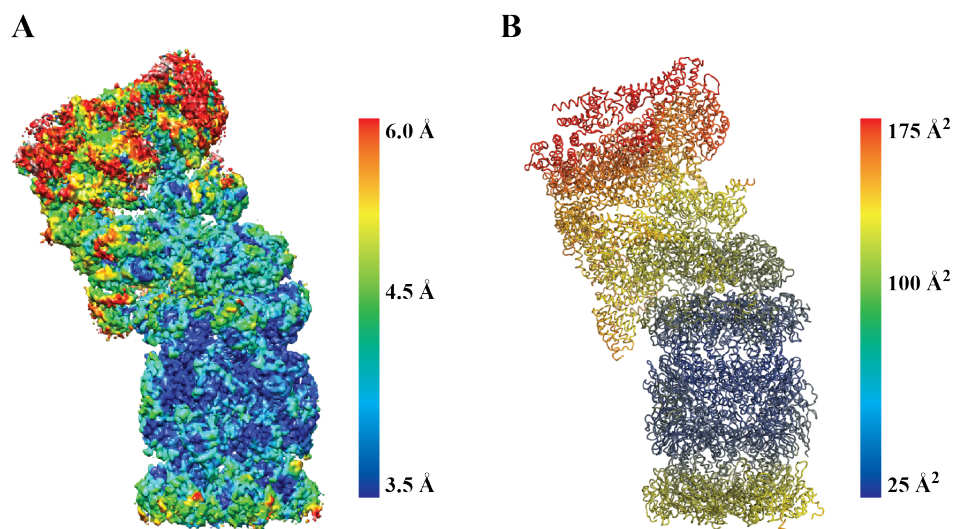


Figure 3.22: Local resolution map and atomic model colored according to the B-factors. (A) Local resolution of the density map of the Oprozomib-inhibited 26S proteasome complex. Resolution ranges from 3.8 Å (blue) to 6 Å (red). (B) Model colored according to the B-factors of all individual residues. B-factors from 25-175 Å² are colored. Only single residues show higher flexibility. Figure adapted from Haselbach et al., 2017¹⁴⁶.

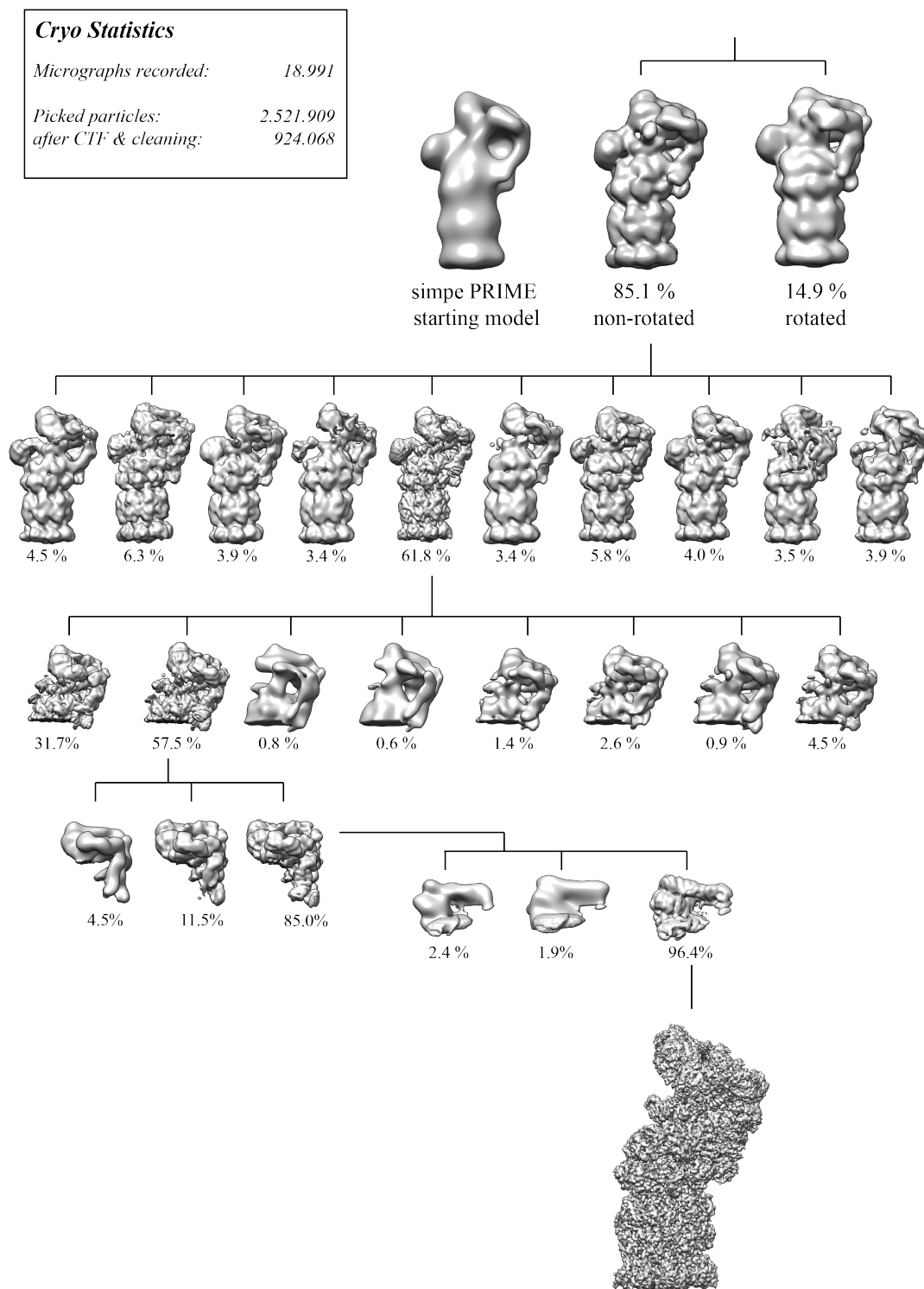


Figure 3.23: Particle sorting scheme. The various computational image sorting steps of the structure determination of the 3.8 Å resolution Oprozomib-inhibited human 26S proteasome. In a first step, an initial 3D model was calculated with the software simple PRIME¹¹⁶. Next, 3D classification was performed and the particles were sorted according to the two main rotational conformations of the regulatory particle: non-rotated and rotated. Particles contributing to the non-rotated state were further classified in three consecutive rounds of classifications. In each round the highest populated class was chosen and a focused classification was performed. First, with a mask for the complete regulatory particle, second, for the lid and lastly, a mask for the Rpn2 protein. The particles remaining after all steps of classification were refined in RELION¹¹⁵ to the final model at 3.8 Å. Figure adapted from Haselbach et al., 2017¹⁴⁶.

3.2.3 Restricted Dynamics in the Inhibited 26S Proteasome

Compared to structures from the literature, the overall conformation of the inhibited 26S proteasome appears to be similar as no significant differences are visible. To address differences between the inhibited and non-inhibited 26S proteasomes in more detail, a non-inhibited sample was prepared and the structure was calculated at a resolution of 4.8 Å. For calculation, the identical image processing and classification protocol was utilized (Figure 3.23).

As seen in Figure 3.20, B, the active site of the non-inhibited human 26S proteasome map shows no extra density and no ligand is bound.

Two major conformational states of the human 26S proteasome were identified during data processing for either inhibited or non-inhibited 26S proteasomes (Figure 3.23). These states agree well with previously published conformational states observed for the 26S proteasome from yeast⁵⁰. In the following, the conformational states are labeled non-rotated and rotated. This categorization is defined by a rotation of the complete lid by 25° with respect to the 20S core particle combined with a motion of the ATPase Rpt4/5 coiled coil towards the ubiquitin receptor Rpn10. A schematic representation of the regulatory movement with respect to the 20S core particle is shown in Figure 3.24, A.

An analysis of all particles of the native human 26S proteasome shows that 60 % of the particles classify into particle classes representing the non-rotated 26S proteasome and 40 % into classes representing the rotated conformation. Applying the same analysis to the particles of the Oprozomib-inhibited 26S proteasome reveals a surprising result. Here, 90 % of all particles represent the non-rotated state and only 10 % are found in the rotated state (Figure 3.24, B).

These findings lead to the question whether binding of the inhibitor stabilizes the non-rotated state. To address this, a control experiment was performed. A freshly purified human 26S proteasome sample was treated with the epoxyketone inhibitor Epoxomicin, executing the same inhibition mechanism as Oprozomib. Negative stain electron microscopic analysis and subsequent particle sorting reveals that most particles are in the non-rotated state, as seen for the Oprozomib-inhibited 26S proteasome (Figure 3.24).

These results indicate that inhibition by epoxyketone inhibitors leads to a stabilization of the non-rotated state. 90 % of the inhibited proteasome particles are in the substrate-binding state and only 10 % in the rotated, substrate-processing state.

The human proteasome inhibited with epoxyketone inhibitors appears to be restricted in its dynamics which leads to this conformational limitation has a direct connection with the inhibitory effect of epoxyketone inhibitors.

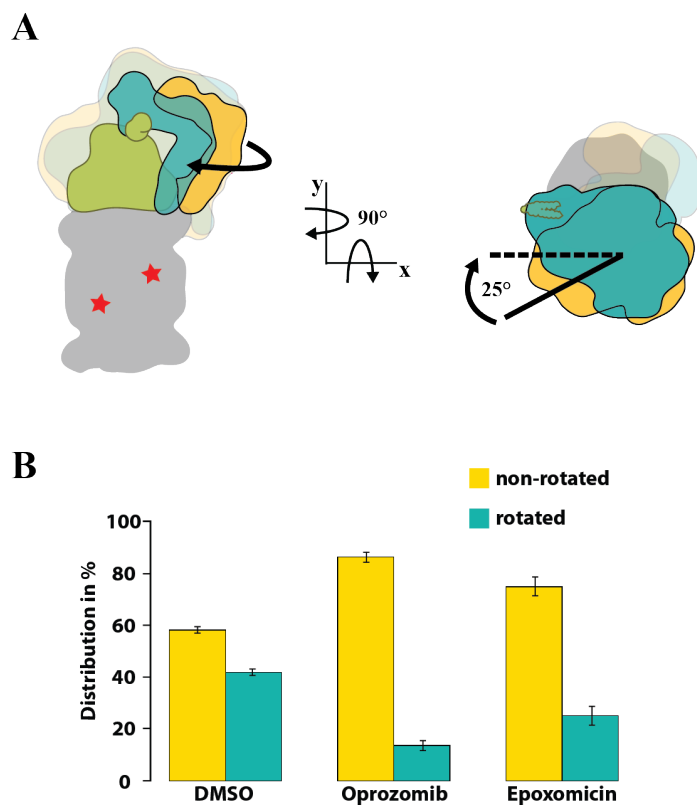


Figure 3.24: Schematic representation of 19S motion and particle distribution. (A) Simplified illustration of the rotation of the lid by 25° in respect to the 20S core particle and movement of Rpt4/5 towards the ubiquitin receptor Rpn10. The red asterisk marks the β_5 active side. (B) Bar chart of the particle distribution between non-rotated and rotated state in three datasets: DMSO (control), Oprozomib (epoxyketone), Epoxomicin (epoxyketone). Figure adapted from Haselbach et al., 2017¹⁴⁶.

3.2.4 The Energy Landscape of the Lid Movements

Only a relatively small subset of particles was used to obtain the non-inhibited and Oprozomib-inhibited proteasome maps at 4.8 and 3.8 Å (4 % and 12 % respectively). The final non-inhibited and the Oprozomib-inhibited human 26S proteasome maps adopt a nearly identical non-rotated conformation. This leads to the hypothesis that the differences between the inhibited and non-inhibited 26S proteasome are manifested in those particles not used for the high-resolution reconstruction. A novel method to extract valuable information about the dynamic properties of the proteasome and the conformational stabilization elicited by drug binding is presented next.

To make use of the concealed information of all particles which were not part of the final 3D model, a method to study the conformational variability in a quantitative manner was created. In a first step, extensive 3D classification was performed. The classification resulted in 346 classes, 224 of the non-inhibited 26S Proteasome and 122 of the inhibited. Each of the 3D volumes was then refined independently. The final 3D volumes were aligned on the core particle using UCSF Chimera, low-pass filtered, and normalized prior to analysis. To study the conformational variability in the regulatory particle, alignment on the core particle is necessary.

To analyze the motions of the regulatory particles of final 3D classes, Principal Component Analysis (PCA) was used: PCA is a statistical analysis by which a set of observations of possibly correlated variables is converted into a set of values of linearly uncorrelated variables, the principal components or eigenvectors. PCA can be used to reduce the complexity of a data set, resulting in a reduced dataset with only basic information.

Here, the resulting eigenvectors describe the largest covariance which represents the primary movement within the regulatory particle. Analysis of the particle motion was concentrated on the first two modes of motion: The first mode corresponds to the lid rotation with respect to the 20S particle and the second mode describes a more complex rearrangement in the lid. In Figure 3.25 (B), the modes are depicted in a simplified way.

With the known particle numbers corresponding to each mode, the transformation of a conformational landscape into an energy landscape, which describes the complexity of the regulatory particle movement in a quantifiable manner, is possible. Additionally, this method allows the direct visualization of changes in the 26S proteasome dynamics upon inhibitor binding.

The results of this analysis are the energy landscapes shown in Figure 3.25. The energy landscapes have to be interpreted according to the coloring. Blue areas represent many particles and a low energy state at the same time. In contrast, red areas have less particles but higher energy states.

Comparing the energy landscapes of the non-inhibited and the Oprozomib-inhibited human 26S proteasome, significant differences become visible: For the Oprozomib-inhibited

human 26S proteasome, the energy landscape shows wide areas with only few particles but very high energy (red) and a defined blue area with high numbers of particles and low energy. In contrast, the energy landscape of the non-inhibited particles appears to be more flat, represented with only little areas in dark red or blue. The particles have the capacity to adopt conformations on a large scale and no accumulation of particles in one defined area is visible.

These findings indicate a significant limitation in the proteasome's motion upon inhibition. Inhibition of the 20S particle seems to influence the lid motion and the energy landscape reflects a significantly decreased lid movement by creating an energy barrier. It is less likely that the molecules reach the rotated state (red area) and more particle images populate the thermodynamically favored conformation in the blue area, having this energy barrier. In total, only 14 % of the analyzed proteasome particles of the inhibited sample contribute to the red area, hence they represent the rotated state. In addition, we found that the lid rotations of the inhibited sample and the non-inhibited sample differ in the maximum degree of rotation: In the inhibited sample, particles with a lid rotation of maximal 20° are found, whereas particles of the non-inhibited sample represent a maximum rotation of 25° .

The structural consequences of this smaller amplitude of lid rotation in inhibited 26S proteasomes concentrate on the regulatory particle domain orientation. In the non-inhibited 26S proteasome, the coiled coil of the AAA+ ATPase domains Rpt4/5 reach the interface between the domains Rpn10 and Rpn9. Interestingly, upon a lid rotation of only 20° the interface is not reached and only Rpn10 is in contact to the coiled coil. This limited rotation might have far-reaching consequences on the proteasome's function.

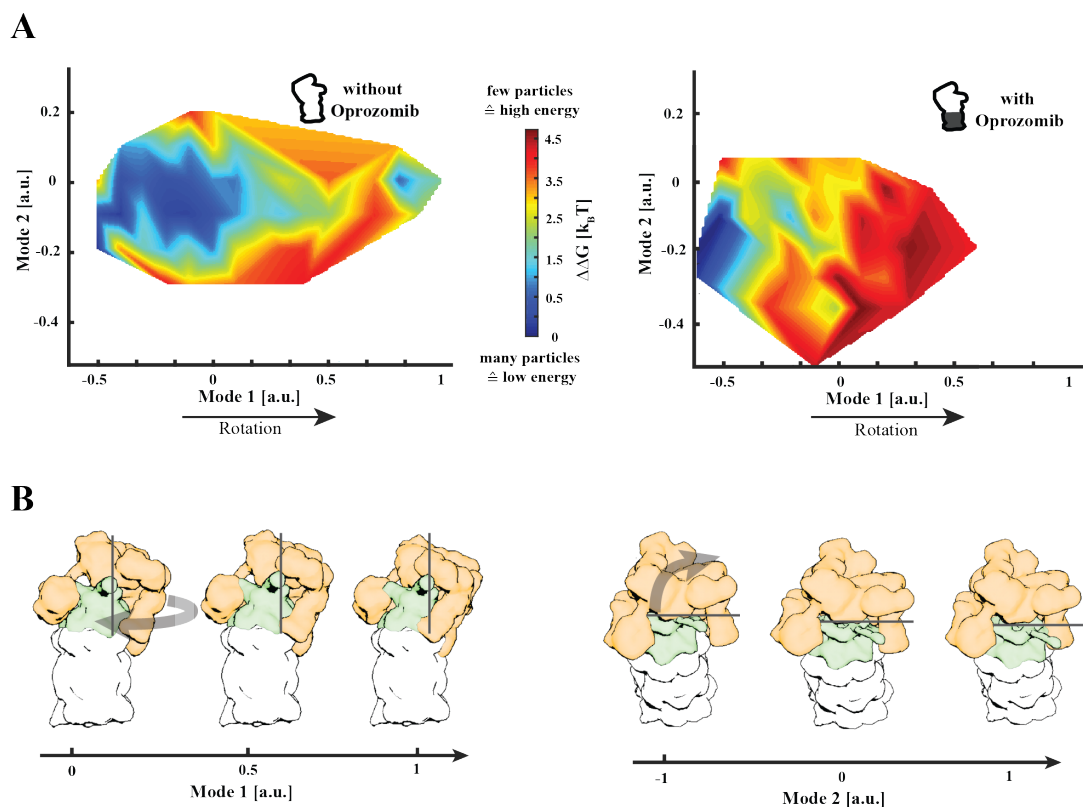


Figure 3.25: Energy landscapes and graphic representation of the modes. (A) Shows two energy landscapes, one of the non-inhibited and one of the Oprozomib-inhibited particles, respectively. Blue areas represent many particles and low energy, red areas mark areas with less particles and higher energy. The dark blue area in the right plot represents all particles belonging to the high resolution 3.8 Å structure, found in a local energy minimum. In (2) the complex movement modes of the proteasome lid are represented in a graphical approach. Parts colored in orange belong to the regulatory particle, green represents all parts of the ATPase. The arrow indicates the direction of the main movement. The gray lines help to distinguish between the 3 main conformational stage. Figure adapted from Haselbach et al., 2017¹⁴⁶.

Chapter 4

Discussion

In this thesis crystallographic analysis of the native human 20S proteasomes and seven inhibitor-20S proteasome complexes was performed and the structural impact of 20S inhibitors on the proteasome holoenzyme was studied by single particle cryo-EM.

The results obtained provide an important contribution to the understanding of proteasome inhibition. The key achievements of this thesis can be summarized as follows:

1. Optimized and robust pipeline for the production, purification and crystallization of human 20S proteasomes.
2. Native human 20S proteasome crystal structure at 1.8 Å resolution identifies solvent molecules and functionally important differences with respect to previously published data.
3. Crystal structures of four previously uncharacterized inhibitor complexes of the human 20S proteasome with clinically relevant inhibitors and determination of novel inhibition chemistry.
4. Cryo-EM structure determination of the inhibited and non-inhibited human 26S proteasome.
5. Identification of long-range allosteric regulation of the human 26S proteasome by 20S core particle inhibitors.

4.1 Pipeline for Structure-based Analysis of Human Proteasome Inhibition

The successful crystallographic and electron cryomicroscopic studies rely on a high level of reproducibility in generating proteasomes of high purity and abundance. Sample homogeneity should allow high-quality electron cryomicroscopic analysis and a reproducible crystallization. Hence, great efforts were undertaken to develop a purification procedure for both, human 20S and 26S proteasomes.

Purification of proteasomes from various eukaryotic sources thus far rely on chromatography-based protocols. In this thesis, a generic procedure has been introduced, which overcomes the disadvantages of chromatographic purification, such as high costs and the lack of transferability to proteasomes from different sources. This new method allows the purification of proteasomes from different tissues using the same protocol of PEG fractionation and density gradient centrifugation. The presented low-cost, chromatography-free method results in a high yield of highly soluble and stable complexes. This gentle purification formed the basis for structural analysis of proteasome-inhibitor complexes presented in this thesis and is transferable to a multitude of macromolecular complexes from all organisms.

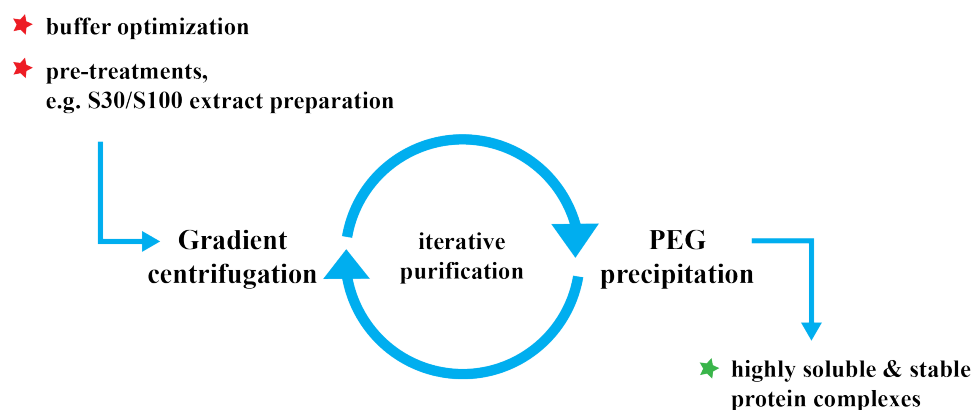


Figure 4.1: A chromatography-free purification procedure at constant ionic strength. PEG precipitation and gradient centrifugation is repeated iteratively until the desired purity/homogeneity is reached. Iterations may differ in PEG concentration and/or gradient composition/density. The method is adaptable to many protein complexes from all organisms.

The choice of a buffer system was a critical step in developing a method to purify functional human 20S and 26S proteasomes. In cells the composition of the fluid surrounding all proteins is very complex. In the laboratory one has to define the best reduced composition of a medium in which the protein is most stable. This medium is mostly a buffer substance supplemented with a mixture of salts. Proteins behave differently in varying buffer and pH conditions and every molecule has its own favored buffer composition.

A generic method that allows to search for the most stabilizing buffer and pH condition was developed by colleagues¹⁴⁸. The chromatography-free purified human 20S proteasome sample showed its most stable condition in the buffer substance Bis-Tris at a pH of 6.5. This correlates with the physiological pH of intracellular fluids between 6.5 and 7.5¹⁴⁹. All previously published 20S purifications were performed in Tris-HCl buffer at a pH of 7.5^{150,25}.

Very stable and durable protein complexes were purified utilizing the gentle purification procedure and the most stabilizing buffer-pH combination. The proteolytic specific activity is an important indication for the proteasome's quality. The chromatography-free purified human 20S proteasomes has a specific activity that is by a factor 10 higher than reported for previous human 20S proteasomes²².

4.2 Native Human 20S Proteasomes Structure at 1.8 Å Resolution

Previously known crystallization conditions for 20S proteasomes require high protein concentrations. For yeast proteasomes the concentration for successful crystallizations lie in the range of 30 to 40 mg/ml. We found a new crystallization condition for the human 20S proteasome. Human 20S proteasomes obtained from chromatography-free purification crystallized in a crystal form not yet described for 20S proteasomes. The optimum protein concentration is reproducibly at 7.5 mg/ml and a drop size of 1 μ l (1:1 mixture with mother liquor). With this comparatively small amount of protein, screening of many different crystallization conditions and protein-ligand complexes is possible on a large scale.

Human 20S proteasome crystals needed to be stabilized and dehydrated in a controlled manner. Complete isotropic diffraction data sets to 1.8 Å resolution were collected, utilizing a complex postcrystallization protocol. For human 20S proteasomes the crystallization and postcrystallization buffer is identical to the purification buffer (Bis-Tris pH 6.5).

The high-resolution human 20S proteasome structure at 1.8 Å resolution reveals a number of functionally important differences of the 20S proteasome active sites with respect to previously published 20S structures. A chloride ion was identified in all three catalytic sites and it was shown that this solvent molecule acts as a proton shuttle. In previous structural studies a water molecule was assigned in the chloride position^{16,25,143,151}. This water molecule was described in the yeast 20S proteasome as an ideally positioned solvent nucleophile involved in both intramolecular autolysis and substrate proteolysis by mediating proton transfer between Thr1O γ and Thr1N^{16,25}. Since the solvent molecule in this position is easily replaced as shown by several experiments it is unlikely that this solvent molecule acts as a nucleophile.

In addition, three localized water molecules were identified in the high quality electron density of the human 20S proteasome catalytic site. These water molecules were not previously described and the possible role of these solvent molecules in the active site of proteasomes was addressed in further experiments.

The possibility to describe the active site of the human 20S proteasome at an unprecedented resolution opens up the opportunity to investigate ligand binding in the active sites at a whole new level. With structures at 1.8 Å resolution the information content of the electron density map increases 3-fold compared to the previously published data. The resolution of the previously published 20S structures from *S. cerevisiae* would allow for identification of the ligands in the active sites but the data are severely anisotropic that results in poor electron density maps^{16,152,153}. X-ray data from higher organisms was collected at relatively low resolution which makes it impossible to obtain a detailed view

of the ligands and solvent molecules in the active site^{23,22,44,25}.

With the availability of the excellent model for the native human 20S proteasome, now structure determination of 20S proteasome structures can occur within minutes by automated refinement. Ligands can then be rapidly identified and modeled.

4.3 Human 20S Proteasome Inhibition

In recent years, several co-crystal structures of the yeast 20S proteasome in complex with inhibitors were elucidated at resolutions between 2.5 and 3 Å. These structures were used to describe the mechanism of proteasome inhibition^{70,25,73}. The electron density in the active site of the 20S proteasomes was of insufficient resolution and quality to model the inhibited state in atomic detail. Binding mechanisms of epoxyketone, ketoaldehyde and boronic acid inhibitors were proposed based on these co-crystal structures^{70,73,152}.

In this thesis, crystallographic analysis of seven co-crystal structures of the human 20S proteasome with cancer therapeutics was performed. The crystal structures of human proteasome-inhibitor complexes were elucidated at improved resolutions between 1.8 and 2.2 Å. The inhibitors adopt antiparallel β sheets in the active sites of the human 20S proteasome. These β sheets are stabilized by direct hydrogen bonds between the conserved residues of the β -type subunits and main chain atoms of the ligand. The excellent electron density provides insight into the inhibited active site at an atomic level as never seen before, and new information about the binding mechanisms and the role of localized solvent molecules was identified.

Epoxyketone Inhibitors

A mechanism for epoxyketone inhibition was presented long before this study started. The inhibition was described as an irreversible reaction of the N-terminal amino group of the Thr1 with the α -carbon atom of the epoxide, resulting in a 6-membered 1,4-morpholine ring closure⁷⁰. The observations leading to this hypothesis were made in yeast 20S proteasomes inhibited by the epoxyketone inhibitor Epoxomicin at a resolution of 2.25 Å⁷⁰. Three co-crystal structures of human epoxyketone-20S complexes were analyzed and a revised description of epoxyketone inhibition was made. The crystal structures of epoxyketone inhibited human 20S proteasomes show a density for an additional atom in the binding site. This identified the formation of a 7-membered 1,4-oxazepane ring structure upon inhibitor binding. This observation was confirmed by theoretical simulations and a series of control experiments. Hence, these findings allow a novel chemical mechanism for the inhibition of 20S proteasomes by epoxyketone inhibitors to be proposed (Figure 4.2): The γ -hydroxyl group of the Thr1 of the proteasome active site reacts with the ketone moiety of the epoxyketone inhibitor, as described for the predicted 1,4-morpholine ring formation. The N-terminal amino group of Thr1 then reacts with the carbon atom of the epoxide that is in β position to the ketone. The carbon atom of the epoxide in β position is less hindered for a reaction with the N-terminal amino group of Thr1.

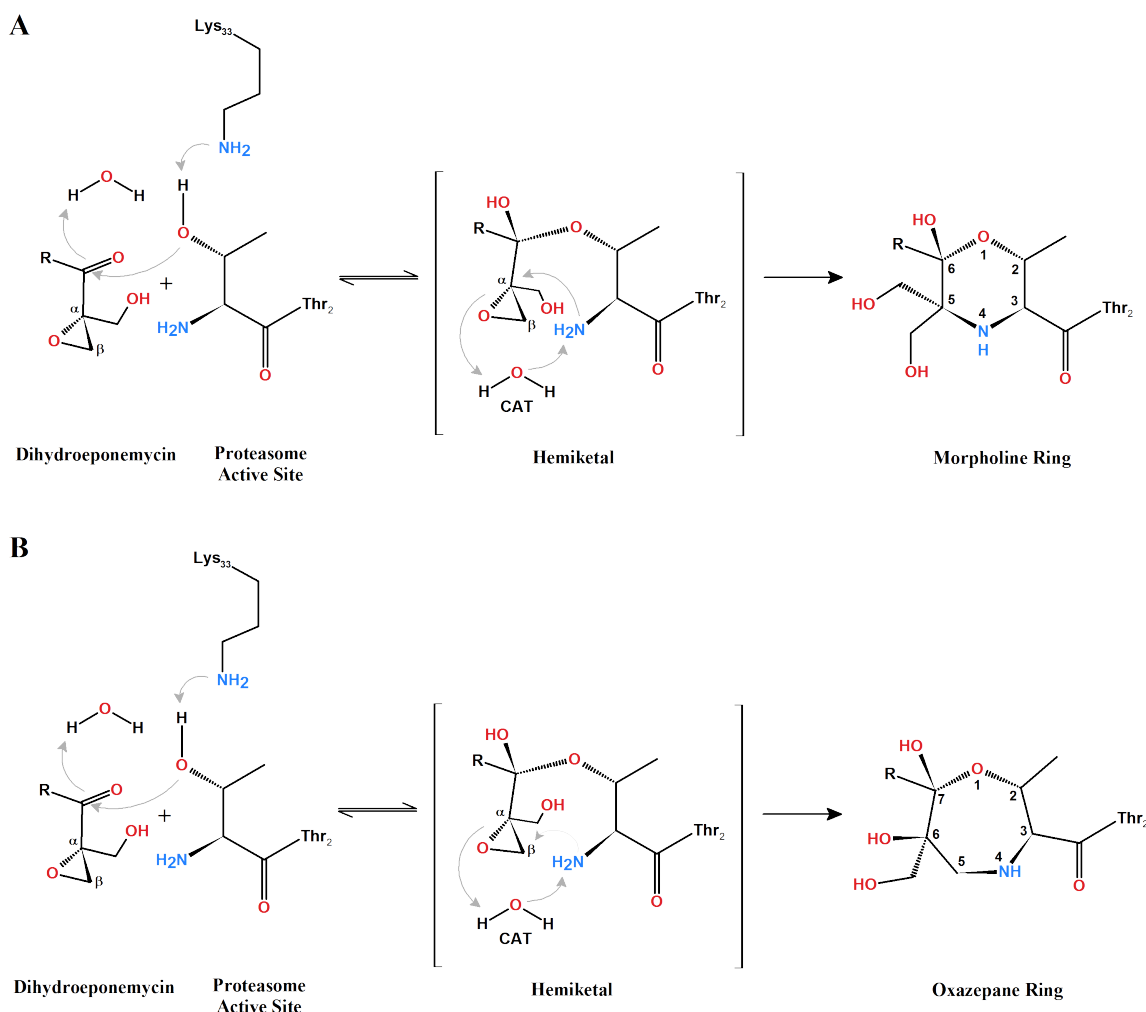


Figure 4.2: Comparison of 6- and 7- ring forming reaction mechanisms for Dihydroepone-mycin. (A) The reaction mechanism for epoxyketone inhibitors proposed thus far using the example inhibitor Dihydroepone-mycin. Groll et al.⁷⁰ proposed that the Thr1-O γ initially reacts with the ketone to form a hemiketal (middle). The N-terminal amine of Thr1 then reacts with the epoxide α -carbon atom resulting in a 1,4-morpholine linkage. (B) The novel inhibition mechanism which leads to the formation of a 7-membered 1,4-oxazepane linkage. Here, the Thr1 N-terminal amine is involved in a nucleophilic reaction with the epoxide β -carbon atom.

Since it is difficult for crystallographers to interpret whether only one binding mechanism occurs or if a mix of two structures is present, a multitude of control experiments were carried out. The results showed unequivocal evidence that the electron density allows only the 7-ring formation in the human 20S proteasome.

Researchers previously describing the inhibition mechanism, suggested the 6-ring formation based on Baldwin's rules⁷⁰. Their observation of chemical reactivities in the Epoxomicin inhibited yeast 20S proteasome lead to the assumption that the 6-ring is formed by a *exo*-tet process, whereby the 7-ring is formed by an *endo*-tet process. *Exo*-tet is favored over *endo*-tet. It was stated that the 6-ring *exo*-tet is the favored and therefore prominent mode of epoxyketone inhibition.

The chemical rules defined by Baldwin were incorrectly applied to the epoxyketone

inhibition by Groll et al.⁷⁰. In short, the Baldwin rules provide the terminology needed to discuss cyclization reactions, allow a classification of cyclization, and suggest a set of rules to define the favorable modes of ring closure¹⁵⁴. Cyclization described by the Baldwin rules is characterized by three prefixes. The first one provides the number of atoms forming the ring, starting at a value of three. The second prefix describes the position of the bond that has to be broken for cyclization of the smallest ring in the structure: *exo* and *endo*. *Exo* means that the breaking bond is outside of the formed ring, whereas *endo* describes that the breaking of the bond happens inside the ring. Lastly, the prefix - tet (tetrahedral), - trig (trigonal), and - dig (diagonal) refers to the hybridization of the atom at the site of the ring closure. With greater understanding based on thousands of examples, a number of extensions and revisions of the Baldwin rules have arisen. One extension was introduced for 3-membered ring structures, the epoxides. Cyclization that involves a nucleophilic epoxide ring opening should not be termed *endo-tet*. The use of both, *exo-tet* and *endo-tet* for epoxide closures is stated as misconception. The breaking epoxide C-O bond is located outside the newly formed ring and each cyclization should be considered *exo-tet*^{155,156}. That means all epoxyketone ring-formations have to be classified *exo-tet*. Here, epoxyketone inhibitors bind in a 7-*exo-tet* process. By the Baldwin rules the 7-*exo-tet* process is not favored or disfavored over the 6-*exo-tet* ring closure. Hence, this argument was neglected in our studies.

We utilized epoxyketone inhibitors because they are the most advanced and specific proteasome inhibitors known to date. With an irreversible binding mode and no known site effects to date is this class of inhibitors desirable as cancer therapeutic. Utilizing the robust pipeline to obtain structural information at higher resolution the atomic details of the epoxyketone inhibition mechanism were shown. For epoxyketones it was outlined that only one of the two electrophilic groups of the epoxide is involved in the inhibition. Here, only the carbon in the β -position to the ketone reacts with the N-terminal Thr1 of the proteasomal active site. Based on the novel inhibition chemistry, there are several possible options for the design of new irreversible proteasome inhibitors exhibiting dual electrophilic head groups.

Ketoaldehyde Inhibitors

To explore the structural implications of a "true" 6-ring linkage, the ketoaldehyde inhibitor Z-LLY-Ketoaldehyde was subjected to structural analysis. Like epoxyketones, ketoaldehyde inhibitors take specific advantage of the unique catalytic mechanism employed by the proteasome. The inhibition mechanism for ketoaldehydes proceeds only via a carbon atom in the α -position of the ketone with the Thr1 of the 20S proteasome active site.

The crystal structure of the Z-LLY-Ketoaldehyde-20S complex was determined at 2.1 Å resolution with high quality electron density in the active sites. The concept of ketoaldehyde binding in the yeast 20S proteasome was published five years ago⁷³. Interpretations of the active site's electron density at 2.7 Å lead to the assumption that the inhibitor forms a 6-membered heterocyclic, 5,6-dihydro-2H-1,4-oxazine ring⁷³. Ketoaldehydes harbor a reversible binding mechanism, due to the Schiff base. Unexpectedly, the binding mechanism for ketoaldehyde inhibitors was misinterpreted.

Our 2.1 Å resolution data confirm a 6-ring formation, but unlike the heterocyclic ring closure, the electron density reveals a rigid 6-ring morpholine linkage. This indicates that a water molecule is not released from the carbinolamine. The morpholine ring that was predicted to be a transition state is the final product of this inhibition (Figure 4.3). This observation could only be made because of excellent electron density at the site of inhibition.

Further, the high resolution structure of the Z-LLY-Ketoaldehyde inhibited human 20S proteasome allowed to identify that the H₂O-3 molecule is involved in the hydrogen-bond network of the C5-OH moiety. This implicated a putative role of this water in the binding mechanism of inhibitors which was confirmed in later inhibition studies with boronic acid inhibitors.

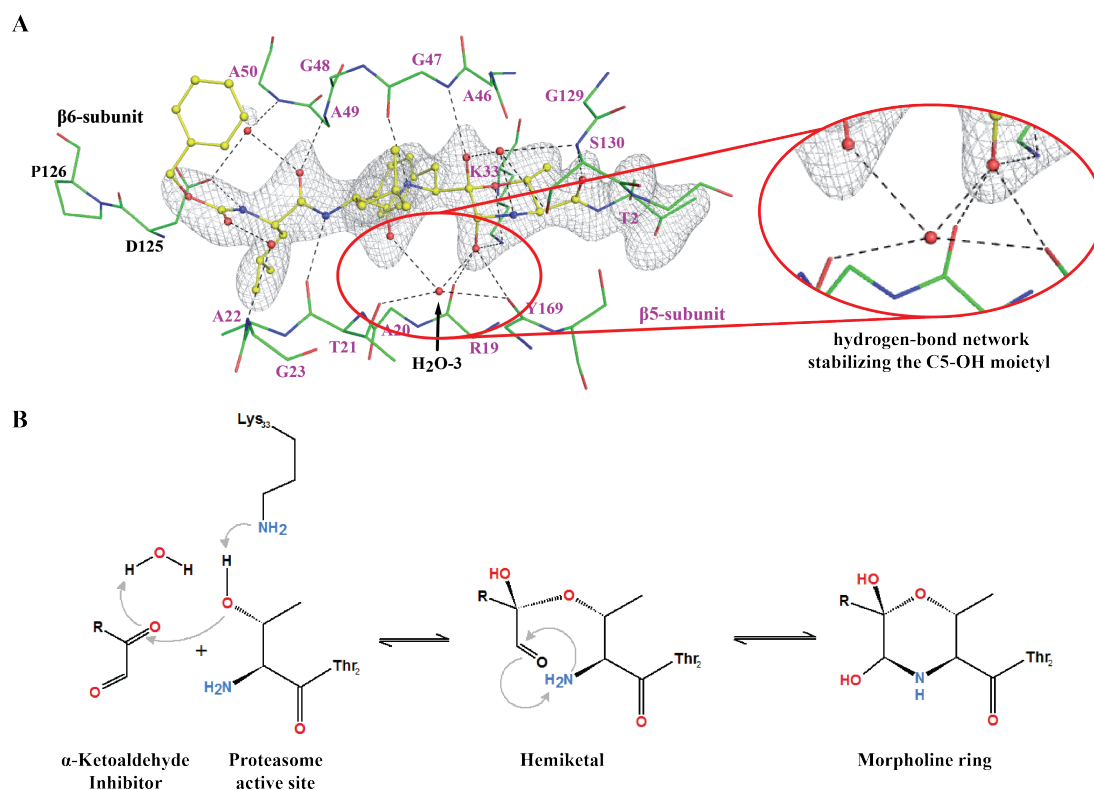


Figure 4.3: Human 20S proteasomes inhibited by Z-LLY-Ketoaldehyde. (A) Hydrogen network of the C5-OH moiety. The H₂O-3 molecule is identified to be involved in the stabilization. (B) Proposed inhibition mechanism for α -Ketoaldehydes. The electron density in the active site shows a six-membered ring with a clear density for a hydroxyl group at the C5 position of the linkage. Z-LLY-Ketoaldehyde inhibition results in a 1,4-morpholine linkage.

Boronic Acid Inhibitors

The binding mode of boronic acid inhibitors mimics the first tetrahedral intermediate state in substrate proteolysis. Boronic acid inhibition was analyzed to address the putative role of the H₂O-3 water molecule in the active site.

Boronic acid inhibitors Bortezomib, Ixazomib and Delanzomib were chosen for X-ray analysis. The organization in the Bortezomib inhibited chymotryptic-like site of yeast 20S proteasome was analyzed previously at 2.8 Å resolution¹⁵²: The boron atom of the tetrahedral boronate adduct interacts covalently with the Thr1 O_γ. The strictly conserved oxyanion hole Gly47N is hydrogen-bridged to one of the acidic boronate hydroxyl groups. The tetrahedral boronate adduct is stabilized by an additional hydrogen-bridge of a second hydroxyl moiety with the N-terminal Thr1 amine atom.

We could evaluate and redefine the critical interactions of boronic acid inhibitors with the human 20S proteasome active site. Boronic acid-20S proteasome complex structures were determined at 2.0 and 2.1 Å resolution. We found that the H₂O-3 stays in a prominent position upon inhibitor binding in orientation to support the cyclization step of ring-forming inhibitors (Figure 4.4). H₂O-1 and H₂O-2 are displaced from the active site upon inhibitor binding. H₂O-3 is hydrogen-bonded to one hydroxyl group of the boronic acid moiety, stabilizing the tetrahedral state. From computed pathways and on the basis of the inhibitor-20S proteasome structures we propose that the H₂O-3 most likely serves as the decisive factor in the cyclization step in ketoaldehyde and epoxyketone inhibition. The significance of these findings might allow for a better understanding of the catalytic details of inhibition and additional inhibitor design.

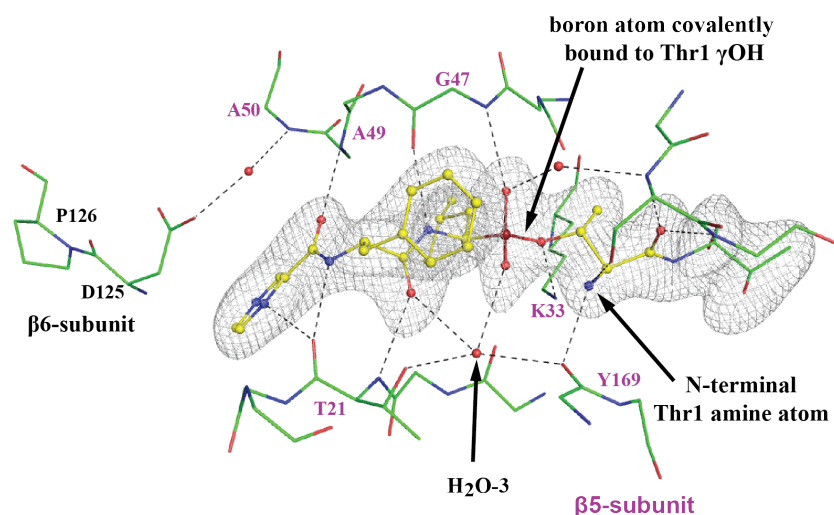


Figure 4.4: Critical interactions of Bortezomib in the active site of human 20S proteasomes. Proposed interactions of boronic acid inhibitors in the human 20S proteasome catalytic site. The boron atom is covalently linked to the Thr1 O_γ. Gly47N and H₂O-3 stabilize the tetrahedral boronate adduct with hydrogen-bridges. No hydrogen bond formation between the N-terminal Thr1 amine atom and the acidic boronate hydroxyl moiety could be visualized.

4.4 Structural Impact of 20S Inhibitors on the 26S Holoenzyme

Knowledge about the structural impact of core particle inhibitors on the human 26S proteasome holoenzyme might provide insight into the proteasome's mechanism of operation. Furthermore, this might serve as a platform for inhibitor screening and the development of future proteasome inhibitors.

The capacity of the proteasome to degrade proteins substantially depends on the core particle-regulatory particle interaction. It was previously shown that proteasome inhibitors are potent in proteasome stabilization¹⁴⁵. In 2007, Finley and colleagues could show by *in vitro* reconstitution assays that epoxyketone and boronic acid inhibitors stabilize the CP-RP interaction. These findings suggested that core particle inhibition is communicated to the interface between core particle and regulatory particle. They envisioned that proteasome inhibition is carried out by an allosteric mechanism. The flow of information is directed from the active site deep in the 20S proteasome towards the regulatory particle¹⁴⁵.

Allosteric regulation was later discovered in the yeast and mouse 20S proteasome¹⁵⁷. Conformational changes in the protease become visible upon peptidic ligand binding at the $\beta 5$ active site. Comparison of all 28 subunits of the unliganded 20S proteasome with a peptide-20S proteasome complex demonstrated an enhanced plasticity of the $\beta 5$ subunit. This suggests specific signaling pathways to other subunits. The tight packing of the subunits in the CP together with the observed conformational changes opened the possibility of signal propagation from $\beta 5$ to other subunits. Most of the conformational alterations in the $\beta 5$ subunit induced by the peptidic binding were observed distant from the active site's Thr1 and located at the surface of the 20S proteasome. In yeast 20S proteasomes, the binding of a peptidic ligand causes domain closure and movements of about 1 Å¹⁵⁷. Still, communication between the 20S core particle and the 19S regulatory particle is unexpected because of the large distance, but movement in the subunits of the 20S core particle seems to propagate towards the surface of the 19S regulatory particle. In the yeast 26S proteasome different conformations were previously observed in electron cryomicroscopic studies. Under native *in vitro* conditions approximately 80 % of the yeast proteasome particles were found in the relaxed, non-rotated conformational state (Figure 4.5)^{158,51}. Binding of a slowly degraded substrate to the regulatory particle¹⁵⁸ or treatment with the slowly-hydrolyzable nucleotide ATP γ S has a direct effect on the conformational state of the 26S proteasome. The rotated conformational state is then favored over the non-rotated state by 55 % and 73 %, respectively (Figure 4.5)⁵¹. Sledz et al. proposed that the yeast 26S proteasome switches to a actively translocating state upon substrate degradation: The AAA+ ATPase becomes coaxially aligned to the core

particle pore, the ubiquitin receptor Rpn10 contacts the Rpt4-Rpt5 coiled coil and the DUB Rpn11 shifts to a central position directly above the N-ring pore of the AAA+ ATPase. These structural rearrangements are similar to the 26S proteasome particles found in the rotated state in the presence of ATP γ S.

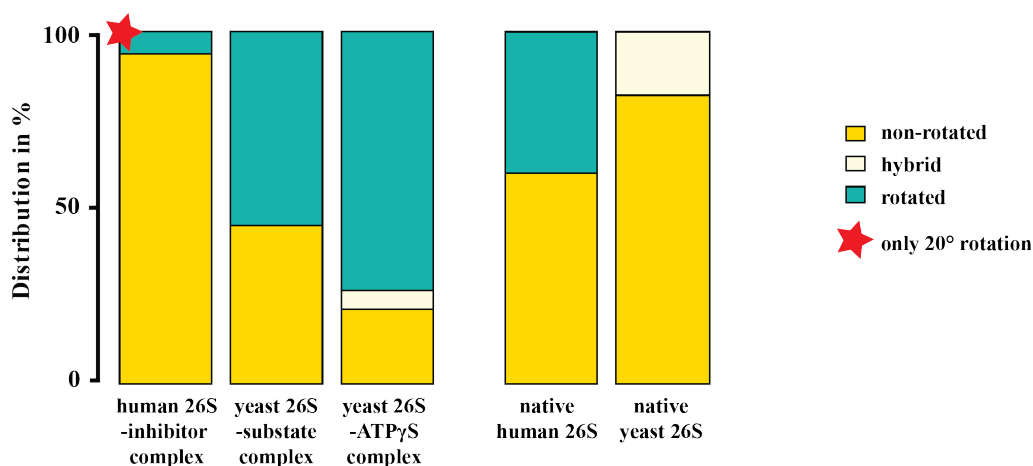


Figure 4.5: Relative frequencies of non-rotated, hybrid and rotated state. Comparison of relative frequencies of the three conformational states of the regulatory particle. Left to right: Human 26S proteasomes in complex with Oprozomib, yeast 26S proteasomes with substrate bound to the 19S subunit, yeast 26S proteasomes in presence of ATP γ S, native human 26S proteasomes, native yeast proteasomes^{51,158}. Human 26S proteasomes inhibited by Oprozomib are predominantly found in the non-rotated state (94 %). The remaining particles are found in a rotated state, whereby the main lid rotation is limited to 20°.

When Finley and colleagues formulated the first hypothesis about allosteric regulation of the 26S proteasome by 20S inhibitors they did not have the possibilities to investigate this structurally. We are now able to determine structures of the 26S proteasome holoenzyme with and without epoxyketone inhibitors by single particle cryo-EM.

We identified a clear restriction of the conformational landscape of the human 26S proteasome upon inhibitor treatment, while the overall conformation of the non-inhibited and inhibited form is identical. Previous studies showed that treatment of 26S proteasomes with 20S proteasome inhibitors leads to a stabilization of polyubiquitinated substrates¹⁴⁷. We found no evidence for a profound accumulation of polyubiquitinated substrates in the inhibited sample by western blot analysis. With this we could exclude that the structural differences derive from polyubiquitinated substrates attached to the 26S proteasome.

We proceeded then to analyze the Oprozomib-inhibited and the non-inhibited 26S proteasome by cryo-EM. This resulted in a final map of the Oprozomib-inhibited human 26S proteasome at a resolution of 3.8 Å and the non-inhibited at 4.8 Å. We found that inhibitor binding induces an energy barrier minimizing the possibility of the regulatory particle to rotate on the core particle. This is reflected by the higher resolution structure of the Oprozomib-inhibited 26S proteasome compared to the non-inhibited structure. 12 % of all particles of the Oprozomib dataset contributed to the high resolution Oprozomib-

26S proteasome complex. Only 4 % of all particles of the native dataset are found in the lower resolution reconstruction of the non-inhibited 26S proteasome.

Inhibition of the human 26S proteasome by 20S core particle inhibitors leads to a stabilization of the proteasome holoenzyme in the non-rotated state (Figure 4.5). Thus, inhibitor binding in the core particle of the holoenzyme shows a distinct opposing effect on the conformational landscape than substrate binding to the regulatory particle or blockage of the AAA+ ATPase. Regulation of the conformational motion seems to occur from two directions: the 19S regulatory particle or the 20S core particle, resulting in opposing conformational states. In Figure 4.5 the relative frequencies of all previously described prominent conformational states in different proteasome preparations are shown. The native yeast conformation distribution differs from the native human distribution. In yeast, most particles are found in the non-rotated state (82 %) and the remaining particles are found in a hybrid state (S2). Native human 26S proteasomes have an almost even distribution between non-rotated and rotated states (60 % to 40 %).

The same trend was observed from *in situ* studies of mammalian hippocampal neurons¹⁵⁹. 80 % of the 26S proteasome found in the cell were in the ground state and 20 % in the rotated substrate processing state. This correlates well with the native human 26S proteasome dataset. In addition, we performed 26S proteasome data analysis of three independent proteasome preparations. Classification of the datasets was performed carefully and in an exemplary way to allow for statistical analysis.

In conclusion, our data show that 20S core particle inhibition shifts the 26S particle distribution towards the non-rotated state. In contrast, 26S proteasomes in complex with substrates in the 19S regulatory particle or in the presence of ATP γ S have a higher fraction of particles in the rotated conformational state. This points to the fact that the 26S proteasome can be manipulated at various sites and we propose a bi-directional signaling pathway throughout the 26S proteasome. This is presented and discussed in the following section.

4.5 A Potential bi-directional Signaling Pathway

Electron cryomicroscopic analysis of inhibited human 26S proteasomes provides evidence that inhibition of the 20S proteasome allosterically regulates the conformation of the holoenzyme. The inhibitor bound to the proteolytic site in the core particle has the possibility to send a signal to the regulatory particle which is converted and amplified into structural changes. Earlier studies presented a similar allosteric effect mediated from the regulatory particle towards the 20S core particle.

To address the question of which determinants might be involved in the long-range communication throughout the proteasome holoenzyme, a detailed investigation of the dynamics of distinct parts of the proteasome was carried out. Two important and correlated criteria to investigate conformational mobility were taken into account: decreased local resolutions in the EM map and regions with high B-factors in the atomic model.

The chemical signal of inhibition is located in the $\beta 5$ subunit of the 20S core particle and is propagated towards the outer parts of the regulatory particle. Starting from the site of inhibition, a hypothesis for propagation of signals throughout the holoenzyme is presented.

The α -ring

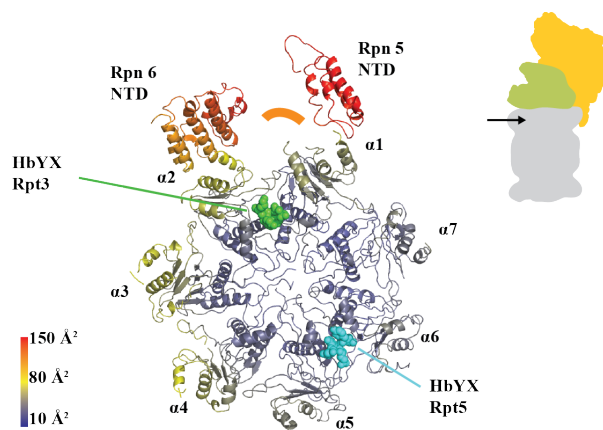
The upper α -ring is located between the inhibitor binding site and regulatory particle. This α -ring serves as a platform for regulatory particle binding to the 20S core particle. A gradient of flexibility within the α -ring becomes visible. A significant increase in B-factors was found on the outer parts of the α -ring subunits $\alpha 2$, $\alpha 3$ and $\alpha 4$, as shown in Figure 4.6. These subunits are located above the Oprozomib binding site in the $\beta 5$ subunit.

The asymmetric B-factor elevation of the α -ring might directly be relayed to the regulatory particle subunits Rpn5 and Rpn6. The N-termini of Rpn5 and Rpn6 are extended towards the $\alpha 1$ and $\alpha 2$ subunits of the 20S particle. The atomic model of these N-terminal domains revealed high B-factors (Figure 4.6). A direct lateral transmission of the inhibitory signal onto the regulatory particle Rpn5 and Rpn6 subunits is possible according to these data.

The AAA+ ATPase

The next area which shows conformational mobility is the next higher level in vertical transmission: the AAA+ ATPase. The AAA+ ATPase is part of the 19S regulatory particle and connects the core particle with the regulatory particle through binding of

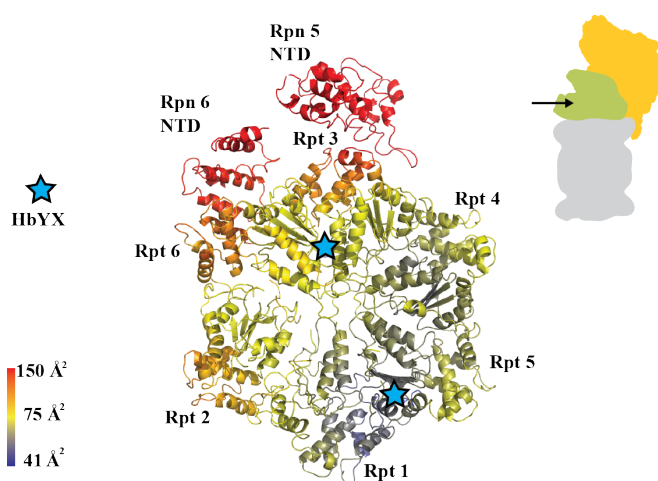
Figure 4.6: B-factors of the upper α -ring. Model of the α -ring together with the 19S subunit N-terminal domains of Rpn5 and Rpn6. Colored according to the B-factors. The HbXY motifs of Rpt3 and Rpt5 (green and cyan ball-and-stick model) are bound in the corresponding binding pockets. The orange arc line depicts the position of Rpt3 which shows the highest B-factor.



N-terminal tails of the HbXY motifs into the binding pockets of the α -ring. The motifs of AAA+ ATPase subunits Rpt3 and Rpt5 are bound to their corresponding binding pockets in the core particle (Figure 4.6). The density for the HbXY motif of Rpt2 is missing, indicating that the HbXY motif remains flexible. The AAA+ ATPase model with coloring according to the B-factors is shown in Figure 4.7. The subunits Rpt2, Rpt3 and Rpt6 show an increased mobility, represented by high B-factor values. These subunits are in close proximity to the highly flexible Rpn5 and Rpn6 N-terminal domains. Rpt2 is most proximal to the CP in the staircase arrangement of the ATPase. The unbound and flexible HbXY motif of Rpt2 might facilitate AAA+ ATPase motion on the 20S core particle.

The high flexibility on one side of the α -ring is propagated to the AAA+ ATPase subunits. The flexible parts are in close proximity to the N-terminal domains of Rpn5 and Rpn6 in both cases.

Figure 4.7: B-factors of the AAA+ ATPase. Model of the AAA+ ATPase together with the 19S subunit N-terminal domains of Rpn5 and Rpn6. Colored according to the B-factors. The B-factors increase towards the AAA+ ATPase parts which are adjacent to the N-terminal domains of Rpn5 and Rpn6. For better orientation, the position of the HbXY domains is indicated by blue asterisks.



The symmetry of the dynamic AAA+ ATPase was also investigated. The AAA+ ATPase rings deviate from a sixfold pseudosymmetry and the subunits are arranged in a helical staircase structure³¹. For analysis, three conserved amino acids from all six ATPase subunits were chosen as anchor points. These amino acids are found in (a) the C-terminal region, (b) the middle part of the ATPase, and, (c) the N-terminal region near the center

of the AAA+ ATPase. When connecting the $C\alpha$ -atoms of the conserved amino acids next to each other the resulting hexagon gives evidence of the angle of the symmetry of the AAA+ ATPase. In Figure 4.8 the exact angles for the subunit Rpt2 are given. The C-terminal region is arranged in a perfect hexagon with an angle of 120° . The symmetry is distorted when measuring the N-terminal regions near the center of the AAA+ ATPase. The angle measured for Rpt2 is decreased to 99° , indicating a vertical deviation from perfect six-fold symmetry. This is even visible in different sugar conformations of the bound nucleotide in subunit Rpt2 (Figure 4.9). The only nucleotide showing a different sugar pucker conformation is Rpt2. This might indicate major conformational changes in the areas around or the exchange to a different nucleotide in that particular position.

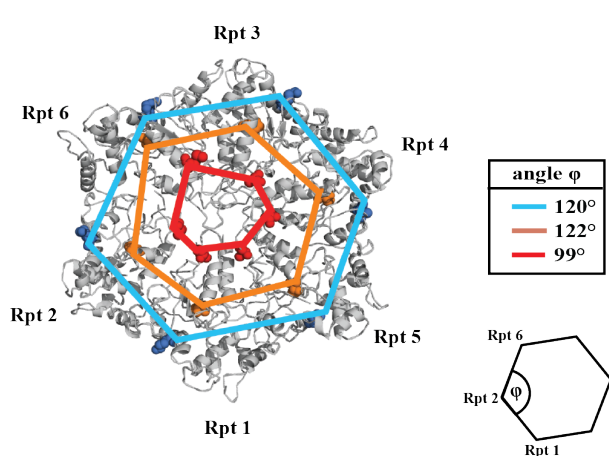


Figure 4.8: Deviation from perfect six-fold symmetry in the ATPase. The conserved amino acids are depicted in ball-and-stick representation. Hexagons were created by linking the aminoacids of the neighboring subunits. The C-terminal (outer) parts of the ATPase form a perfect hexagon. Moving towards the N-terminal region the hexagon becomes distorted.

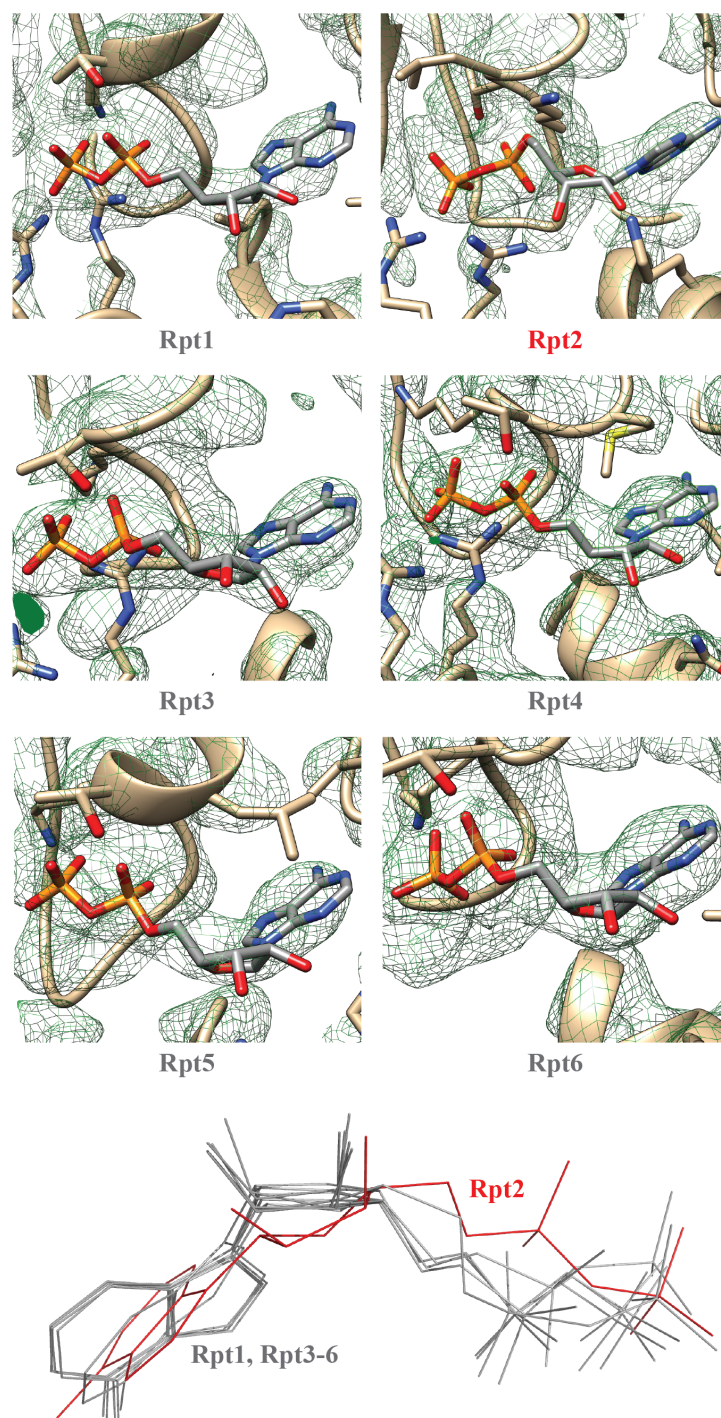


Figure 4.9: Different sugar conformation of nucleotide Rpt2. Close-up view of all six nucleotide densities in the AAA+ ATPase of the human Oprozomib-26S proteasome complex. All nucleotides were built as ADP. Due to low resolution we could not distinguish between ADP and ATP nucleotides. The nucleotide bound to Rpt2 shows a different sugar pucker (bottom).

Rpn10 Domain Dynamics

By focused classification on the ubiquitin receptor, Rpn10, a multitude of different conformations were found in the next higher level in vertical transmission. Figure 4.10 shows exemplary conformations of the highly flexible ubiquitin receptor, Rpn10. The receptor is located in the periphery of the regulatory particle above the ATPase domain and is in close proximity to Rpn5. The classification revealed conformers of Rpn10 in direct contact with the coiled-coil regions of the AAA+ ATPase domains Rpt4 and Rpt5. Other conformers of Rpn10 are completely detached from the adjacent subunit, the deubiquitinase Rpn8.

The proteasome subunit Rpn5 spans a distance of 100 Å from the 20S core particle passing the ATPase towards the ubiquitin receptor Rpn10. This makes Rpn5 a likely candidate to be involved in the propagation of the inhibitory signal from the active site in the core particle to the substrate receptor in the regulatory particles. Rpn5 is an essential lid protein, as described for yeast and plants¹⁶⁰.

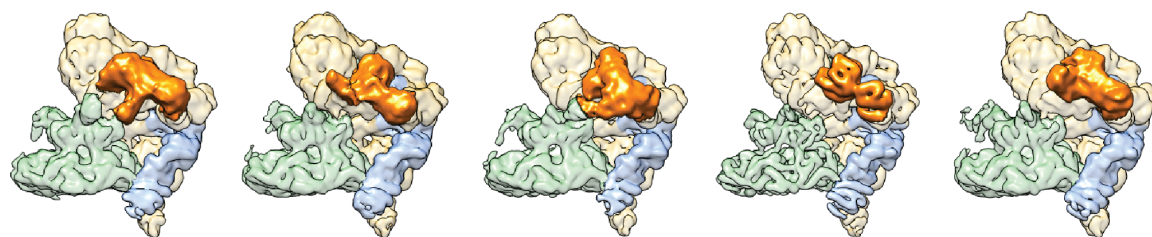


Figure 4.10: Conformational states of the Rpn10 protein. Focused classification on the ubiquitin receptor Rpn10 (orange) revealed a multiple conformational states. Exemplary conformational states are shown. The Rpn5 domain is colored in blue.

In conclusion, all sites of the 26S proteasome that are in direct contact or in close proximity to Rpn5 show a high degree of flexibility and harbor the most mobile regions in the atomic model: The signal might be transmitted by Rpn5 from the site of inhibition in the core particle to the α -subunit and the adjacent AAA+ ATPase and come to a final stage by effecting the receptors of the regulatory particle. In general, the signal transmission seems to make it's way from deep in the barrel shaped 20S core particle to the surface of the 19S regulatory particle.

Chapter 5

Conclusion and Outlook

This work furthers the understanding of proteasome inhibition in the human 20S proteasome and gives first insights into structural influences of 20S core particle inhibition on the 26S holoenzyme.

Firstly, a general workflow to gently purify endogenous human proteasome was established. High resolution crystal structures of the native human 20S proteasome and in complex with cancer therapeutics were analyzed. The native human 20S proteasome structure was determined at 1.8 Å resolution. This is the highest resolution yet attained for any proteasome structure. Collectively, the structures provide detailed insights into the active site and catalytic mechanisms of inhibition of the 20S proteasome. The map details reveal substantial differences calling for a revised descriptions of the proteasomal active site. Co-crystal structures with inhibitors enabled the direct observation of novel inhibition mechanism that distinctly differ from earlier models derived from lower resolution maps.

The inhibition mechanisms will guide the design of next-generation proteasome-based cancer therapeutics. Our results suggest that peptide based inhibitors with dual-electrophile head groups would exhibit kinetically improved inhibition rates. With the workflow presented, we have a powerful and robust tool to structurally analyze hundreds of potential cancer therapeutics in complex with the human 20S proteasome in a short time.

In the second part of this thesis, the effect of core particle inhibition on the human 26S holoenzyme was analyzed by single particle cryo-EM. Since the human 26S holoenzyme is an attractive target for the development of chemotherapeutics, the structure of the human 26S proteasome in complex with the 20S core particle inhibitor, Oprozomib was determined. We found that inhibitor binding modifies the conformational dynamics of the 19S regulatory particle resulting in a stabilization of a non-productive state of the 26S holoenzyme. We propose a mediation of the chemical drug-binding signal into structural changes over a distance of more than 150 Å. Furthermore, we present evidence that the regulatory particle subunit, Rpn5 most likely conveys the information from the catalytic center over this long-range distance. An allosteric effector that has such an extended reach was never described before. From previous publications it was known that substrate bind-

ing to the regulatory particle also results in structural changes in the 26S holoenzyme. Ligand binding to the regulatory particle has the opposing effect on the conformational landscape of the 26S proteasome than ligand binding to the core particle. These findings indicate a bi-directional signaling pathway, mediated by a feedback regulation through regulatory particle subunit Rpn5. This knowledge allows a foresight: Core particle inhibitors with novel inhibition chemistry and inhibitors that target the regulatory particle might have a profound influence on the conformational variability and activity of the 26S proteasome. Furthermore, the inhibitory signal is communicated to the surface of the 26S proteasome and detectable by structural methods.

A detailed knowledge of the inhibition chemistry in the proteolytic site combined with a direct visualization of changes in the conformational dynamics in the 26S holoenzyme upon drug binding will allow for future drug design and drug screening. Still, better resolved structures of the 26S proteasome are needed to identify all determinants that are involved in the long-range communication.

Appendix A

Declaration of contribution as co-author

The inhibition mechanism of human 20S proteasomes enables next-generation inhibitor design

Schrader J, Henneberg F, Mata RA, Tittmann K, Schneider TR, Stark H, Bourenkov G, Chari A: **Science**, 353 (6299): 594-598

Thesis author's contributions

Conception:	20 %
Experimental contribution:	20 %
Formulation of results:	10 %

Long-range allosteric regulation of the human 26S proteasome by 20S proteasome-targeting cancer drugs

Haselbach D, Schrader J, Lambrecht F, Henneberg F, Chari A, Stark H: **Nat. Commun.**, 8: 15578

Thesis author's contributions

Conception:	20 %
Experimental contribution:	20 %
Formulation of results:	10 %

Appendix B

Abbreviations

2D two-dimensional

3D three-dimensional

Å Ångström

AAA+ ATPases Associated with diverse cellular Activities

Arg Arginine

Asp Aspartic acid

ATP Adenosine triphosphate

Blm10 bleomycin-sensitive 10

Br/Br⁻ Bromine/Bromide

BS3 Bis(sulfosuccinimidyl)suberat

B. stearothermophilus *Bacillus stearothermophilus*

CCD Charge Coupled Device

Cdc48 Cell division cycle 48

CP Core Particle (20S proteasome)

cryo-EM cryogenic electron microscopy/ electron cryomicroscopy

CTF Contrast Transfer Function

DDi1 DNA damage-inducible 1

DNA Desoxy-Ribonucleic Acid

Dsk2 dominant suppressor of Kar2

DTT Dithiothreitol

DUB Deubiquinating enzyme

E1 Ubiquitin-activating enzyme

- E2** Ubiquitin-conjugating enzyme
- E3** Ubiquitin-ligase
- E3BP** E3-binding protein
- EM** Electron Microscopy
- EMDB** Electron Microscopy Data Bank
- FDA** Food and Drug Administration
- FSC** Fourier shell correlation
- Glu** Glutamic acid
- Gly** Glycine
- GraFix** Gradient Fixation
- HbYX** hydrophobic, tyrosine, any amino acid tripeptide
- HECT** Homologous to the E6AP Carboxyl Terminus
- HeLa** cell line, Henrietta Lacks
- Hul5** HECT ubiquitin ligase 5
- IDP** Intrinsically disordered proteins
- I κ B** NF-kappa-B inhibitor
- Ile** Isoleucine
- K** Lysine
- kDa** kiloDalton
- keV** kiloelectron volt
- Lys** Lysine
- IN₂** liquid nitrogen
- MAD** Multiple Anomalous Dispersion
- Mg** Magnesium
- MGy** Megagray
- MIR** Multiple Isomorphous Replacement
- Mn** Manganese
- MPN** Mpr1/Pad1 N-terminal

N Nitrogen

Nf- α B nuclear factor of α B

NMA Normal Mode Analysis

NTD N-terminal domain

Ntn N-terminal nucleophile

O Oxygen

PA Proteasome Activator

PAN Proteasome-Activating Nucleotidase

PC Proteasome/Cyclosome repeats

PCI Proteasome-CSN-eIF3

PCA principal component analysis

PDB Protein Data Bank

PRU Pleckstrin-like Receptor for Ubiquitin

Rad23 Radiation Sensitive 23

RING Really Interesting New Gene

RP Regulatory Particle (19S subunit)

Rpn Regulatory particle non-ATPase

Rpt Regulatory particle tripleA-ATPase

SAD Single Anomalous Dispersion

S. cerevisiae *Saccharomyces cerevisiae*

SIR Single Isomorphous Replacement

SDS-PAGE Sodium Dodecyl Sulfate- Poly-Acrylamide Gel Electrophoresis

Ser Serine

SNR Signal-to-Noise-Ratio

T. acidophilum *Thermoplasma acidophilum*

Thr Threonine

TEM Transmission Electron Microscope

T. thermophilus *Thermus thermophilus*

Ub Ubiquitin

UBA Ubiquitin-Associated

UBL Ubiquitin-Like

Ubp Ubiquitin-specific protease

UIM Ubiquitin-Interacting Motif

UPS Ubiquitin-Proteasome-System

USP Ubiquitin-Specific Protease

VCP Valosin-Containing Protein

vWA von Willebrand factor type A

Bibliography

- [1] T.-W. Mu, D. S. T. Ong, Y.-J. Wang, W. E. Balch, J. R. Yates, L. Segatori, and J. W. Kelly, “Chemical and Biological Approaches Synergize to Ameliorate Protein-Folding Diseases,” *Cell*, vol. 134, no. 5, pp. 769–781, 2008.
- [2] E. Cohen, J. F. Paulsson, P. Blinder, T. Burstyn-Cohen, D. Du, G. Estepa, A. Adame, H. M. Pham, M. Holzenberger, J. W. Kelly, E. Masliah, and A. Dillin, “Reduced IGF-1 Signaling Delays Age-Associated Proteotoxicity in Mice,” *Cell*, vol. 139, no. 6, pp. 1157–1169, dec 2009.
- [3] M. H. Glickman and A. Ciechanover, “The Ubiquitin-Proteasome Proteolytic Pathway: Destruction for the Sake of Construction,” *Physiological Reviews*, vol. 82, no. 2, pp. 373–428, apr 2002.
- [4] K. L. Rock, C. Gramm, L. Rothstein, K. Clark, R. Stein, L. Dick, D. Hwang, and A. L. Goldberg, “Inhibitors of the proteasome block the degradation of most cell proteins and the generation of peptides presented on MHC class I molecules.” *Cell*, vol. 78, no. 5, pp. 761–71, sep 1994.
- [5] D. Finley, “Recognition and processing of ubiquitin-protein conjugates by the proteasome.” *Annual review of biochemistry*, vol. 78, pp. 477–513, jan 2009.
- [6] O. Coux, K. Tanaka, and A. L. Goldberg, “Structure and Functions of the 20S and 26S Proteasomes,” *Annual Review of Biochemistry*, vol. 65, no. 1, pp. 801–847, jun 1996.
- [7] C. M. Pickart and R. E. Cohen, “Proteasomes and their kin: proteases in the machine age,” *Nature Reviews Molecular Cell Biology*, vol. 5, no. 3, pp. 177–187, mar 2004.
- [8] V. Chau, J. Tobias, A. Bachmair, D. Marriott, D. Ecker, D. Gonda, and A. Varshavsky, “A multiubiquitin chain is confined to specific lysine in a targeted short-lived protein,” *Science*, vol. 243, no. 4898, pp. 1576–1583, mar 1989.
- [9] J. S. Thrower, L. Hoffman, M. Rechsteiner, and C. M. Pickart, “Recognition of the polyubiquitin proteolytic signal.” *The EMBO journal*, vol. 19, no. 1, pp. 94–102, jan 2000.

- [10] A. Hershko, H. Heller, E. Eytan, and Y. Reiss, "The protein substrate binding site of the ubiquitin-protein ligase system." *The Journal of biological chemistry*, vol. 261, no. 26, pp. 11 992–9, sep 1986.
- [11] K. D. Wilkinson, "Regulation of ubiquitin-dependent processes by deubiquitinating enzymes." *FASEB journal : official publication of the Federation of American Societies for Experimental Biology*, vol. 11, no. 14, pp. 1245–56, dec 1997.
- [12] C. M. Pickart and I. A. Rose, "Ubiquitin carboxyl-terminal hydrolase acts on ubiquitin carboxyl-terminal amides." *The Journal of biological chemistry*, vol. 260, no. 13, pp. 7903–10, jul 1985.
- [13] J. M. Huibregtse, M. Scheffner, S. Beaudenon, and P. M. Howley, "A family of proteins structurally and functionally related to the E6-AP ubiquitin-protein ligase." *Proceedings of the National Academy of Sciences of the United States of America*, vol. 92, no. 7, pp. 2563–7, mar 1995.
- [14] K. L. Lorick, J. P. Jensen, S. Fang, A. M. Ong, S. Hatakeyama, and A. M. Weissman, "RING fingers mediate ubiquitin-conjugating enzyme (E2)-dependent ubiquitination." *Proceedings of the National Academy of Sciences of the United States of America*, vol. 96, no. 20, pp. 11 364–9, sep 1999.
- [15] T. Ravid and M. Hochstrasser, "Diversity of degradation signals in the ubiquitin-proteasome system," *Nature Reviews Molecular Cell Biology*, vol. 9, no. 9, pp. 679–689, sep 2008.
- [16] M. Groll, L. Ditzel, J. Löwe, D. Stock, M. Bochtler, H. D. Bartunik, and R. Huber, "Structure of 20S proteasome from yeast at 2.4 Å resolution." *Nature*, vol. 386, no. 6624, pp. 463–71, apr 1997.
- [17] M. Groll, M. H. Glickman, D. Finley, M. Bajorek, A. Köhler, L. Moroder, D. M. Rubin, and R. Huber, "A gated channel into the proteasome core particle," *Nature Structural Biology*, vol. 7, no. 11, pp. 1062–1067, nov 2000.
- [18] F. Kriegenburg, E. G. Poulsen, A. Koch, E. Krüger, and R. Hartmann-Petersen, "Redox Control of the Ubiquitin-Proteasome System: From Molecular Mechanisms to Functional Significance," *Antioxidants & Redox Signaling*, vol. 15, no. 8, pp. 2265–2299, oct 2011.
- [19] M. Orłowski and C. Michaud, "Pituitary multicatalytic proteinase complex. Specificity of components and aspects of proteolytic activity," *Biochemistry*, vol. 28, no. 24, pp. 9270–9278, nov 1989.
- [20] A. K. Nussbaum, T. P. Dick, W. Keilholz, M. Schirle, S. Stevanović, K. Dietz, W. Heinemeyer, M. Groll, D. H. Wolf, R. Huber, H. G. Rammensee, and H. Schild,

- “Cleavage motifs of the yeast 20S proteasome beta subunits deduced from digests of enolase 1.” *Proceedings of the National Academy of Sciences of the United States of America*, vol. 95, no. 21, pp. 12 504–9, oct 1998.
- [21] I. Schechter and A. Berger, “On the size of the active site in proteases. I. Papain,” *Biochemical and Biophysical Research Communications*, vol. 27, no. 2, pp. 157–162, apr 1967.
- [22] E. M. Huber, M. Basler, R. Schwab, W. Heinemeyer, C. J. Kirk, M. Groettrup, and M. Groll, “Immuno- and constitutive proteasome crystal structures reveal differences in substrate and inhibitor specificity.” *Cell*, vol. 148, no. 4, pp. 727–38, feb 2012.
- [23] M. Unno, T. Mizushima, Y. Morimoto, Y. Tomisugi, K. Tanaka, N. Yasuoka, and T. Tsukihara, “The Structure of the Mammalian 20S Proteasome at 2.75 Å Resolution,” *Structure*, vol. 10, no. 5, pp. 609–618, may 2002.
- [24] J. Löwe, D. Stock, B. Jap, P. Zwickl, W. Baumeister, and R. Huber, “Crystal structure of the 20S proteasome from the archaeon *T. acidophilum* at 3.4 Å resolution.” *Science*, vol. 268, no. 5210, pp. 533–9, apr 1995.
- [25] W. Harshbarger, C. Miller, C. Diedrich, and J. Sacchettini, “Crystal structure of the human 20S proteasome in complex with carfilzomib.” *Structure*, vol. 23, no. 2, pp. 418–24, feb 2015.
- [26] E. Seemüller, A. Lupas, D. Stock, J. Löwe, R. Huber, and W. Baumeister, “Proteasome from *Thermoplasma acidophilum*: a threonine protease.” *Science*, vol. 268, no. 5210, pp. 579–82, apr 1995.
- [27] A. Martin, T. A. Baker, and R. T. Sauer, “Rebuilt AAA + motors reveal operating principles for ATP-fuelled machines.” *Nature*, vol. 437, no. 7062, pp. 1115–20, oct 2005.
- [28] R. J. Tomko, M. Funakoshi, K. Schneider, J. Wang, M. Hochstrasser, and M. Hochstrasser, “Heterohexameric ring arrangement of the eukaryotic proteasomal ATPases: implications for proteasome structure and assembly.” *Molecular cell*, vol. 38, no. 3, pp. 393–403, may 2010.
- [29] K. Hofmann and P. Bucher, “The PCI domain: a common theme in three multiprotein complexes,” *Trends in Biochemical Sciences*, vol. 23, no. 6, pp. 204–205, jun 1998.
- [30] K. Paraskevopoulos, F. Kriegenburg, M. H. Tatham, H. I. Rösner, B. Medina, I. B. Larsen, R. Brandstrup, K. G. Hardwick, R. T. Hay, B. B. Kragelund, R. Hartmann-

- Petersen, and C. Gordon, "Dss1 is a 26S proteasome ubiquitin receptor." *Molecular cell*, vol. 56, no. 3, pp. 453–61, nov 2014.
- [31] G. C. Lander, E. Estrin, M. E. Matyskiela, C. Bashore, E. Nogales, and A. Martin, "Complete subunit architecture of the proteasome regulatory particle," *Nature*, vol. 482, jan 2012.
- [32] R. Verma, L. Aravind, R. Oania, W. H. McDonald, J. R. Yates, E. V. Koonin, and R. J. Deshaies, "Role of Rpn11 metalloprotease in deubiquitination and degradation by the 26S proteasome." *Science*, vol. 298, no. 5593, pp. 611–5, oct 2002.
- [33] M. Schmidt, J. Hanna, S. Elsasser, and D. Finley, "Proteasome-associated proteins: regulation of a proteolytic machine," *Biological Chemistry*, vol. 386, no. 8, pp. 725–737, jan 2005.
- [34] R. Verma, R. Oania, J. Graumann, and R. J. Deshaies, "Multiubiquitin Chain Receptors Define a Layer of Substrate Selectivity in the Ubiquitin-Proteasome System," *Cell*, vol. 118, no. 1, pp. 99–110, jul 2004.
- [35] D. S. Leggett, J. Hanna, A. Borodovsky, B. Crosas, M. Schmidt, R. T. Baker, T. Walz, H. Ploegh, and D. Finley, "Multiple Associated Proteins Regulate Proteasome Structure and Function," *Molecular Cell*, vol. 10, no. 3, pp. 495–507, sep 2002.
- [36] J. You and C. M. Pickart, "A HECT domain E3 enzyme assembles novel polyubiquitin chains." *The Journal of biological chemistry*, vol. 276, no. 23, pp. 19 871–8, jun 2001.
- [37] D. M. Smith, S.-C. Chang, S. Park, D. Finley, Y. Cheng, and A. L. Goldberg, "Docking of the proteasomal ATPases' carboxyl termini in the 20S proteasome's alpha ring opens the gate for substrate entry." *Molecular cell*, vol. 27, no. 5, pp. 731–44, sep 2007.
- [38] G. Tian, S. Park, M. J. Lee, B. Huck, F. McAllister, C. P. Hill, S. P. Gygi, and D. Finley, "An asymmetric interface between the regulatory and core particles of the proteasome." *Nature structural & molecular biology*, vol. 18, no. 11, pp. 1259–67, oct 2011.
- [39] B. M. Stadtmueller and C. P. Hill, "Proteasome activators." *Molecular cell*, vol. 41, no. 1, pp. 8–19, jan 2011.
- [40] D. Barthelme and R. T. Sauer, "Identification of the Cdc48/20S proteasome as an ancient AAA+ proteolytic machine." *Science*, vol. 337, no. 6096, pp. 843–6, aug 2012.

- [41] D. Barthelme and R. T. Sauer, “Bipartite determinants mediate an evolutionarily conserved interaction between Cdc48 and the 20S peptidase.” *Proceedings of the National Academy of Sciences of the United States of America*, vol. 110, no. 9, pp. 3327–32, feb 2013.
- [42] S. Bohn, F. Beck, E. Sakata, T. Walzthoeni, M. Beck, R. Aebersold, F. Förster, W. Baumeister, and S. Nickell, “Structure of the 26S proteasome from *Schizosaccharomyces pombe* at subnanometer resolution.” *Proceedings of the National Academy of Sciences of the United States of America*, vol. 107, no. 49, pp. 20 992–7, dec 2010.
- [43] K. Lasker, F. Förster, S. Bohn, T. Walzthoeni, E. Villa, P. Unverdorben, F. Beck, R. Aebersold, A. Sali, and W. Baumeister, “Molecular architecture of the 26S proteasome holocomplex determined by an integrative approach.” *Proceedings of the National Academy of Sciences of the United States of America*, vol. 109, no. 5, pp. 1380–7, jan 2012.
- [44] P. C. A. da Fonseca, J. He, and E. P. Morris, “Molecular model of the human 26S proteasome.” *Molecular cell*, vol. 46, no. 1, pp. 54–66, apr 2012.
- [45] F. Beck, P. Unverdorben, S. Bohn, A. Schweitzer, G. Pfeifer, E. Sakata, S. Nickell, J. M. Plitzko, E. Villa, W. Baumeister, and F. Förster, “Near-atomic resolution structural model of the yeast 26S proteasome.” *Proceedings of the National Academy of Sciences of the United States of America*, vol. 109, no. 37, pp. 14 870–5, sep 2012.
- [46] A. Schweitzer, A. Aufderheide, T. Rudack, F. Beck, G. Pfeifer, J. M. Plitzko, E. Sakata, K. Schulten, F. Förster, and W. Baumeister, “Structure of the human 26S proteasome at a resolution of 3.9 Å.” *Proceedings of the National Academy of Sciences of the United States of America*, vol. 113, no. 28, pp. 7816–21, jul 2016.
- [47] X. Huang, B. Luan, J. Wu, and Y. Shi, “An atomic structure of the human 26S proteasome,” *Nature Structural & Molecular Biology*, vol. 23, no. 9, pp. 778–785, jul 2016.
- [48] S. Chen, J. Wu, Y. Lu, Y.-B. Ma, B.-H. Lee, Z. Yu, Q. Ouyang, D. J. Finley, M. W. Kirschner, and Y. Mao, “Structural basis for dynamic regulation of the human 26S proteasome.” *Proceedings of the National Academy of Sciences of the United States of America*, vol. 113, no. 46, pp. 12 991–12 996, nov 2016.
- [49] S. Nickell, F. Beck, S. H. W. Scheres, A. Korinek, F. Förster, K. Lasker, O. Mihalache, N. Sun, I. Nagy, A. Sali, J. M. Plitzko, J.-M. Carazo, M. Mann, and W. Baumeister, “Insights into the molecular architecture of the 26S proteasome.” *Proceedings of the National Academy of Sciences of the United States of America*, vol. 106, no. 29, pp. 11 943–7, jul 2009.

- [50] P. Unverdorben, F. Beck, P. Śledź, A. Schweitzer, G. Pfeifer, J. M. Plitzko, W. Baumeister, and F. Förster, “Deep classification of a large cryo-EM dataset defines the conformational landscape of the 26S proteasome.” *Proceedings of the National Academy of Sciences of the United States of America*, vol. 111, no. 15, pp. 5544–9, apr 2014.
- [51] M. E. Matyskiela, G. C. Lander, and A. Martin, “Conformational switching of the 26S proteasome enables substrate degradation.” *Nature structural & molecular biology*, vol. 20, no. 7, pp. 781–8, jul 2013.
- [52] P. F. Bross, “Approval Summary for Bortezomib for Injection in the Treatment of Multiple Myeloma,” *Clinical Cancer Research*, vol. 10, no. 12, pp. 3954–3964, jun 2004.
- [53] International Myeloma Foundation, “Myeloma.org,” 2017. [Online]. Available: <https://www.myeloma.org/>
- [54] National Library of Medicine, “Clinicaltrials.gov,” 2017. [Online]. Available: <https://clinicaltrials.gov/>
- [55] S. T. Nawrocki, J. S. Carew, M. S. Pino, R. A. Highshaw, K. Dunner, P. Huang, J. L. Abbruzzese, and D. J. McConkey, “Bortezomib sensitizes pancreatic cancer cells to endoplasmic reticulum stress-mediated apoptosis.” *Cancer research*, vol. 65, no. 24, pp. 11 658–66, dec 2005.
- [56] B. An, R. H. Goldfarb, R. Siman, and Q. P. Dou, “Novel dipeptidyl proteasome inhibitors overcome Bcl-2 protective function and selectively accumulate the cyclin-dependent kinase inhibitor p27 and induce apoptosis in transformed, but not normal, human fibroblasts,” *Cell Death and Differentiation*, vol. 5, no. 12, pp. 1062–1075, dec 1998.
- [57] J. Adams, “Proteasome inhibition: a novel approach to cancer therapy,” *Trends in Molecular Medicine*, vol. 8, no. 4, pp. S49–S54, apr 2002.
- [58] H. C. Drexler, “Activation of the cell death program by inhibition of proteasome function.” *Proceedings of the National Academy of Sciences of the United States of America*, vol. 94, no. 3, pp. 855–60, feb 1997.
- [59] P. Masdehors, S. Omura, H. Merle-Beral, F. Mentz, J.-M. Cosset, J. Dumont, H. Magdelenat, and J. Delic, “Increased sensitivity of CLL-derived lymphocytes to apoptotic death activation by the proteasome-specific inhibitor lactacystin,” *British Journal of Haematology*, vol. 105, no. 3, pp. 752–757, jun 1999.

- [60] P. Masdehors, H. Merle-Béral, K. Maloum, S. Omura, H. Magdelénat, and J. Delic, “Deregulation of the ubiquitin system and p53 proteolysis modify the apoptotic response in B-CLL lymphocytes.” *Blood*, vol. 96, no. 1, pp. 269–74, jul 2000.
- [61] A. A. Argyriou, G. Iconomou, and H. P. Kalofonos, “Bortezomib-induced peripheral neuropathy in multiple myeloma: a comprehensive review of the literature,” *Blood*, vol. 112, no. 5, pp. 1593–1599, sep 2008.
- [62] P. G. Richardson, B. Barlogie, J. Berenson, S. Singhal, S. Jagannath, D. Irwin, S. V. Rajkumar, G. Srkalovic, M. Alsina, R. Alexanian, D. Siegel, R. Z. Orlowski, D. Kuter, S. A. Limentani, S. Lee, T. Hideshima, D.-L. Esseltine, M. Kauffman, J. Adams, D. P. Schenkein, and K. C. Anderson, “A Phase 2 Study of Bortezomib in Relapsed, Refractory Myeloma,” *New England Journal of Medicine*, vol. 348, no. 26, pp. 2609–2617, jun 2003.
- [63] P. C. A. da Fonseca and E. P. Morris, “Cryo-EM reveals the conformation of a substrate analogue in the human 20S proteasome core.” *Nature communications*, vol. 6, p. 7573, jan 2015.
- [64] J. Adams, M. Behnke, S. Chen, A. A. Cruickshank, L. R. Dick, L. Grenier, J. M. Klunder, Y.-T. Ma, L. Plamondon, and R. L. Stein, “Potent and selective inhibitors of the proteasome: Dipeptidyl boronic acids,” *Bioorganic & Medicinal Chemistry Letters*, vol. 8, no. 4, pp. 333–338, feb 1998.
- [65] D. Chauhan, Z. Tian, B. Zhou, D. Kuhn, R. Orlowski, N. Raje, P. Richardson, and K. C. Anderson, “In vitro and in vivo selective antitumor activity of a novel orally bioavailable proteasome inhibitor MLN9708 against multiple myeloma cells.” *Clinical cancer research : an official journal of the American Association for Cancer Research*, vol. 17, no. 16, pp. 5311–21, aug 2011.
- [66] E. Kupperman, E. C. Lee, Y. Cao, B. Bannerman, M. Fitzgerald, A. Berger, J. Yu, Y. Yang, P. Hales, F. Bruzzese, J. Liu, J. Blank, K. Garcia, C. Tsu, L. Dick, P. Fleming, L. Yu, M. Manfredi, M. Rolfe, and J. Bolen, “Evaluation of the Proteasome Inhibitor MLN9708 in Preclinical Models of Human Cancer,” *Cancer Research*, vol. 70, no. 5, pp. 1970–1980, mar 2010.
- [67] R. Piva, B. Ruggeri, M. Williams, G. Costa, I. Tamagno, D. Ferrero, V. Gai, M. Coscia, S. Peola, M. Massaia, G. Pezzoni, C. Allievi, N. Pescalli, M. Cassin, S. di Giovine, P. Nicoli, P. de Feudis, I. Streppone, I. Roato, R. Ferracini, B. Bussoleti, G. Camussi, S. Jones-Bolin, K. Hunter, H. Zhao, A. Neri, A. Palumbo, C. Berkers, H. Ovaa, A. Bernareggi, and G. Inghirami, “CEP-18770: A novel, orally active proteasome inhibitor with a tumor-selective pharmacologic profile competitive with bortezomib,” *Blood*, vol. 111, no. 5, pp. 2765–2775, mar 2008.

- [68] J. Adams, "The development of proteasome inhibitors as anticancer drugs." *Cancer cell*, vol. 5, no. 5, pp. 417–21, may 2004.
- [69] M. Altun, P. J. Galardy, R. Shringarpure, T. Hideshima, R. LeBlanc, K. C. Anderson, H. L. Ploegh, and B. M. Kessler, "Effects of PS-341 on the activity and composition of proteasomes in multiple myeloma cells." *Cancer research*, vol. 65, no. 17, pp. 7896–901, sep 2005.
- [70] M. Groll, K. B. Kim, N. Kairies, R. Huber, and C. M. Crews, "Crystal Structure of Epoxomicin:20S Proteasome Reveals a Molecular Basis for Selectivity of α' , β' -Epoxyketone Proteasome Inhibitors," *Journal of the American Chemical Society*, vol. 122, no. 6, pp. 1237–1238, feb 2000.
- [71] S. D. Demo, C. J. Kirk, M. A. Aujay, T. J. Buchholz, M. Dajee, M. N. Ho, J. Jiang, G. J. Laidig, E. R. Lewis, F. Parlati, K. D. Shenk, M. S. Smyth, C. M. Sun, M. K. Vallone, T. M. Woo, C. J. Molineaux, and M. K. Bennett, "Antitumor activity of PR-171, a novel irreversible inhibitor of the proteasome." *Cancer research*, vol. 67, no. 13, pp. 6383–91, jul 2007.
- [72] M. Verdoes, L. I. Willems, W. A. van der Linden, B. A. Duivenvoorden, G. A. van der Marel, B. I. Florea, A. F. Kisselev, and H. S. Overkleeft, "A panel of subunit-selective activity-based proteasome probes." *Organic & biomolecular chemistry*, vol. 8, no. 12, pp. 2719–27, jun 2010.
- [73] M. A. Gräwert, N. Gallastegui, M. Stein, B. Schmidt, P.-M. Kloetzel, R. Huber, and M. Groll, "Elucidation of the α -keto-aldehyde binding mechanism: a lead structure motif for proteasome inhibition." *Angewandte Chemie (International ed. in English)*, vol. 50, no. 2, pp. 542–4, jan 2011.
- [74] S. Imajohohmi, T. Kawaguchi, S. Sugiyama, K. Tanaka, S. Omura, and H. Kikuchi, "Lactacystin, a Specific Inhibitor of the Proteasome, Induces Apoptosis in Human Monoblast U937 Cells," *Biochemical and Biophysical Research Communications*, vol. 217, no. 3, pp. 1070–1077, dec 1995.
- [75] K. Shinohara, M. Tomioka, H. Nakano, S. Toné, H. Ito, and S. Kawashima, "Apoptosis induction resulting from proteasome inhibition." *The Biochemical journal*, pp. 385–8, jul 1996.
- [76] C. Garc a-Echeverr a, P. Imbach, D. France, P. F urst, M. Lang, M. Noorani, D. Scholz, J. Zimmermann, and P. Furet, "A New Structural Class of Selective and Non-covalent Inhibitors of the Chymotrypsin-like Activity of the 20S Proteasome," *Bioorganic & Medicinal Chemistry Letters*, vol. 11, no. 10, pp. 1317–1319, may 2001.

- [77] P. Furet, P. Imbach, M. Noorani, J. Koeppler, K. Laumen, M. Lang, V. Guagnano, P. Fuerst, J. Roesel, J. Zimmermann, and C. García-Echeverría, “Entry into a New Class of Potent Proteasome Inhibitors Having High Antiproliferative Activity by Structure-Based Design,” *Journal of Medicinal Chemistry*, vol. 47, no. 20, pp. 4810–4813, sep 2004.
- [78] B. Villoutreix, M. Reboud-Ravaux, N. Basse, J. Vidal, and M. Montes, “Nitrogen heterocycle derivatives as proteasome modulators,” 2009.
- [79] H. R. Lawrence, S. M. Sebti, and S. Ozcan, “Proteasome chymotrypsin-like inhibition using pi-1833 analogs,” 2012.
- [80] Y. Koguchi, J. Kohno, M. Nishio, K. Takahashi, T. Okuda, T. Ohnuki, and S. Komatsubara, “TMC-95A, B, C, and D, Novel Proteasome Inhibitors Produced by *Apiospora montagnei* Sacc. TC 1093. Taxonomy, Production, Isolation, and Biological Activities.” *The Journal of Antibiotics*, vol. 53, no. 2, pp. 105–109, 2000.
- [81] S. Schoof, G. Pradel, M. Aminake, B. Ellinger, S. Baumann, M. Potowski, Y. Najajreh, M. Kirschner, and H.-D. Arndt, “Antiplasmodial Thiostrepton Derivatives: Proteasome Inhibitors with a Dual Mode of Action,” *Angewandte Chemie International Edition*, vol. 49, no. 19, pp. 3317–3321, apr 2010.
- [82] C. Blackburn, K. M. Gigstad, P. Hales, K. Garcia, M. Jones, F. J. Bruzzese, C. Barrett, J. X. Liu, T. A. Soucy, D. S. Sappal, N. Bump, E. J. Olhava, P. Fleming, L. R. Dick, C. Tsu, M. D. Sintchak, and J. L. Blank, “Characterization of a new series of non-covalent proteasome inhibitors with exquisite potency and selectivity for the 20S β 5-subunit,” *Biochemical Journal*, vol. 430, no. 3, pp. 461–476, sep 2010.
- [83] J. Kohno, Y. Koguchi, M. Nishio, K. Nakao, M. Kuroda, R. Shimizu, T. Ohnuki, and S. Komatsubara, “Structures of TMC-95A-D: Novel Proteasome Inhibitors from *Apiospora montagnei* Sacc. TC 1093,” *The Journal of Organic Chemistry*, vol. 65, 2000.
- [84] M. Groll, Y. Koguchi, R. Huber, and J. Kohno, “Crystal structure of the 20 S proteasome:TMC-95A complex: a non-covalent proteasome inhibitor,” *Journal of Molecular Biology*, vol. 311, no. 3, pp. 543–548, aug 2001.
- [85] B. E. Clurman, R. J. Sheaff, K. Thress, M. Groudine, and J. M. Roberts, “Turnover of cyclin E by the ubiquitin-proteasome pathway is regulated by cdk2 binding and cyclin phosphorylation.” *Genes & development*, vol. 10, no. 16, pp. 1979–90, aug 1996.
- [86] M. Glotzer, A. W. Murray, and M. W. Kirschner, “Cyclin is degraded by the ubiquitin pathway,” *Nature*, vol. 349, no. 6305, pp. 132–138, jan 1991.

- [87] C. Li, R. Dai, and D. Longo, "Inactivation of NF- κ B Inhibitor I κ B α : Ubiquitin-Dependent Proteolysis and Its Degradation Product," *Biochemical and Biophysical Research Communications*, vol. 215, no. 1, pp. 292–301, oct 1995.
- [88] V. J. Palombella, O. J. Rando, A. L. Goldberg, and T. Maniatis, "The ubiquitin-proteasome pathway is required for processing the NF- κ B1 precursor protein and the activation of NF- κ B," *Cell*, vol. 78, no. 5, pp. 773–785, sep 1994.
- [89] D. R. Chowdary, J. J. Dermody, K. K. Jha, and H. L. Ozer, "Accumulation of p53 in a mutant cell line defective in the ubiquitin pathway." *Molecular and cellular biology*, vol. 14, no. 3, pp. 1997–2003, mar 1994.
- [90] M. Ljungman, "Dial 9-1-1 for p53: mechanisms of p53 activation by cellular stress." *Neoplasia*, vol. 2, no. 3, pp. 208–25, 2000.
- [91] J. C. Phillips, A. Wlodawer, M. M. Yevitz, and K. O. Hodgson, "Applications of synchrotron radiation to protein crystallography: preliminary results." *Proceedings of the National Academy of Sciences of the United States of America*, vol. 73, no. 1, pp. 128–32, jan 1976.
- [92] J. C. Kendrew, G. Bodo, H. M. Dintzis, R. G. Parrish, H. Wyckoff, and D. C. Phillips, "A Three-Dimensional Model of the Myoglobin Molecule Obtained by X-Ray Analysis," *Nature*, vol. 181, no. 4610, pp. 662–666, mar 1958.
- [93] M. F. Perutz, M. G. Rossmann, A. F. Cullis, H. Muirhead, G. Will, and A. C. T. North, "Structure of Hæmoglobin: A Three-Dimensional Fourier Synthesis at 5.5-Å. Resolution, Obtained by X-Ray Analysis," *Nature*, vol. 185, no. 4711, pp. 416–422, feb 1960.
- [94] L. Bragg and M. F. Perutz, "The Structure of Haemoglobin." *Proceedings of the Royal Society of London A: Mathematical, Physical and Engineering Sciences*, vol. 225, no. 1162, 1954.
- [95] D. W. Green, V. M. Ingram, and M. F. Perutz, "The Structure of Haemoglobin." *Proceedings of the Royal Society of London A: Mathematical, Physical and Engineering Sciences*, vol. 225, no. 1162, 1954.
- [96] G. Taylor, "The phase problem," *Acta Crystallographica Section D Biological Crystallography*, vol. 59, no. 11, pp. 1881–1890, nov 2003.
- [97] G. Scapin, "Molecular replacement then and now." *Acta crystallographica. Section D, Biological crystallography*, vol. 69, no. Pt 11, pp. 2266–75, nov 2013.

- [98] J. C. Kendrew, G. Bodo, H. M. Dintzis, R. G. Parrish, H. Wyckoff, and D. C. Phillips, "A Three-Dimensional Model of the Myoglobin Molecule Obtained by X-Ray Analysis," *Nature*, vol. 181, no. 4610, pp. 662–666, mar 1958.
- [99] W. A. Hendrickson and M. M. Teeter, "Structure of the hydrophobic protein crambin determined directly from the anomalous scattering of sulphur," *Nature*, vol. 290, no. 5802, pp. 107–113, mar 1981.
- [100] W. Hendrickson, "Determination of macromolecular structures from anomalous diffraction of synchrotron radiation," *Science*, vol. 254, no. 5028, pp. 51–58, oct 1991.
- [101] A. Yonath, J. Missing, B. Tesche, S. Lorenz, V. Erdmann, and H. Wittmann, "Crystallization of the large ribosomal subunit from *Bacillus Stearothermophilus*," *Biochemistry International*, vol. 1, no. 5, pp. 428–435, 1980.
- [102] J. H. Cate, "X-ray Crystal Structures of 70S Ribosome Functional Complexes," *Science*, vol. 285, no. 5436, pp. 2095–2104, sep 1999.
- [103] J. Bernal and D. Crowfoot, "X-Ray Photographs of Crystalline Pepsin," *Nature*, vol. 133, pp. 794–795, 1934.
- [104] B. Heras and J. L. Martin, "Post-crystallization treatments for improving diffraction quality of protein crystals," *Acta Crystallographica Section D Biological Crystallography*, vol. 61, no. 9, pp. 1173–1180, sep 2005.
- [105] M. Knoll and E. Ruska, "Das Elektronenmikroskop," *Zeitschrift für Physik*, vol. 78, no. 5-6, pp. 318–339, may 1932.
- [106] J. Dubochet, J. Lepault, R. Freeman, J. A. Berriman, and J.-C. Homo, "Electron microscopy of frozen water and aqueous solutions," *Journal of Microscopy*, vol. 128, no. 3, pp. 219–237, dec 1982.
- [107] H. Stark, F. Zemlin, and C. Boettcher, "Electron radiation damage to protein crystals of bacteriorhodopsin at different temperatures," *Ultramicroscopy*, vol. 63, no. 2, pp. 75–79, 1996.
- [108] W. Wong, X.-c. Bai, A. Brown, I. S. Fernandez, E. Hanssen, M. Condrón, Y. H. Tan, J. Baum, and S. H. Scheres, "Cryo-EM structure of the *Plasmodium falciparum* 80S ribosome bound to the anti-protozoan drug emetine," *eLife*, vol. 3, p. e01963, jun 2014.
- [109] P. Lu, X.-c. Bai, D. Ma, T. Xie, C. Yan, L. Sun, G. Yang, Y. Zhao, R. Zhou, S. H. W. Scheres, and Y. Shi, "Three-dimensional structure of human γ -secretase," *Nature*, vol. 512, no. 7513, pp. 166–170, jun 2014.

- [110] D. Stalling, M. Westerhoff, and H. C. Hege, “Amira: a highly interactive system for visual data analysis,” 2005.
- [111] P. Emsley and K. Cowtan, “Coot: model-building tools for molecular graphics.” *Acta crystallographica. Section D, Biological crystallography*, vol. 60, pp. 2126–32, dec 2004.
- [112] K. Zhang, “Gctf: Real-time CTF determination and correction,” *Journal of Structural Biology*, vol. 193, no. 1, pp. 1–12, jan 2016.
- [113] M. van Heel, G. Harauz, E. V. Orlova, R. Schmidt, and M. Schatz, “A New Generation of the IMAGIC Image Processing System,” *Journal of Structural Biology*, vol. 116, no. 1, pp. 17–24, jan 1996.
- [114] A. A. Lebedev, P. Young, M. N. Isupov, O. V. Moroz, A. A. Vagin, and G. N. Murshudov, “JLigand: a graphical tool for the CCP4 template-restraint library.” *Acta crystallographica. Section D, Biological crystallography*, vol. 68, no. Pt 4, pp. 431–40, apr 2012.
- [115] S. H. W. Scheres, “RELION: implementation of a Bayesian approach to cryo-EM structure determination.” *Journal of structural biology*, vol. 180, no. 3, pp. 519–30, dec 2012.
- [116] H. Elmlund, D. Elmlund, and S. Bengio, “PRIME: probabilistic initial 3D model generation for single-particle cryo-electron microscopy.” *Structure*, vol. 21, no. 8, pp. 1299–306, aug 2013.
- [117] E. F. Pettersen, T. D. Goddard, C. C. Huang, G. S. Couch, D. M. Greenblatt, E. C. Meng, and T. E. Ferrin, “UCSF Chimera—a visualization system for exploratory research and analysis.” *Journal of computational chemistry*, vol. 25, no. 13, pp. 1605–12, oct 2004.
- [118] J. D. Dignam, R. M. Lebovitz, and R. G. Roeder, “Accurate transcription initiation by RNA polymerase II in a soluble extract from isolated mammalian nuclei.” *Nucleic acids research*, vol. 11, no. 5, pp. 1475–89, mar 1983.
- [119] U. K. Laemmli, “Cleavage of structural proteins during the assembly of the head of bacteriophage T4.” *Nature*, vol. 227, no. 5259, pp. 680–5, aug 1970.
- [120] J. Schrader, F. Henneberg, R. A. Mata, K. Tittmann, T. R. Schneider, H. Stark, G. Bourenkov, and A. Chari, “The inhibition mechanism of human 20S proteasomes enables next-generation inhibitor design,” *Science*, vol. 353, no. 6299, pp. 594–598, aug 2016.

- [121] F. Weigend and R. Ahlrichs, "Balanced basis sets of split valence, triple zeta valence and quadruple zeta valence quality for H to Rn: Design and assessment of accuracy," *Physical Chemistry Chemical Physics*, vol. 7, no. 18, p. 3297, 2005.
- [122] C. Lee, W. Yang, and R. G. Parr, "Development of the Colle-Salvetti correlation-energy formula into a functional of the electron density," *Physical Review B*, vol. 37, no. 2, pp. 785–789, jan 1988.
- [123] A. D. Becke, "Density-functional thermochemistry. III. The role of exact exchange," *The Journal of Chemical Physics*, vol. 98, no. 7, pp. 5648–5652, apr 1993.
- [124] S. Grimme, S. Ehrlich, and L. Goerigk, "Effect of the damping function in dispersion corrected density functional theory," *Journal of Computational Chemistry*, vol. 32, no. 7, pp. 1456–1465, may 2011.
- [125] A. D. Becke and E. R. Johnson, "A simple effective potential for exchange," *The Journal of Chemical Physics*, vol. 124, no. 22, p. 221101, jun 2006.
- [126] A. Klamt and G. Schüürmann, "COSMO: a new approach to dielectric screening in solvents with explicit expressions for the screening energy and its gradient," *J. Chem. Soc., Perkin Trans. 2*, no. 5, pp. 799–805, 1993.
- [127] M. R. A. Blomberg, T. Borowski, F. Himo, R.-Z. Liao, and P. E. M. Siegbahn, "Quantum Chemical Studies of Mechanisms for Metalloenzymes," *Chemical Reviews*, vol. 114, no. 7, pp. 3601–3658, apr 2014.
- [128] F. Neese, "The ORCA program system," *Wiley Interdisciplinary Reviews: Computational Molecular Science*, vol. 2, no. 1, pp. 73–78, jan 2012.
- [129] B. Rupp, *Biomolecular crystallography : principles, practice, and application to structural biology*. New York: Garland Science, 2010.
- [130] A. A. Vagin, R. A. Steiner, A. A. Lebedev, L. Potterton, S. McNicholas, F. Long, and G. N. Murshudov, "REFMAC 5 dictionary: organization of prior chemical knowledge and guidelines for its use," *Acta Crystallographica Section D Biological Crystallography*, vol. 60, no. 12, pp. 2184–2195, dec 2004.
- [131] T. Grant and N. Grigorieff, "Measuring the optimal exposure for single particle cryo-EM using a 2.6 Å reconstruction of rotavirus VP6." *eLife*, vol. 4, p. e06980, jan 2015.
- [132] K. Zhang, "Gautomatch." [Online]. Available: <http://www.mrc-lmb.cam.ac.uk/kzhang/>
- [133] A. Kucukelbir, F. J. Sigworth, and H. D. Tagare, "Quantifying the local resolution of cryo-EM density maps." *Nature methods*, vol. 11, no. 1, pp. 63–5, jan 2014.

- [134] Y. Song, F. DiMaio, R. Y.-R. Wang, D. Kim, C. Miles, T. Brunette, J. Thompson, and D. Baker, “High-resolution comparative modeling with RosettaCM.” *Structure*, vol. 21, no. 10, pp. 1735–42, oct 2013.
- [135] D. E. Kim, D. Chivian, and D. Baker, “Protein structure prediction and analysis using the Robetta server.” *Nucleic acids research*, vol. 32, pp. W526–31, jul 2004.
- [136] F. Zhang, M. Hu, G. Tian, P. Zhang, D. Finley, P. D. Jeffrey, and Y. Shi, “Structural insights into the regulatory particle of the proteasome from *Methanocaldococcus jannaschii*.” *Molecular cell*, vol. 34, no. 4, pp. 473–84, may 2009.
- [137] L. J. McGuffin, K. Bryson, and D. T. Jones, “The PSIPRED protein structure prediction server.” *Bioinformatics (Oxford, England)*, vol. 16, no. 4, pp. 404–5, apr 2000.
- [138] P. D. Adams, P. V. Afonine, G. Bunkóczi, V. B. Chen, I. W. Davis, N. Echols, J. J. Headd, L.-W. Hung, G. J. Kapral, R. W. Grosse-Kunstleve, A. J. McCoy, N. W. Moriarty, R. Oeffner, R. J. Read, D. C. Richardson, J. S. Richardson, T. C. Terwilliger, and P. H. Zwart, “PHENIX: a comprehensive Python-based system for macromolecular structure solution.” *Acta crystallographica. Section D, Biological crystallography*, vol. 66, no. Pt 2, pp. 213–21, feb 2010.
- [139] S. H. W. Scheres, “Chapter Six - Processing of Structurally Heterogeneous Cryo-EM Data in RELION,” in *Methods in Enzymology*, 2016, vol. 579, pp. 125–157.
- [140] P. A. Penczek, M. Kimmel, and C. M. T. Spahn, “Identifying conformational states of macromolecules by eigen-analysis of resampled cryo-EM images.” *Structure*, vol. 19, no. 11, pp. 1582–90, nov 2011.
- [141] P. I. Zhuravlev and G. A. Papoian, “Protein functional landscapes, dynamics, allostery: a tortuous path towards a universal theoretical framework,” *Quarterly Reviews of Biophysics*, vol. 43, no. 03, pp. 295–332, aug 2010.
- [142] D. L. Beveridge and F. M. DiCapua, “Free Energy Via Molecular Simulation: Applications to Chemical and Biomolecular Systems,” *Annual Review of Biophysics and Biophysical Chemistry*, vol. 18, no. 1, pp. 431–492, jun 1989.
- [143] E. M. Huber, M. Basler, R. Schwab, W. Heinemeyer, C. J. Kirk, M. Groettrup, and M. Groll, “Immuno- and Constitutive Proteasome Crystal Structures Reveal Differences in Substrate and Inhibitor Specificity,” *Cell*, vol. 148, no. 4, pp. 727–738, feb 2012.
- [144] R. Z. Orlowski and D. J. Kuhn, “Proteasome Inhibitors in Cancer Therapy: Lessons from the First Decade,” *Clinical Cancer Research*, vol. 14, no. 6, pp. 1649–1657, mar 2008.

- [145] M. F. Kleijnen, J. Roelofs, S. Park, N. A. Hathaway, M. Glickman, R. W. King, and D. Finley, "Stability of the proteasome can be regulated allosterically through engagement of its proteolytic active sites." *Nature structural & molecular biology*, vol. 14, no. 12, pp. 1180–8, dec 2007.
- [146] D. Haselbach, J. Schrader, F. Lambrecht, F. Henneberg, A. Chari, and H. Stark, "Long-range allosteric regulation of the human 26S proteasome by 20S proteasome-targeting cancer drugs," *Nature Communications*, vol. 8, p. 15578, may 2017.
- [147] C. Haglund, C. Mohanty, M. Fryknäs, P. D'Arcy, R. Larsson, S. Linder, and L. Rickardson, "Identification of an inhibitor of the ubiquitin-proteasome system that induces accumulation of polyubiquitinated proteins in the absence of blocking of proteasome function," *MedChemComm*, vol. 5, no. 3, p. 376, 2014.
- [148] A. Chari, D. Haselbach, J.-M. Kirves, J. Ohmer, E. Paknia, N. Fischer, O. Ganichkin, V. Möller, J. J. Frye, G. Petzold, M. Jarvis, M. Tietzel, C. Grimm, J.-M. Peters, B. A. Schulman, K. Tittmann, J. Markl, U. Fischer, and H. Stark, "ProteoPlex: stability optimization of macromolecular complexes by sparse-matrix screening of chemical space." *Nature methods*, vol. 12, no. 9, pp. 859–65, sep 2015.
- [149] J. R. Casey, S. Grinstein, and J. Orlowski, "Sensors and regulators of intracellular pH," *Nature Reviews Molecular Cell Biology*, vol. 11, no. 1, pp. 50–61, jan 2010.
- [150] M. Groll and R. Huber, "Purification, Crystallization, and X-ray Analysis of the Yeast 20S Proteasome," in *Methods in Enzymology*, 2005, vol. 398, pp. 329–336.
- [151] E. M. Huber, W. Heinemeyer, X. Li, C. S. Arendt, M. Hochstrasser, and M. Groll, "A unified mechanism for proteolysis and autocatalytic activation in the 20S proteasome." *Nature communications*, vol. 7, p. 10900, jan 2016.
- [152] M. Groll, C. R. Berkers, H. L. Ploegh, and H. Ovaa, "Crystal Structure of the Boronic Acid-Based Proteasome Inhibitor Bortezomib in Complex with the Yeast 20S Proteasome," *Structure*, vol. 14, no. 3, pp. 451–456, mar 2006.
- [153] M. Groll, R. Huber, and B. C. M. Potts, "Crystal Structures of Salinosporamide A (NPI-0052) and B (NPI-0047) in Complex with the 20S Proteasome Reveal Important Consequences of β -Lactone Ring Opening and a Mechanism for Irreversible Binding," 2006.
- [154] J. E. Baldwin, R. C. Thomas, L. I. Kruse, and L. Silberman, "Rules for ring closure: ring formation by conjugate addition of oxygen nucleophiles," *The Journal of Organic Chemistry*, vol. 42, no. 24, pp. 3846–3852, nov 1977.

-
- [155] K. Gilmore, R. K. Mohamed, and I. V. Alabugin, “The Baldwin rules: revised and extended,” *Wiley Interdisciplinary Reviews: Computational Molecular Science*, vol. 6, no. 5, pp. 487–514, sep 2016.
- [156] I. Vilotijevic and T. F. Jamison, “Synthesis of marine polycyclic polyethers via endo-selective epoxide-opening cascades.” *Marine drugs*, vol. 8, no. 3, pp. 763–809, mar 2010.
- [157] M. Arciniega, P. Beck, O. F. Lange, M. Groll, and R. Huber, “Differential global structural changes in the core particle of yeast and mouse proteasome induced by ligand binding.” *Proceedings of the National Academy of Sciences of the United States of America*, vol. 111, no. 26, pp. 9479–84, jul 2014.
- [158] P. Sledz, P. Unverdorben, F. Beck, G. Pfeifer, A. Schweitzer, F. Forster, and W. Baumeister, “Structure of the 26S proteasome with ATP- S bound provides insights into the mechanism of nucleotide-dependent substrate translocation,” *Proceedings of the National Academy of Sciences*, pp. 7264–7269, apr 2013.
- [159] S. Asano, Y. Fukuda, F. Beck, A. Aufderheide, F. Forster, R. Danev, and W. Baumeister, “A molecular census of 26S proteasomes in intact neurons,” *Science*, vol. 347, no. 6220, pp. 439–442, jan 2015.
- [160] H.-C. S. Yen, C. Espiritu, and E. C. Chang, “Rpn5 Is a Conserved Proteasome Subunit and Required for Proper Proteasome Localization and Assembly,” *Journal of Biological Chemistry*, vol. 278, no. 33, pp. 30 669–30 676, aug 2003.

Acknowledgements

I would like to thank Holger for giving me the opportunity to carry out my PhD Thesis in his department. I am very grateful to Holger and to my direct supervisor Ashwin, for their guidance and enthusiasm through the projects.

I also want to thank our collaboration partners Thomas and Gleb from the EMBL in Hamburg for their support and Kai and Ricardo from the University of Göttingen for their contribution to our work. The 20S proteasome project would not have been possible without these excellent collaborations.

The Stark lab has been a great place to work over the past four years, and I would like to thank the current and former members of the lab. David, Erik, Steffi, Wen-Ti, Michael, Andrius, Juliane, Niels, Florian, Boris, Jan, Mario, Tobias, Sabrina, Georg, Felix, Lukas, Karl, Kashish, Fabian, Elham, Prakash, Frank, Dietmar, Gudrun, Dirk and Uwe. You all have contributed immensely to my personal and professional development during my PhD.

I would also like to thank Ralf and Karin, for serving as my committee members and for their helpful comments.

This thesis would not have been possible without the moral support of many friends and my family. I would like to thank Tobi, Nils and my mother for all the love and encouragement. Thank you.

Curriculum Vitae

Name: Jil Schrader
Date of birth: 27.Juli.1988
Place of birth: Geseke, Germany

Scientific education

- 04/2013 - present PhD student in the Department of Structural Dynamics, Max Planck Institute for biophysical Chemistry, Göttingen, Thesis title: *Structural Characterization of Proteasome Inhibition*
- 04/2012 - 10/2012 Master Thesis in the Department of Structural Dynamics, Max Planck Institute for biophysical Chemistry, Göttingen, Thesis title: *Mechanistic and Structural Analysis of Key Functional States of the AAA+ ATPase p97*
- 10/2010 - 10/2012 Georg-August University Göttingen: Studies in Microbiology and Biochemistry (MSc.), Specialization in Biochemistry and Structural biology
- 02/2010 - 06/2010 Bachelor Thesis in the Department of Molecular Structural Biology, Georg-August University, Göttingen, Thesis title: *Expression und Reinigung der Spleißfaktoren Ntr1 und Ntr2*
- 10/2007 - 08/2010 Georg-August University Göttingen: Studies in Biology (BSc.), Specialization in Molecular Biosciences

Göttingen, 2017

